

Chapter 13

Double-Passage Problems: Laser Radar Systems

13.1	Introduction	534
13.2	Laser Radar Configuration	536
13.2.1	Basic radar principles	537
13.2.2	Classification of targets	539
13.3	Modeling the Backscattered Wave	540
13.3.1	Gaussian-beam parameters	541
13.3.2	Complex phase perturbations	543
13.3.3	Backscatter amplification effect	546
13.3.4	Scintillation index	547
13.4	Finite Smooth Target—Part I	547
13.4.1	Mutual coherence function	547
13.4.2	Mean irradiance and spot size	550
13.4.3	Backscatter correlation function: Gaussian-beam wave	551
13.4.4	Incident spherical wave	552
13.4.5	Incident plane wave	557
13.5	Finite Smooth Target—Part II	559
13.5.1	Scintillation index: incident beam wave	561
13.5.2	Scintillation index: incident spherical wave	565
13.5.3	Scintillation index: incident plane wave	568
13.6	Finite Smooth Reflector—Part III	570
13.6.1	Spatial coherence: incident beam wave	571
13.6.2	Spatial coherence: incident spherical wave	572
13.7	Unresolved (Point) Target	575
13.7.1	Backscatter amplification factor: weak fluctuations	577
13.7.2	Backscatter amplification factor: strong fluctuations	577
13.7.3	Spatial coherence	581
13.7.4	Covariance and scintillation index: weak fluctuations	581
13.7.5	Scintillation index: strong fluctuations	584
13.8	Diffuse Target	589
13.8.1	Mean irradiance and BSAE	589
13.8.2	Spatial coherence	590
13.8.3	Scintillation index—Part I	591
13.8.4	Scintillation index—Part II	593
13.9	Summary and Discussion	596

13.10	Worked Examples	597
	Problems	599
	References	604

Overview: In this chapter we investigate the double-pass problem that arises in laser radar applications. Namely, the double-passage of an optical wave through the atmosphere to a target and back through exactly the same atmospheric turbulence, but in the opposite direction, can lead to an enhancement in the mean irradiance near the optical axis of the return (echo) beam known as *enhanced backscatter* (EBS), also called the *backscatter amplification effect* (BSAE). Because the spatial coherence of the echo beam and the irradiance fluctuations can also be affected by the double-passage phenomenon, it is important to understand these effects in the design of a laser radar system.

We begin by modeling the backscattered wave in free space from a smooth target of finite size. This involves the introduction of two sets of Gaussian beam parameters as discussed in Chap. 10. In the presence of atmospheric turbulence we can identify two types of double-passage propagation paths—one called the *folded path* and the other called the *reciprocal path*. Each type of path requires separate mathematical treatment with effects from both types of path contributing to the notion of EBS or BSAE. Mathematical models for the *mutual coherence function* associated with a finite smooth reflector (target) in bistatic and monostatic systems are developed first under the assumption of weak irradiance fluctuations. These models include the *mean irradiance*, which identifies the *spot size* of the echo wave, and the BSAE. We follow this with a treatment of the *scintillation index* and the *spatial coherence* properties for the same smooth targets.

The BSAE associated with a small *unresolved target*, also known as a “point target,” is developed under both weak and strong irradiance fluctuations. This is followed by a similar treatment of the scintillation index. Last, we develop models for the limiting case of a fully diffuse (Lambertian) surface that also includes both weak and strong scattering of the optical wave. We distinguish between the cases of a “slow detector” and a “fast detector” in comparison with the temporal fluctuations associated with the rough surface.

13.1 Introduction

The classical theory of pulsed radar performance was developed many years ago by Marcum and Swerling [1] for microwave radars. *Laser radar* or *lidar*

systems are a direct extension of conventional microwave radars to wavelengths from the optical bands. Extension of this classical microwave theory to the optical regime, however, requires some modification to account for the shorter wavelengths in the infrared (IR), visible, and ultraviolet (UV) bands. Such systems are capable of simultaneous measurements of range, reflectivity, velocity, temperature, azimuth, and elevation angle. Because of the shorter wavelength, a laser radar system is more susceptible than a microwave radar system to atmospheric effects like scattering, absorption, and optical turbulence. A *monostatic system* is one in which the transmitter and receiver are colocated. This combination of transmitter/receiver is often referred to as a *transceiver*. In a monostatic channel the transmitted wave must traverse the same atmospheric path twice in opposite directions—once in the forward direction to the target and, upon reflection, back to the receiver in the opposite direction. When the transmitter and receiver are separated in space by much more than a Fresnel zone, it is called a *bistatic system*.

Enhanced backscatter (EBS) effects associated with an optical wave propagating twice in opposite directions through statistically dependent inhomogeneities of a random medium have been the subject of numerous theoretical and experimental studies since the early 1970s [2–17] (see also Refs. [18] and [19] for extensive surveys of early papers). In particular, remote sensing techniques and other applications using laser radar have generated a need for studying the observed *increase in mean irradiance* close to the optical axis of a reflected wave through the atmosphere. This increase in mean irradiance, caused by medium-induced correlations between the incident and reflected (echo) optical waves, is widely known as the *backscatter amplification effect* (BSAE). The BSAE, first predicted by Belen’kii and Mironov [2] for an incident spherical wave on a finite specular target, is defined by the ratio of backscattered mean irradiance of the optical wave after reflection from a surface to that obtained at points for which incident and reflected waves propagate through different inhomogeneities of the random medium, i.e., at points in the source/receiver plane that are sufficiently far from the source. Later it was shown that this increase in the mean irradiance is also accompanied by an *increase in the irradiance fluctuations* and either an *increase or decrease in the spatial coherence radius* of the reflected wave, dependent upon reflection characteristics of the target [3].

Our treatment here of double-passage waves is based primarily on a series of published papers concerning smooth reflectors [12–17] as well as on results in Ref. [18] concerning a diffuse or Lambertian surface. Weak fluctuation theory is applied within the framework of generalized spectral representations for the complex phase perturbations and rotationally symmetric *ABCD* ray matrices developed in Chap. 10. In some cases we can extend the results to strong fluctuation theory using the extended Rytov theory developed in Chaps. 5 and 9. The assumed target models include (i) an unresolved target (also known as a point reflector), (ii) a finite smooth target (mirror), (iii) a finite glint target (retroreflector), and (iv) a finite rough surface target (diffuse surface). Both monostatic and bistatic configurations are discussed.

13.2 Laser Radar Configuration

In our analysis we assume a *Gaussian-beam wave* illuminates a target at range L from the transmitter, is scattered backward by the target, and the echo wave is received in the plane of the transceiver (see Fig. 13.1). Both bistatic and monostatic system configurations are depicted in this figure.

A radar system is generally called *monostatic* when the receiver and transmitter are colocated, and have either the same field of view (FOV) or the FOV of the receiver encompasses the FOV of the transmitter. Otherwise, a radar system is said to be *bistatic*. We say the *channel* of the radar system is *monostatic* when the echo beam wave encounters the same turbulent medium realizations as that of the transmitted beam wave. A *channel* is called *bistatic* when the echo beam wave encounters a statistically independent random medium realization over more of the path than that of the transmitted beam wave. Hence, the operational characteristics of the laser radar system depend in part on the types of channels through which the beam propagates.

To further explain, there may be situations in which a monostatic laser radar system has the operational characteristics of a bistatic system and vice versa. As an example, suppose we have a monostatic system mounted on a fast-moving platform that is tracking a target. From the perspective of the transceiver, the atmospheric turbulence encountered by the beam will act as a “frozen” random medium moving across the propagation path. When the transit time for the medium is less than the round trip transit time of the radar beam to and from the target, the echo beam wave encounters a somewhat different medium realization from that of the transmitted beam wave. Here the monostatic radar system has the operational characteristics of a bistatic channel. The converse of this situation may also occur; if the turbulent medium realization encountered by the transmitted beam wave “moves” into the path of the echo beam wave, a bistatic radar system may have the operational characteristics of a monostatic channel.

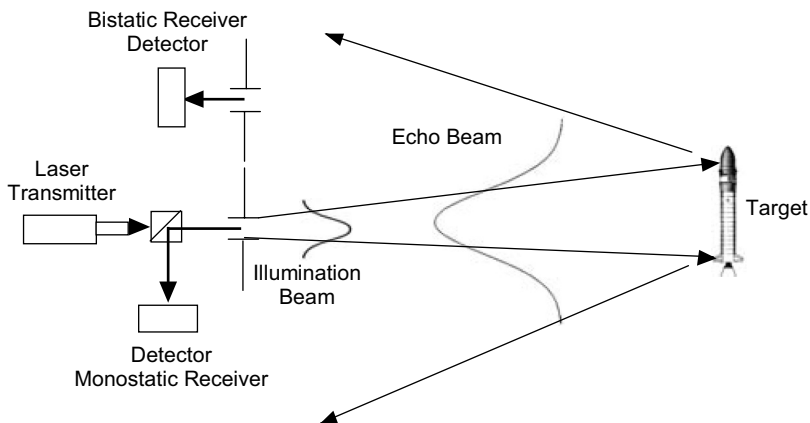


Figure 13.1 Laser radar configuration illustrating double-pass propagation to the target and back to the receiver.

How these characteristics occur depends on the specific design configuration of the system and the target engagement scenario. During any specific scenario, the operational characteristics may change several times due to changes in the types of channels encountered.

13.2.1 Basic radar principles

Radar is concerned with the extraction of target information contained in the received signal. A radar system obtains this information about a possible target by comparing the received echo signal with the transmitted signal. Receiving an echo signal indicates the *presence* of a reflecting target, but target *location*, *velocity*, and type of target (*target classification*) are also important in some applications.

All radar waves are of two types—continuous wave (CW) and pulsed. Pulsed radars that sense Doppler frequencies are further called *pulse Doppler radars*. The (temporal) pulse width is often denoted by the symbol τ , and the number of pulses transmitted per second is the *pulse repetition frequency* (PRF) f_R . The reciprocal of the PRF defines the *pulse repetition interval* (PRI), which provides a measure of the period T between the start of one pulse and the start of the next pulse. The *duty cycle* τ/T represents the fraction of time that the radar is actually transmitting. If P denotes *peak power* in the transmitted pulse, the *average power* is defined by $P_{\text{avg}} = P\tau/T$.

Assuming a target is within the FOV of the radar, it will not be detected unless its echoes are strong enough to distinguish it from the noise at the output of the receiver arising from various sources. The strength of a target echo is described by the received power P_S which is related to the range L of the target according to the power law [20]

$$P_S = \frac{K}{L^4}, \quad (1)$$

where the proportionality constant K depends on transmitted power, effective scattering target cross section, diameter of receiving aperture, wavelength, and attenuation factors caused by atmospheric transmission and system transmission. Equation (1) is one of the most fundamental relations in conventional radar and is known as the *range equation*. It reveals that the received power generally grows rapidly as the target distance is shortened. However, the standard range equation is valid only in the far field of the aperture, which is quite short for most microwaves. For laser wavelengths the far field can be hundreds of kilometers, so laser radars in many applications operate in the near field. This requires modification of the range equation that leads to power law relations like $1/L^2$ or $1/L^3$. For example, in the case of an extended Lambertian target the scattering cross section depends on the inverse square of target range, and the range equation becomes [20]

$$P_S = \frac{\pi P_0 T_0^2 D^2}{(4L)^2}, \quad (2)$$

where P_0 is transmitted power and T_0 is the target reflection coefficient. Attenuation factors have been omitted.

The *angular position* of the target is determined from the line of sight of the narrow echo beam from the target and the *range* L is most easily obtained by *pulse delay ranging*. Thus, range is found by measuring the time delay that the radar pulse signal takes to reach the target and return, which leads to

$$L = \frac{cT_{2L}}{2}, \quad (3)$$

where T_{2L} is the round-trip time and $c = 3 \times 10^8$ m/s is the speed of light. For example, a round-trip time of $10 \mu\text{s}$ corresponds to a range of 1.5 km to the target. Once a transmitted pulse has been sent by the radar, a sufficient length of time must elapse for the echo signal to return before the next pulse is transmitted; otherwise range ambiguities might arise due to the return echo arriving after the second pulse is transmitted. This condition sets the PRF, which depends on the longest range at which targets are expected. Thus, if f_R is the PRF, the *maximum unambiguous range* to a target is

$$L_{\max} = \frac{c}{2f_R}. \quad (4)$$

The echo from a moving target generates a *frequency shift* due to the *Doppler* effect, which is a measure of the *relative velocity* of the target with respect to the radar. The relative velocity can also be determined from *range rate* dL/dt . Tracking radars, for example, often measure relative target velocity by range rate rather than using the Doppler shift. The Doppler frequency shift f_d , relative velocity, and range rate are related by

$$f_d = -\frac{2}{\lambda} \frac{dL}{dt} = -\frac{2V_r}{\lambda}, \quad (5)$$

where V_r is the relative (radial) speed of the target. The negative sign accounts for the fact that Doppler frequency is positive for a closing target and the 2 factor comes from the total path length $2L$. For radar on a moving platform approaching a target head-on (tail-on), the relative velocity in (5) is actually a sum (difference) of target speed and platform speed. Analogous to the maximum unambiguous range (4), the *maximum unambiguous velocity* is given by

$$V_{r,\max} = \frac{\lambda f_R}{2}. \quad (6)$$

Range resolution is the ability of a radar to resolve (separate) two closely spaced targets in range. To better understand this concept, pulse width τ is sometimes expressed in terms of physical *pulse length*. The length of a pulse is defined by

the physical distance between its leading and trailing edges as it propagates through space. Therefore, pulse length is simply equal to τc . For a radar to resolve two targets in range with an unmodulated pulse, the range separation of the targets must be such that the trailing edge of the transmitted pulse will have passed the near target before the leading edge of the echo from the far target reaches the near target. This condition is satisfied if the range separation of the two targets is greater than half the pulse length. Hence, shorter pulses generally give better range resolution and, consequently, better range accuracy.

Last, although typical radars transmit modulated pulses, there are other types of radars that are used. In particular, an unmodulated CW radar can measure range rate by sensing the Doppler shift in the received echo signal. If the target is in motion, both range L and the phase ϕ are continually changing. A change in phase with respect to time is equal to the Doppler frequency shift

$$f_d = -\frac{1}{2\pi} \frac{d\phi}{dt} = -\frac{2}{\lambda} \frac{dL}{dt} = -\frac{2V_r}{\lambda}. \quad (7)$$

CW signals can also be used to indirectly measure target range. However, owing to a narrow bandwidth, an unmodulated CW waveform cannot measure range—to do so requires a broadening of the spectrum bandwidth through amplitude, frequency, or phase modulation.

13.2.2 Classification of targets

By “target,” we are including such things as aircraft, spacecraft, satellites, ships, ground vehicles, buildings, people, and so on. In most radar applications the only properties of a target that are measured are its location in terms of range and angle. Nonetheless, it is possible to extract more information about the target that may lead to target identification or classification. Our treatment of target classification is intentionally brief, focusing only on target size relative to the illumination beam and on broad target characteristics rather than on specific detail. In general, the target of interest may have both *specular* (glint) and *diffuse* reflection components. Specular targets are usually considered to be smooth surfaces such as the surface of a lens or retroreflector. The limiting case of a small specular target leads to the notion of a “point target.” We say a target is classified as a point target if its size is small relative to the size of the first Fresnel zone. A *Lambertian* (diffuse) *surface* is a rough target in which the surface roughness correlation width is on the order of a wavelength (or smaller). Many natural and man-made targets are modeled as Lambertian surfaces for radar analysis.

Targets are further classified as resolved or unresolved. An *unresolved target* is one that lies entirely within the spot size of the illumination beam, and a *resolved target* (also called an *extended target*) is one larger than the illumination beam spot size. The size of an unresolved target is the target size itself. The same is also true if the target is an extended smooth “Gaussian” reflector (mirror). However, the size of an extended diffuse target is generally taken to be the size of the illumination beam in our analysis.

The statistical characteristics of the return echo from a target will be treated in detail in the following sections. Some general characteristics in the echo wave are summarized below:

- *Target return beam spread.* The reflected wave may experience considerable beam spreading along the path back to the receiver, particularly for smaller targets. For a purely diffuse target, however, the return wave will be nondirectional with uniform mean irradiance across the received profile. The most significant effect will be loss of power.
- *Receiver plane loss of spatial coherence.* For a small unresolved target the transverse spatial coherence radius of the return wave will be determined by the spatial coherence of an echo spherical wave propagating through optical turbulence from the target to the receiver. For a diffuse target the spatial coherence radius of the return optical wave may be greatly diminished over that of the illumination wave on the target, depending on the size of the target—larger targets lead to a greater loss of coherence.
- *Receiver plane scintillation.* Scintillation in the echo wave of a bistatic system will generally consist of two distinct terms (related to incident and echo waves). In a monostatic channel that is stationary during the transit time of the echo return, there is an additional term caused by correlations between incident and reflected waves. The most deleterious effects from scintillation will be loss of signal-to-noise ratio and dropouts (information loss).

13.3 Modeling the Backscattered Wave

Let us assume a Gaussian-beam wave incident on a smooth reflecting surface at distance L from the source is scattered backward and received in the plane of the transmitter (see Fig. 13.2). If the beam wave at the input plane ($z = 0$) has unit amplitude, effective beam radius W_0 , and phase front radius of curvature F_0 , it can be characterized by

$$U_0(\mathbf{r}, 0) = \exp\left(-\frac{r^2}{W_0^2} - j\frac{kr^2}{2F_0}\right) = \exp\left(-\frac{1}{2}\alpha_0 kr^2\right), \quad (8)$$

where k is the optical wave number, r denotes distance in the transverse direction, the parameter $\alpha_0 = 2/(kW_0^2) + j/F_0$, and $j^2 = -1$. (In this chapter we use $j = \sqrt{-1}$ instead of i to designate the imaginary component.) In the absence of turbulence, the reflected wave back at the source/receiver plane is described by the generalized Huygens-Fresnel integral

$$\begin{aligned} U_0(\mathbf{r}, 2L) &= -\frac{jk}{2\pi B} \exp(2jkL) \int \int_{-\infty}^{\infty} d^2s \exp\left(-\frac{1}{2}\alpha_0 ks^2\right) \exp\left[\frac{jk}{2B}(As^2 - 2\mathbf{s} \cdot \mathbf{r} + Dr^2)\right] \\ &= \frac{1}{A + j\alpha_0 B} \exp(2jkL) \exp\left[-\frac{1}{2}\left(\frac{\alpha_0 D - jC}{A + j\alpha_0 B}\right)kr^2\right], \end{aligned} \quad (9)$$

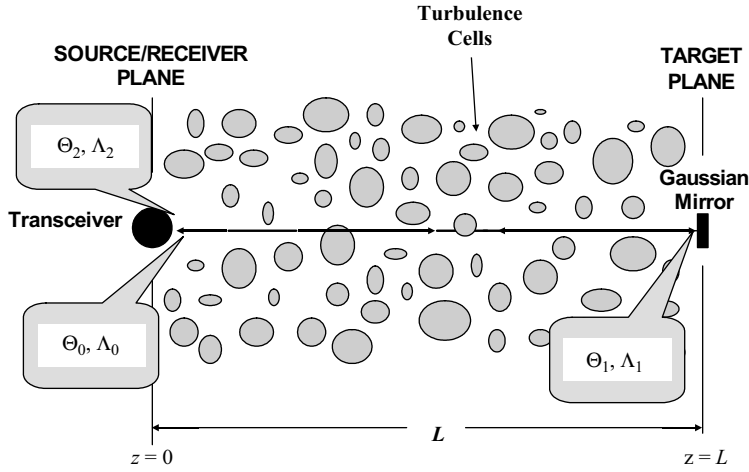


Figure 13.2 Illustration of the propagation channel for a reflected Gaussian-beam wave from a finite smooth reflector.

where $2L$ refers to the total distance traveled and A , B , C , and D are the ray-matrix elements describing the optical channel to the target and back, including the (smooth) target characteristics (see Chap. 10).

The $ABCD$ matrix characterizing the propagation path shown in Fig. 13.2 is

$$\begin{aligned} \begin{pmatrix} A & B \\ C & D \end{pmatrix} &= \begin{pmatrix} 1 & L \\ 0 & 1 \end{pmatrix} \begin{pmatrix} 1 & 0 \\ j\alpha_R & 1 \end{pmatrix} \begin{pmatrix} 1 & L \\ 0 & 1 \end{pmatrix} \\ &= \begin{pmatrix} 1 + j\Omega_R & L + L(1 + j\Omega_R) \\ j\alpha_R & 1 + j\Omega_R \end{pmatrix}, \end{aligned} \quad (10)$$

where we have introduced the target parameters

$$\alpha_R = \frac{2}{kW_R^2}, \quad \Omega_R = \alpha_R L = \frac{2L}{kW_R^2}, \quad (11)$$

and where W_R denotes the radius of the reflector (target). The parameter Ω_R is a nondimensional parameter that characterizes the finite size of the target. The target described by the center 2×2 matrix in (10) is called a *Gaussian mirror*, analogous to the notion of a Gaussian lens introduced in Chaps. 4 and 10.

13.3.1 Gaussian-beam parameters

It facilitates the following analysis to introduce various Gaussian-beam parameters that characterize the beam at the source, reflector, and receiver (see Fig. 13.2).

First, for the transmitted Gaussian-beam wave defined by Eq. (8), we introduce the nondimensional curvature and Fresnel ratio beam parameters

$$\Theta_0 = 1 - \frac{L}{F_0}, \quad \Lambda_0 = \frac{2L}{kW_0^2}. \quad (12)$$

The illumination beam in the plane of the target in the absence of atmospheric effects is

$$\begin{aligned} U_0(\mathbf{r}, L) &= (\Theta_1 - j\Lambda_1) \exp \left[jkL + \frac{jk}{2L} (\bar{\Theta}_1 + j\Lambda_1) r^2 \right] \\ &= (\Theta_1 - j\Lambda_1) \exp \left[-\frac{r^2}{W_1^2} + jk \left(L - \frac{r^2}{2F_1} \right) \right], \end{aligned} \quad (13)$$

where

$$\begin{aligned} \Theta_1 &= \frac{\Theta_0}{\Theta_0^2 + \Lambda_0^2} = 1 + \frac{L}{F_1}, \\ \bar{\Theta}_1 &= 1 - \Theta_1, \\ \Lambda_1 &= \frac{\Lambda_0}{\Theta_0^2 + \Lambda_0^2} = \frac{2L}{kW_1^2}. \end{aligned} \quad (14)$$

Here, F_1 [m] and W_1 [m] characterize the phase front radius of curvature and spot radius of the illumination beam. For the special case of a point target, the above sets of beam parameters are generally adequate to describe the double-pass wave at the transceiver. However, if the illuminated target cross section is finite, we model the “effective” target cross section as circular in shape with Gaussian radius W_R [m]. Thus, in the case of a smooth reflector, it is useful to describe the reflected wave back in the plane of the transceiver by use of the additional beam parameters

$$\begin{aligned} \Theta_2 &= \frac{2 - \Theta_1}{(2 - \Theta_1)^2 + (\Lambda_1 + \Omega_R)^2} = 1 + \frac{L}{F}, \\ \Lambda_2 &= \frac{\Lambda_1 + \Omega_R}{(2 - \Theta_1)^2 + (\Lambda_1 + \Omega_R)^2} = \frac{2L}{kW^2}, \end{aligned} \quad (15)$$

where F [m] is the phase front radius of curvature at the pupil plane of the receiver and W [m] is the spot radius.

The complex amplitude of the received wave is

$$A_0 = (\Theta_1 - j\Lambda_1)(\Theta_2 - j\Lambda_2) = \Theta - j\Lambda, \quad (16)$$

which leads to another set of parameters Θ, Λ (without subscripts) that are also used on occasion. If we compare the real and imaginary parts of (16), this last set of beam parameters can be defined explicitly by

$$\begin{aligned}
\Theta &= \Theta_1 \Theta_2 - \Lambda_1 \Lambda_2, \\
\overline{\Theta} &= 1 - \Theta, \\
\Lambda &= \Lambda_1 \Theta_2 + \Theta_1 \Lambda_2.
\end{aligned} \tag{17}$$

Based on Eq. (16), we see that Θ represents the real part of the free-space complex amplitude A_0 of the echo beam and $-\Lambda$ is the imaginary part.

The irradiance of the free-space reflected optical wave in the receiver plane can be expressed in several equivalent forms, depending on how we choose to represent the complex amplitude. These forms lead to the following expressions:

$$\begin{aligned}
I^0(\mathbf{r}, 2L) &= |U_0(\mathbf{r}, 2L)|^2 = (\Theta_1^2 + \Lambda_1^2)(\Theta_2^2 + \Lambda_2^2) \exp\left(-\frac{2r^2}{W^2}\right) \\
&= (\Theta^2 + \Lambda^2) \exp\left(-\frac{2r^2}{W^2}\right) \\
&= \frac{W_0^2}{W^2(1 + \Omega_R/\Lambda_1)} \exp\left(-\frac{2r^2}{W^2}\right).
\end{aligned} \tag{18}$$

The factor $(1 + \Omega_R/\Lambda_1)$ in the denominator of the last expression in Eq. (18) accounts for power loss of the transmitted beam owing to the finite size of the reflector. For a fixed transmitter spot size W_0 , the spot size W at the receiver is always minimized for a particular reflector size. In the case of a collimated beam ($\Theta_0 = 1$), for example, this minimum occurs for finite reflectors characterized by $\Omega_R \sim 1$ (see Example 1 in the Worked Examples).

13.3.2 Complex phase perturbations

Using the *Rytov approximation*, the reflected wave received in the source/receiver plane ($z = 0$) after reflection from a smooth reflector (at $z = L$) in the presence of atmospheric turbulence is

$$U(\mathbf{r}, 2L) = U_0(\mathbf{r}, 2L) \exp[\psi_1(\mathbf{r}, 2L) + \psi_2(\mathbf{r}, 2L) + \dots], \tag{19}$$

where $U_0(\mathbf{r}, 2L)$ is the optical field (9) of the Gaussian-beam wave at the receiver in the absence of turbulence and $\psi_1(\mathbf{r}, 2L)$ and $\psi_2(\mathbf{r}, 2L)$ denote first-order and second-order corrections of the complex phase perturbation of the wave caused by atmospheric effects. It has been recognized that two types of correlation terms exist in the complex phase perturbation caused by the random medium—one arising from a “reciprocal path” geometry and one arising from a “folded-path” geometry (or straight-back path) of the reflected radiation [13,21]. The reciprocal path geometries are depicted in Fig. 13.3 by the paths ABCDA and ADCBA, which indicate that two optical rays simultaneously traverse along each path through exactly the same atmospheric turbulence but in opposite

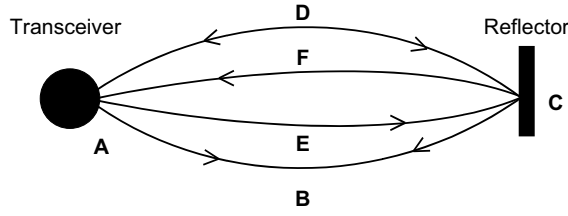


Figure 13.3 Diagram depicting two types of propagation geometries. Reciprocal paths are described by ABCDA and ADCBA, whereas a folded path is only one such path like AECFA.

directions. Also illustrated in Fig. 13.3 is the folded-path geometry described by AECFA. Thus, it is useful to further express $\psi_1(\mathbf{r}, 2L)$ as the sum of two statistically independent terms in the form

$$\begin{aligned}\psi_1(\mathbf{r}, 2L) &= \psi_a(\mathbf{r}, 2L) + \psi_b(\mathbf{r}, 2L) \\ &= \psi_a^i(\pm \mathbf{r}, L) + \psi_a^R(\mathbf{r}, L) + \psi_b^{i*}(0, L) + \psi_b^R(\mathbf{r}, L),\end{aligned}\quad (20)$$

where $\psi_a(\mathbf{r}, 2L)$ is the first-order complex phase perturbation associated with folded-path integrals and $\psi_b(\mathbf{r}, 2L)$ is due to reciprocal paths of the optical wave modeled as two single-passage waves propagating backward in opposite directions through the atmosphere with the reflector and receiver acting like pseudosources. The superscripts i and R refer to incident and reflected waves, respectively, but not in the strict sense,¹ and the asterisk $*$ denotes the complex conjugate. Finally, the upper (positive) sign in the argument of $\psi_a^i(\pm \mathbf{r}, L)$ is used with a plane mirror target whereas the lower (negative) sign is used with a retroreflector.

Statistical moments associated with the folded-path complex phase perturbation $\psi_a(\mathbf{r}, 2L)$ can be obtained directly from the spectral representation [see Eq. (85) in Chap. 5 and Section 10.2.2]

$$\begin{aligned}\psi_a(\mathbf{r}, 2L) &= \psi_a^i(\pm \mathbf{r}, L) + \psi_a^R(\mathbf{r}, L) \\ &= jk \int_0^L \int \int_{-\infty}^{\infty} \exp \left[\pm j\gamma_a^i \mathbf{K} \cdot \mathbf{r} - \frac{j\kappa^2 \gamma_a^i}{2k} B_a^i(z; 2L) \right] dv(\mathbf{K}, z) dz \\ &\quad + jk \int_0^L \int \int_{-\infty}^{\infty} \exp \left[j\gamma_a^R \mathbf{K} \cdot \mathbf{r} - \frac{j\kappa^2 \gamma_a^R}{2k} B_a^R(z; 2L) \right] dv(\mathbf{K}, z) dz,\end{aligned}\quad (21)$$

where γ_a^i is the path amplitude ratio of the complex on-axis amplitude of the incident wave at the observation plane to that along the propagation path between the emitting aperture and the reflector, γ_a^R is the path amplitude ratio between the reflector and the source/receiver plane, $B_a^i(z; 2L)$ and $B_a^R(z; 2L)$ are generalized distance ray-matrix elements for an optical wave propagating backward through

¹The terms with superscript i do not refer to the one-way target illumination beam since these terms generally will also involve target characteristics.

the system, and the random amplitude $dv(\mathbf{K}, z)$ is related to the fluctuating refractive index $n_1(\mathbf{r}, z)$ according to

$$n_1(\mathbf{r}, z) = \int \int_{-\infty}^{\infty} \exp(j\mathbf{K} \cdot \mathbf{r}) dv(\mathbf{K}, z). \quad (22)$$

Writing $\xi = 1 - z/L$, it follows from Eqs. (14)–(18) in Chap. 10 that

$$\gamma_a^i = (\Theta - j\Lambda)\xi + (\Theta_2 - j\Lambda_2)(1 - \xi), \quad (23)$$

$$\gamma_a^R = \xi + (\Theta_2 - j\Lambda_2)(1 - \xi), \quad (24)$$

$$B_a^i(z; 2L) \equiv B_a^i(\xi) = L(1 + \xi + j\xi\Omega_R), \quad (25)$$

$$B_a^R(z; 2L) \equiv B_a^R(\xi) = L(1 - \xi). \quad (26)$$

Equations (23)–(26) are valid for both a plane mirror and a retroreflector.

In dealing with the reciprocal path terms, we express $\psi_b(\mathbf{r}, 2L)$ as the sum of complex phase perturbations of the backward propagating “designated incident wave” evaluated on the beam axis and the “designated reflected wave” at some off-axis point. Hence, the spectral representation used in this calculation is

$$\begin{aligned} \psi_b(\mathbf{r}, 2L) &= \psi_b^{i*}(0, L) + \psi_b^R(\mathbf{r}, L) \\ &= -jk \int_0^L \int \int_{-\infty}^{\infty} \exp\left[\frac{j\kappa^2 \gamma_b^{i*}}{2k} B_b^{i*}(z; 2L)\right] dv^*(\mathbf{K}, z) dz \\ &\quad + jk \int_0^L \int \int_{-\infty}^{\infty} \exp\left[j\gamma_b^R \mathbf{K} \cdot \mathbf{r} - \frac{j\kappa^2 \gamma_b^R}{2k} B_b^R(z; 2L)\right] dv(\mathbf{K}, z) dz. \end{aligned} \quad (27)$$

However, the only moments that are permitted to arise from this representation are those involving products of the “incident wave” with the “reflected wave.” If we once again introduce the normalized distance variable $\xi = 1 - z/L$, the various parameters in (27) for the case of a *plane mirror* are defined by [13]

$$\begin{aligned} \gamma_b^i &= \frac{(\Theta - j\Lambda)B_a^i(\xi)}{L} + \frac{B_a^R(\xi)}{L} \\ &= (\Theta - j\Lambda)(1 + \xi + j\xi\Omega_R) + 1 - \xi, \end{aligned} \quad (28)$$

$$\gamma_b^R = \gamma_a^R - \gamma_a^i = (\bar{\Theta} + j\Lambda)\xi, \quad (29)$$

$$B_b^i(z; 2L) \equiv B_b^i(\xi) = L - B_a^R(\xi) = L\xi, \quad (30)$$

$$B_b^R(z; 2L) \equiv B_b^R(\xi) = B_a^R(\xi) = L(1 - \xi). \quad (31)$$

For the case of a *retroreflector*, the corresponding expressions are [8]

$$\gamma_b^i = \gamma_a^i = (\Theta - j\Lambda)\xi + (\Theta_2 - j\Lambda_2)(1 - \xi), \quad (32)$$

$$\gamma_b^R = \gamma_a^R + \gamma_a^i = (1 + \Theta - j\Lambda)\xi + 2(\Theta_2 - j\Lambda_2)(1 - \xi), \quad (33)$$

$$B_b^i(z; 2L) \equiv B_b^i(\xi) = B_a^i(\xi) + B_a^R(\xi) = L(2 + j\xi\Omega_R), \quad (34)$$

$$B_b^R(z; 2L) \equiv B_b^R(\xi) = B_a^R(\xi) = L(1 - \xi). \quad (35)$$

13.3.3 Backscatter amplification effect

The *backscatter amplification effect* (BSAE) in a monostatic radar channel is an increase in mean irradiance near the optical axis of a reflected wave (also called *enhanced backscatter* or EBS). This increase in mean irradiance is caused by correlations between the incident and echo waves propagating through the same optical turbulence, but in opposite directions. The EBS phenomenon has been discussed theoretically and verified experimentally by many researchers. An excellent treatment of EBS and a list of references to many of the early papers is provided in the text *LIDAR in a Turbulent Atmosphere* by Banakh and Mironov [6]. General models have now been developed for many of the statistical quantities of interest, but these are often restricted to either weak irradiance fluctuations or the saturation regime.

For a monostatic channel we assume the irradiance of the received wave can be written as a modulation or product

$$I(\mathbf{r}, 2L) = C(\mathbf{r})I(\mathbf{r}, 2L)_{\text{bistatic}}, \quad (36)$$

where $I(\mathbf{r}, 2L)_{\text{bistatic}}$ is the irradiance that would exist in the absence of correlations between incident and echo waves, e.g., for a bistatic channel. The quantity $C(\mathbf{r})$ is a (unitless) statistically independent random amplification factor modulating $I(\mathbf{r}, 2L)_{\text{bistatic}}$. Hence, by taking the mean value of both sides of (36), it can be shown that the mean value of $C(\mathbf{r})$ under *weak fluctuations* has the form

$$\langle C(\mathbf{r}) \rangle = \frac{\langle I(\mathbf{r}, 2L) \rangle}{\langle I(\mathbf{r}, 2L) \rangle_{\text{bistatic}}} = \exp[B_I^{iR}(\mathbf{r}, L)], \quad (37)$$

where $B_I^{iR}(\mathbf{r}, L)$ is the BSAE *correlation function* of the irradiance defined below. The notation $N(\mathbf{r}) = \langle C(\mathbf{r}) \rangle$ is also commonly used for (37). The maximum value of $B_I^{iR}(\mathbf{r}, L)$ takes place at $r = 0$ and it generally decreases to zero at all points sufficiently far from the optical axis. Hence, the amplification factor $\langle C(\mathbf{r}) \rangle$ has essentially a unit mean value at all points sufficiently far from the optical axis (i.e., no EBS effects).

13.3.4 Scintillation index

Building on the irradiance model described by Eq. (36), the normalized variance of irradiance, or *scintillation index*, for a monostatic channel is

$$\begin{aligned}\sigma_I^2(\mathbf{r}, 2L)_{\text{monostatic}} &= \frac{\langle I^2(\mathbf{r}, 2L) \rangle}{\langle I(\mathbf{r}, 2L) \rangle^2} - 1 \\ &= \frac{\langle C^2(\mathbf{r}) \rangle \langle I^2(\mathbf{r}, 2L) \rangle_{\text{bistatic}}}{\langle C(\mathbf{r}) \rangle^2 \langle I(\mathbf{r}, 2L) \rangle_{\text{bistatic}}^2} - 1 \\ &= \frac{\langle C^2(\mathbf{r}) \rangle}{\langle C(\mathbf{r}) \rangle^2} [1 + \sigma_I^2(\mathbf{r}, 2L)_{\text{bistatic}}] - 1,\end{aligned}\quad (38)$$

where $\sigma_I^2(\mathbf{r}, 2L)_{\text{bistatic}}$ is the scintillation index that would exist in a bistatic system. In the following sections we will develop models for the normalized second moment of the amplification factor $\langle C(\mathbf{r})^2 \rangle / \langle C(\mathbf{r}) \rangle^2$.

13.4 Finite Smooth Target—Part I

Most realistic targets are rough surfaces. However, if the target roughness correlation width is sufficiently large (see Section 16.8), we can often classify the target as “smooth.” In such cases we model the target as a circular mirror of finite size. We include the case of a *retroreflector* here in addition to a *flat* or *plane mirror*. The free-space analysis with the *ABCD* matrix representation of the propagation channel, including the target, does not generally distinguish between these two types of smooth targets (Section 13.3).

13.4.1 Mutual coherence function

The *mutual coherence function* (MCF) associated with a reflected Gaussian-beam wave in the plane of the receiver is defined by the ensemble average

$$\begin{aligned}\Gamma_2(\mathbf{r}_1, \mathbf{r}_2, 2L) &= \langle U(\mathbf{r}_1, 2L) U^*(\mathbf{r}_2, 2L) \rangle \\ &= \Gamma_2^0(\mathbf{r}_1, \mathbf{r}_2, 2L) P(\mathbf{r}_1, \mathbf{r}_2) N(\mathbf{r}_1, \mathbf{r}_2),\end{aligned}\quad (39)$$

where the first factor represents the MCF in the absence of atmospheric turbulence, i.e.,

$$\begin{aligned}\Gamma_2^0(\mathbf{r}_1, \mathbf{r}_2, 2L) &= U_0(\mathbf{r}_1, 2L) U_0^*(\mathbf{r}_2, 2L) \\ &= \frac{W_0^2}{W^2(1 + \Omega_R/\Lambda_1)} \exp \left[-\frac{(r_1^2 + r_2^2)}{W^2} - \frac{jk(r_1^2 - r_2^2)}{2F} \right].\end{aligned}\quad (40)$$

The remaining factors in (39), which are attributed to effects of the random medium, are described by

$$P(\mathbf{r}_1, \mathbf{r}_2) = \exp[2E_1(0, 0) + \langle \psi_a^i(\pm \mathbf{r}_1, L) \psi_a^{i*}(\pm \mathbf{r}_2, L) \rangle + \langle \psi_a^R(\mathbf{r}_1, L) \psi_a^{R*}(\mathbf{r}_2, L) \rangle], \quad (41)$$

$$N(\mathbf{r}_1, \mathbf{r}_2) = \exp[\langle \psi_a^i(\pm \mathbf{r}_1, L) \psi_a^{R*}(\mathbf{r}_2, L) \rangle + \langle \psi_a^R(\mathbf{r}_1, L) \psi_a^{i*}(\pm \mathbf{r}_2, L) \rangle + \langle \psi_b^i(0, L) \psi_b^R(\mathbf{r}_1, L) \rangle + \langle \psi_b^{i*}(0, L) \psi_b^{R*}(\mathbf{r}_2, L) \rangle]. \quad (42)$$

In the absence of mutual correlations between incident and reflected waves, the factor $P(\mathbf{r}_1, \mathbf{r}_2)$ defined by Eq. (41) describes the angular spread and loss of transverse spatial coherence of the received wave due to turbulence. It is the same for both a plane mirror and a retroreflector. Under the assumption of a *statistically homogeneous* and *isotropic* medium, the quantity $E_1(0, 0)$ appearing in (41) is the same as that defined in Chap. 6, but here for a path of length $2L$, i.e.,

$$\begin{aligned} E_1(0, 0) &= \langle \psi_2(\mathbf{r}, 2L) \rangle + \frac{1}{2} \langle \psi_a^2(\mathbf{r}, 2L) \rangle \\ &= -4\pi^2 k^2 L \int_0^\infty \kappa \Phi_n(\kappa) d\kappa. \end{aligned} \quad (43)$$

Also, based on the spectral representation (21) and the quantities defined by Eqs. (23) through (26), the remaining factors in (41) can be expressed as

$$\begin{aligned} &\langle \psi_a^i(\pm \mathbf{r}_1, L) \psi_a^{i*}(\pm \mathbf{r}_2, L) \rangle + \langle \psi_a^R(\mathbf{r}_1, L) \psi_a^{R*}(\mathbf{r}_2, L) \rangle \\ &= 4\pi^2 k^2 L \int_0^1 \int_0^\infty \kappa \Phi_n(\kappa) J_0(|\gamma_a^i \mathbf{r}_1 - \gamma_a^{i*} \mathbf{r}_2| \kappa) \\ &\quad \times \exp\left\{-\frac{j\kappa^2}{2k} [\gamma_a^i B_a^i(\xi) - \gamma_a^{i*} B_a^{i*}(\xi)]\right\} d\kappa d\xi \\ &\quad + 4\pi^2 k^2 L \int_0^1 \int_0^\infty \kappa \Phi_n(\kappa) J_0(|\gamma_a^R \mathbf{r}_1 - \gamma_a^{R*} \mathbf{r}_2| \kappa) \\ &\quad \times \exp\left\{-\frac{j\kappa^2}{2k} [\gamma_a^R B_a^R(\xi) - \gamma_a^{R*} B_a^{R*}(\xi)]\right\} d\kappa d\xi, \end{aligned} \quad (44)$$

where $J_0(x)$ is a Bessel function of order zero (see Appendix I). By combining the results of (43) and (44), we deduce that

$$\begin{aligned} P(\mathbf{r}_1, \mathbf{r}_2) &= \exp\left[-4\pi^2 k^2 L \int_0^1 \int_0^\infty \kappa \Phi_n(\kappa) \left[1 - J_0(|\gamma_a^i \mathbf{r}_1 - \gamma_a^{i*} \mathbf{r}_2| \kappa) \right. \right. \\ &\quad \times \exp\left\{-\frac{j\kappa^2}{2k} [\gamma_a^i B_a^i(\xi) - \gamma_a^{i*} B_a^{i*}(\xi)]\right\} d\kappa d\xi \\ &\quad \left. \left. - 4\pi^2 k^2 L \int_0^1 \int_0^\infty \kappa \Phi_n(\kappa) \left[1 - J_0(|\gamma_a^R \mathbf{r}_1 - \gamma_a^{R*} \mathbf{r}_2| \kappa) \right. \right. \right. \\ &\quad \left. \left. \times \exp\left\{-\frac{j\kappa^2}{2k} [\gamma_a^R B_a^R(\xi) - \gamma_a^{R*} B_a^{R*}(\xi)]\right\} d\kappa d\xi \right] \right]. \end{aligned} \quad (45)$$

The factor $N(\mathbf{r}_1, \mathbf{r}_2)$ defined by Eq. (42) describes the redistribution of energy in the reflected beam caused by correlations between the complex phase perturbations of the incident and reflected waves. It includes terms that are due to folded-path correlations as well as reciprocal-path correlations, and its general form is

$$N(\mathbf{r}_1, \mathbf{r}_2) = \exp[B_\Gamma^{iR}(\mathbf{r}_1, \mathbf{r}_2, L)], \quad (46)$$

where the correlation function is defined by²

$$\begin{aligned} B_\Gamma^{iR}(\mathbf{r}_1, \mathbf{r}_2, L) = & 4\pi^2 k^2 L \int_0^1 \int_0^\infty \kappa \Phi_n(\kappa) J_0(|\gamma_a^i \mathbf{r}_1 \mp \gamma_a^{R*} \mathbf{r}_2| \kappa) \\ & \times \exp\left\{-\frac{j\kappa^2}{2k} [\gamma_a^i B_a^i(\xi) - \gamma_a^{R*} B_a^{R*}(\xi)]\right\} d\kappa d\xi \\ & + 4\pi^2 k^2 L \int_0^1 \int_0^\infty \kappa \Phi_n(\kappa) J_0(|\gamma_a^R \mathbf{r}_1 \mp \gamma_a^{i*} \mathbf{r}_2| \kappa) \\ & \times \exp\left\{\frac{j\kappa^2}{2k} [\gamma_a^{i*} B_a^{i*}(\xi) - \gamma_a^R B_a^R(\xi)]\right\} d\kappa d\xi \\ & - 4\pi^2 k^2 L \int_0^1 \int_0^\infty \kappa \Phi_n(\kappa) J_0(\gamma_b^R r_1 \kappa) \\ & \times \exp\left\{-\frac{j\kappa^2}{2k} [\gamma_b^i B_b^i(\xi) + \gamma_b^R B_b^R(\xi)]\right\} d\kappa d\xi \\ & - 4\pi^2 k^2 L \int_0^1 \int_0^\infty \kappa \Phi_n(\kappa) J_0(\gamma_b^{R*} r_2 \kappa) \\ & \times \exp\left\{\frac{j\kappa^2}{2k} [\gamma_b^{i*} B_b^{i*}(\xi) + \gamma_b^{R*} B_b^{R*}(\xi)]\right\} d\kappa d\xi. \end{aligned} \quad (47)$$

To arrive at (47), we used the spectral representations (21) and (27). For terms in which both plus and minus signs appear together, the upper sign is always associated with a plane mirror reflector and the lower sign with a retroreflector. In the following discussion the factors $P(\mathbf{r}_1, \mathbf{r}_2)$ and $N(\mathbf{r}_1, \mathbf{r}_2)$ are sometimes expressed in terms of difference and center-of-gravity coordinates defined by

$$\begin{aligned} \mathbf{p} &= \mathbf{r}_1 - \mathbf{r}_2, \quad \mathbf{r} = \frac{1}{2}(\mathbf{r}_1 + \mathbf{r}_2). \\ \rho &= |\mathbf{p}|, \quad r = |\mathbf{r}|. \end{aligned} \quad (48)$$

The general expression (39) for the MCF is based on a monostatic system configuration in which the source and receiver are colocated. In the case of a bistatic system, the correlation function (47) vanishes and the factor $N(\mathbf{r}_1, \mathbf{r}_2)$ becomes unity. Below, we examine the mean irradiance deduced from the above results

²The reader should not confuse the notation $B_\Gamma^{iR}(\mathbf{r}_1, \mathbf{r}_2, L)$ for the EBS correlation function with generalized distance matrix elements like $B_a^i(\xi)$ and $B_a^R(\xi)$.

and also the scintillation index—taking into account both monostatic and bistatic system configurations.

13.4.2 Mean irradiance and spot size

The MCF (39) evaluated at identical observation points $\mathbf{r}_1 = \mathbf{r}_2 = \mathbf{r}$ leads to the *mean irradiance*

$$\langle I(\mathbf{r}, 2L) \rangle = \Gamma_2(\mathbf{r}, \mathbf{r}, 2L) = \frac{W_0^2}{W^2(1 + \Omega_R/\Lambda_1)} \exp\left(-\frac{2r^2}{W^2}\right) P(\mathbf{r}) N(\mathbf{r}), \quad (49)$$

where $P(\mathbf{r}) \equiv P(\mathbf{r}, \mathbf{r})$ and $N(\mathbf{r}) \equiv N(\mathbf{r}, \mathbf{r})$. In the absence of the mutual correlations, Eq. (49) reduces to the mean irradiance associated with a bistatic channel, viz.,

$$\langle I(\mathbf{r}, 2L) \rangle_{\text{bistatic}} = \frac{W_0^2}{W^2(1 + \Omega_R/\Lambda_1)} \exp\left(-\frac{2r^2}{W^2}\right) P(\mathbf{r}). \quad (50)$$

Based on Eq. (45), it follows that

$$\begin{aligned} P(\mathbf{r}) = & \exp \left[-4\pi^2 k^2 L \int_0^1 \int_0^\infty \kappa \Phi_n(\kappa) \left\{ 1 - I_0[2\kappa r(\Lambda_2 - \Lambda_2 \xi + \Lambda \xi)] \right. \right. \\ & \times \exp \left[-\frac{\Lambda_1 L \kappa^2}{k} \xi (\Theta_2 + \bar{\Theta}_2 \xi + \Theta \xi) \right] \\ & \times \exp \left[-\frac{L \kappa^2}{k} (1 - \bar{\Theta}_1 \xi)(\Lambda_2 - \Lambda_2 \xi + \Lambda \xi) \right] \left. \right\} d\kappa d\xi \\ & - 4\pi^2 k^2 L \int_0^1 \int_0^\infty \kappa \Phi_n(\kappa) \\ & \times \left[1 - I_0(2\Lambda_2 \kappa \xi r) \exp \left(-\frac{\Lambda_2 L \kappa^2 \xi^2}{k} \right) \right] d\kappa d\xi \Big], \end{aligned} \quad (51)$$

where $I_0(x) = J_0(jx)$. To obtain a simple expression for the effective spot size of the reflected wave in the presence of atmospheric turbulence, we follow the approach used in Chap. 6 for single-pass propagation. In particular, we recognize that, under weak irradiance fluctuation conditions, the quantity (51) on the optical axis can be written as

$$P(0) = \exp(-T_i - T_R) \cong \frac{1}{1 + T_i + T_R}, \quad (52)$$

the last step of which is based on a small argument approximation in the exponential function. The quantities T_i and T_R are defined explicitly by

$$T_i = 4\pi^2 k^2 L \int_0^1 \int_0^\infty \kappa \Phi_n(\kappa) \left\{ 1 - \exp \left[-\frac{\Lambda_1 L \kappa^2}{k} \xi (\Theta_2 + \bar{\Theta}_2 \xi + \Theta \xi) \right] \right. \\ \left. \times \exp \left[-\frac{L \kappa^2}{k} (1 - \bar{\Theta}_1 \xi) (\Lambda_2 - \Lambda_2 \xi + \Lambda \xi) \right] \right\} d\kappa d\xi, \quad (53)$$

$$T_R = 4\pi^2 k^2 L \int_0^1 \int_0^\infty \kappa \Phi_n(\kappa) \left[1 - \exp \left(-\frac{\Lambda_2 L \kappa^2 \xi^2}{k} \right) \right] d\kappa d\xi. \quad (54)$$

For $r \neq 0$, a useful approximation to $P(\mathbf{r})$ is given by

$$P(\mathbf{r}) \cong \frac{1}{1 + T_i + T_R} \exp \left[\frac{2r^2}{W^2} (T_i + T_R) \right], \quad (55)$$

and, hence, the mean irradiance (49) for a monostatic channel under weak irradiance fluctuations takes the form

$$\langle I(\mathbf{r}, 2L) \rangle \cong \frac{W_0^2}{W_{LT}^2 (1 + \Omega_R / \Lambda_1)} \exp \left(-\frac{2r^2}{W_{LT}^2} \right) N(\mathbf{r}), \quad (56)$$

where the effective or long-term spot size at the receiver is approximated by

$$W_{LT} = W \sqrt{1 + T_i + T_R}. \quad (57)$$

Equation (57) approximates the effective spot size for both a bistatic system and a monostatic system. It also is the same for a smooth plane reflector (mirror) or a retroreflector. In the limit of a point reflector defined by $\Omega_R \rightarrow \infty$ (see also Section 13.7), we find that $\Theta_2 = \Lambda_2 = 0$ in Eqs. (53) and (54).

13.4.3 Backscatter correlation function: Gaussian-beam wave

The factor $N(\mathbf{r}) \equiv N(\mathbf{r}, \mathbf{r})$ appearing in Eq. (56) is the same quantity defined above by Eq. (37), viz.,

$$N(\mathbf{r}) \equiv \langle C(\mathbf{r}) \rangle = \exp[B_I^{iR}(\mathbf{r}, L)], \quad (58)$$

where $B_I^{iR}(\mathbf{r}, L) \equiv B_{\Gamma}^{iR}(\mathbf{r}, \mathbf{r}, L)$. For the general case of a *Gaussian-beam wave* incident on a finite smooth reflector, the correlation function can be expressed as

$$\begin{aligned}
 B_I^{iR}(\mathbf{r}, L) = & 4\pi^2 k^2 L \int_0^1 \int_0^\infty \kappa \Phi_n(\kappa) J_0[(\gamma_a^i \mp \gamma_a^{R*})\kappa r] \\
 & \times \exp\left\{-\frac{j\kappa^2}{2k} [\gamma_a^i B_a^i(\xi) - \gamma_a^{R*} B_a^{R*}(\xi)]\right\} d\kappa d\xi \\
 & + 4\pi^2 k^2 L \int_0^1 \int_0^\infty \kappa \Phi_n(\kappa) J_0[(\gamma_a^R \mp \gamma_a^{i*})\kappa r] \\
 & \times \exp\left\{\frac{j\kappa^2}{2k} [\gamma_a^{i*} B_a^{i*}(\xi) - \gamma_a^R B_a^R(\xi)]\right\} d\kappa d\xi \\
 & - 4\pi^2 k^2 L \int_0^1 \int_0^\infty \kappa \Phi_n(\kappa) J_0(\gamma_b^R r \kappa) \\
 & \times \exp\left\{-\frac{j\kappa^2}{2k} [\gamma_b^i B_b^i(\xi) + \gamma_b^R B_b^R(\xi)]\right\} d\kappa d\xi \\
 & - 4\pi^2 k^2 L \int_0^1 \int_0^\infty \kappa \Phi_n(\kappa) J_0(\gamma_b^{R*} r \kappa) \\
 & \times \exp\left\{\frac{j\kappa^2}{2k} [\gamma_b^{i*} B_b^{i*}(\xi) + \gamma_b^{R*} B_b^{R*}(\xi)]\right\} d\kappa d\xi.
 \end{aligned} \tag{59}$$

The first two integral pairs arise from the folded-path representation of the complex phase perturbation and the last two integral pairs come from the reciprocal path representation. Also, the upper signs in the arguments of the first two Bessel functions are associated with the plane mirror reflector and the lower signs with the retroreflector. Because of the complexity of Eq. (59), we will develop explicit expressions for it only for the limiting cases of a spherical wave or a plane wave.

13.4.4 Incident spherical wave

In this section we will restrict the analysis to an incident spherical wave as the illumination source. A point source or *spherical wave* at the transmitter is characterized by $\Theta_1 = \Lambda_1 = 0$. Hence, it follows that $\Theta = \Lambda = 0$ and

$$\Theta_2 = \frac{2}{4 + \Omega_R^2}, \quad \Lambda_2 = \frac{\Omega_R}{4 + \Omega_R^2}. \tag{60}$$

The irradiance at the receiver in the absence of turbulence becomes

$$I^0(\mathbf{r}, 2L) = \frac{1}{4 + \Omega_R^2} \exp\left(-\frac{2r^2}{W^2}\right), \tag{61}$$

where the corresponding free-space spot size of the reflected wave is

$$W = W_R \sqrt{4 + \Omega_R^2}. \quad (62)$$

Equation (51) for the reflected spherical wave in optical turbulence reduces to

$$P(\mathbf{r}) = \exp \left\{ -8\pi^2 k^2 L \int_0^1 \int_0^\infty \kappa \Phi_n(\kappa) \left[1 - I_0(2\Lambda_2 \kappa \xi r) \exp \left(-\frac{\Lambda_2 L \kappa^2 \xi^2}{k} \right) \right] d\kappa d\xi \right\}. \quad (63)$$

Hence, following the technique that led to Eq. (56), the mean irradiance (49) for a monostatic system can be approximated by

$$\langle I(\mathbf{r}, 2L) \rangle \cong \frac{W_R^2}{W_{LT}^2} \exp \left(-\frac{2r^2}{W_{LT}^2} \right) \exp [B_I^{iR}(\mathbf{r}, L)], \quad (64)$$

where, based on a Kolmogorov spectrum, the long-term spot size (57) is approximately³

$$W_{LT} = W_R \sqrt{4 + \Omega_R^2} \sqrt{1 + 2.65 \sigma_1^2(L) \left(\frac{\Omega_R}{4 + \Omega_R^2} \right)^{5/6}}. \quad (65)$$

The correlation function appearing in Eq. (64) for a *plane mirror target* is

$$\begin{aligned} B_I^{iR}(\mathbf{r}, L) = & 8\pi^2 k^2 L \int_0^1 \int_0^\infty \kappa \Phi_n(\kappa) \exp \left(-\frac{\Lambda_2 L \kappa^2 \xi^2}{k} \right) \operatorname{Re} \{ J_0[(1 - \xi + 2j\Lambda_2 \xi) \kappa r] \} d\kappa d\xi \\ & - 8\pi^2 k^2 L \int_0^1 \int_0^\infty \kappa \Phi_n(\kappa) J_0(\kappa \xi r) \cos \left[\frac{L \kappa^2}{k} \xi(1 - \xi) \right] d\kappa d\xi, \end{aligned} \quad (66)$$

where Re denotes the real part of the argument. Notice that (66) depends on the Fresnel ratio Λ_2 of the reflected wave but not on the curvature parameter Θ_2 . Thus, the finite size of the reflector plays a critical role. In particular, for $r = 0$ and a Kolmogorov spectrum, Eq. (66) yields

$$B_I^{iR}(0, L) = (0.4 - 2.65 \Lambda_2^{5/6}) \sigma_1^2(L), \quad (67)$$

which is less than or equal to the scintillation index of the incident spherical wave, $B_I^{iR}(0, L) = \sigma_{I, \text{sp}}^2(L) = 0.4 \sigma_1^2(L)$. Because $\Lambda_2 = 0$ in the case of a point reflector ($\Omega_R \gg 1$) or an unbounded mirror ($\Omega_R \ll 1$), Eq. (66) in these limiting cases simplifies to

$$\begin{aligned} B_I^{iR}(\mathbf{r}, L) = & B_{I, \text{sp}}(\mathbf{r}, L) \\ = & 8\pi^2 k^2 L \int_0^1 \int_0^\infty \kappa \Phi_n(\kappa) J_0(\kappa \xi r) \left\{ 1 - \cos \left[\frac{L \kappa^2}{k} \xi(1 - \xi) \right] \right\} d\kappa d\xi, \end{aligned} \quad (68)$$

³In this chapter we will use the notation $\sigma_1^2(L)$ for the Rytov variance $\sigma_R^2(L) = 1.23 C_n^2 k^{7/6} L^{11/6}$ to avoid confusion with other quantities with the subscript R .

where $B_{I,\text{sp}}(\mathbf{r}, L)$ is the same as the covariance function of the incident spherical wave (see Chap. 8). Consequently, when $r = 0$ the on-axis correlation function (68) reduces to the scintillation index associated with that of the incident spherical wave.

For a *retroreflector*, the corresponding correlation function in (64) is

$$B_I^{iR}(\mathbf{r}, L) = 8\pi^2 k^2 L \int_0^1 \int_0^\infty \kappa \Phi_n(\kappa) \left\{ J_0[(1 - \xi + 2\Theta_2 \xi)\kappa r] \exp\left(-\frac{\Lambda_2 L \kappa^2 \xi^2}{k}\right) - \text{Re} \left[J_0[(1 - \xi + 2\Theta_2 \xi - 2j\Lambda_2 \xi)\kappa r] \exp\left(-\frac{2\Lambda_2 L \kappa^2 \xi^2}{k}\right) \times \exp\left[-\frac{jL\kappa^2}{k} \xi(1 - \xi + 2\Theta_2 \xi)\right] \right] \right\} d\kappa d\xi. \quad (69)$$

For a point retroreflector, Eq. (69) reduces to (68), but as the size of the retroreflector becomes unbounded, we have $\Theta_2 = 1/2$, $\Lambda_2 = 0$ and Eq. (69) simplifies to

$$B_I^{iR}(\mathbf{r}, L) = B_{I,\text{pl}}(\mathbf{r}, L) = 8\pi^2 k^2 L \int_0^1 \int_0^\infty \kappa \Phi_n(\kappa) J_0(\kappa r) \left[1 - \cos\left(\frac{L\kappa^2 \xi}{k}\right) \right] d\kappa d\xi, \quad (70)$$

which reveals that the amplitude enhancement associated with a spherical wave reflected from an unbounded retroreflector is governed by the covariance function of a plane wave. Thus, based on the Komogorov spectrum and $r = 0$, Eq. (70) reduces to $B_I^{iR}(0, L) = \sigma_1^2(L)$. Also, under the assumption of the Kolmogorov spectrum, the more general correlation function (69) along the optical axis ($r = 0$) can be closely approximated by

$$B_I^{iR}(0, L) \cong 1.54\sigma_1^2(L) \times \left\{ [(1 + 4\Theta_2)^2 + 16\Lambda_2^2]^{5/12} \cos\left[\frac{5}{6} \tan^{-1}\left(\frac{1 + 4\Theta_2}{4\Lambda_2}\right)\right] - 1.72\Lambda_2^{5/6} \right\}. \quad (71)$$

In Fig. 13.4 the scaled quantity $B_I^{iR}(0, L)/\sigma_1^2(L)$, based on a Kolmogorov spectrum, is shown (solid curves) as a function of the reflector size Ω_R for both a plane mirror [Eq. (67)] and a retroreflector [Eq. (71)]. For certain finite reflectors this quantity is negative for a plane mirror (no amplitude enhancement), whereas it is always positive for a retroreflector and maximum near $\Omega_R = 1$. Hence, there is *always amplitude enhancement* for any size retroreflector. The influence of inner scale and modified atmospheric spectrum [Eq. (22) in Chap. 3] on the correlation functions (66) and (69) at the optical axis ($r = 0$) is shown, respectively, in Figs. 13.5 and 13.6 with several values of the inner scale parameter $Q_I = L\kappa_l^2/k = 10.89L/kl_0^2$. The outer scale is assumed to be infinite. It can clearly be seen that the combination of inner scale and high wave number rise in the spectrum can lead to significantly greater values of the correlation function (particularly near $\Omega_R = 1$) than those predicted by the power law spectrum ($Q_I = \infty$).

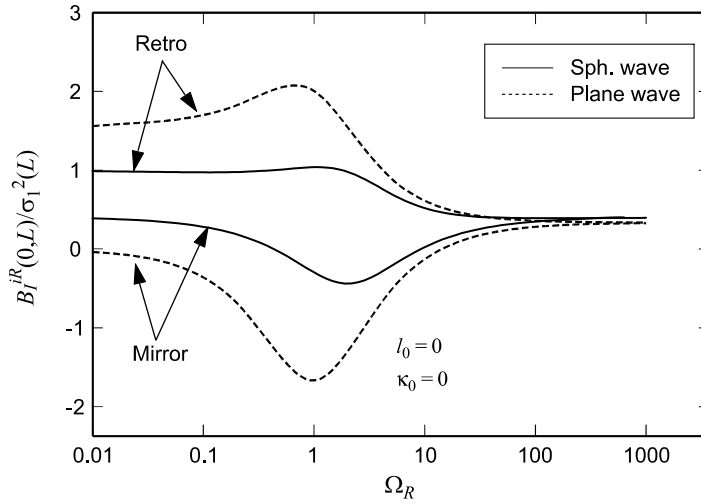


Figure 13.4 The scaled correlation function for the mean irradiance (on the optical axis $r = 0$) at the receiver as a function of reflector size for an incident spherical wave (solid line) and an incident plane wave (dotted line). The upper curves arise from a retroreflector and the lower curves from a plane mirror. All results are based on the Kolmogorov spectrum.

In Fig. 13.7 the mean irradiance $\langle I(\mathbf{r}, 2L) \rangle$ [Eq. (64)], scaled by the on-axis irradiance in the absence of turbulence $I^0(0, 2L)$ [Eq. (61)], is shown for a finite retroreflector ($\Omega_R = 1$) and same size plane mirror as a function of the scaled transverse distance $(kr^2/L)^{1/2}$. The spectral model is that of Kolmogorov and

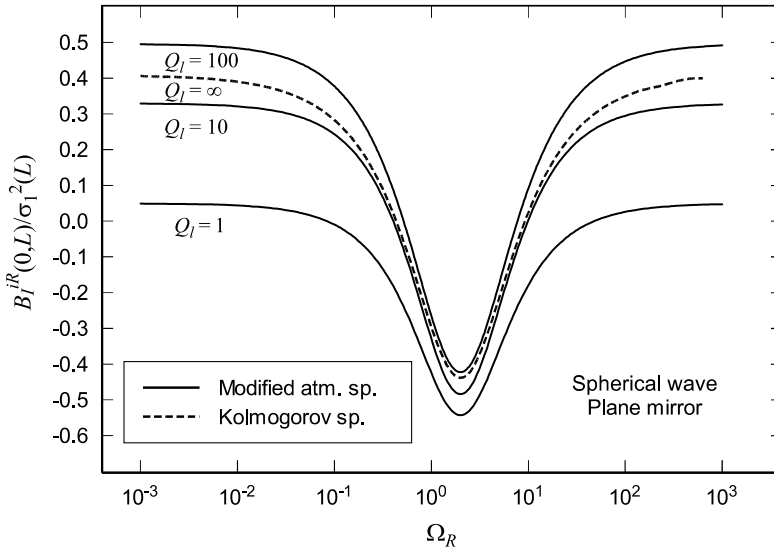


Figure 13.5 The scaled correlation function for the backscatter amplification factor (on the optical axis $r = 0$) at the receiver as a function of reflector size and inner scale for an incident spherical wave.

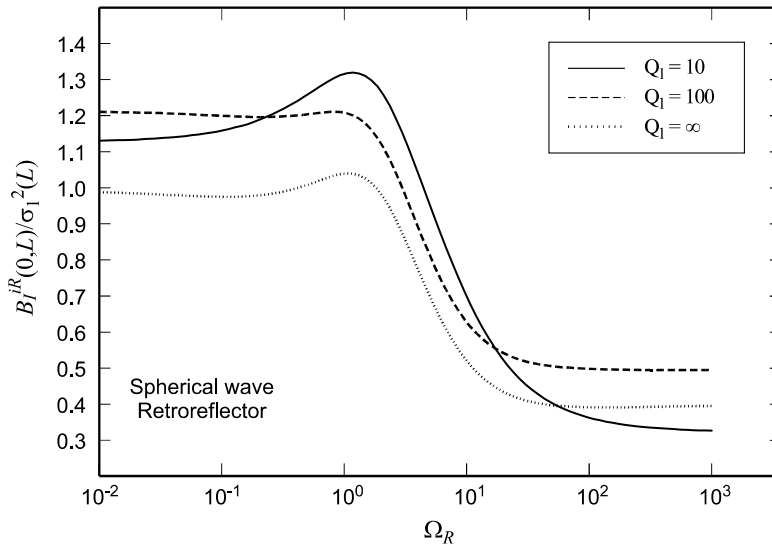


Figure 13.6 Same as Fig. 13.5 for a retroreflector target.

$\sigma_1^2(L) = 0.2$. The solid curves correspond to the monostatic configuration, and illustrate the redistribution of energy in the beam along the optical axis caused by the atmosphere. For contrast, the dashed curve represents the mean irradiance in the absence of the mutual correlations caused by the atmospheric turbulence or,

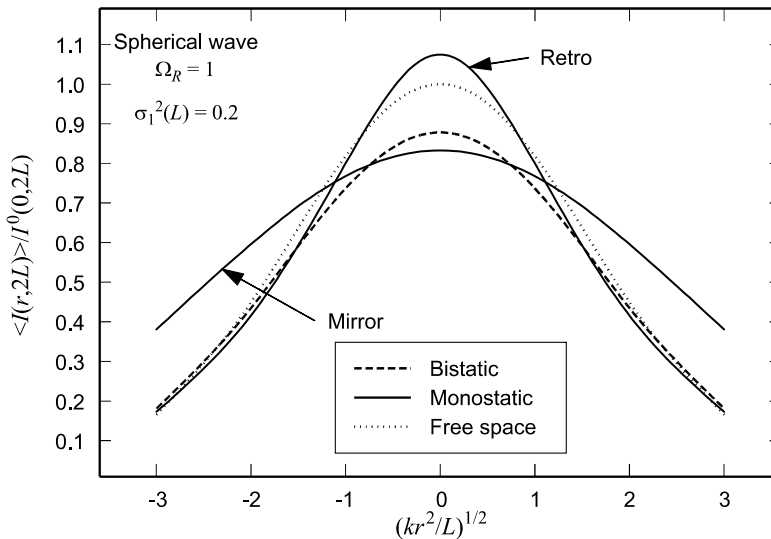


Figure 13.7 The scaled mean irradiance at the receiver as a function of normalized transverse distance from the optical axis of a reflected spherical wave from a finite retroreflector and finite plane mirror, both characterized by $\Omega_R = 1$. The results are based on the Kolmogorov spectrum, and the Rytov variance for a target at range L is taken to be $\sigma_1^2(L) = 0.2$. The dotted curve represents the diffractive or free-space profile of the reflected wave.

equivalently, the bistatic case of a plane mirror. The dotted curve is the normalized irradiance in the absence of atmospheric turbulence obtained from Eq. (61). The width of the enhancement peak (at the intersection points) for the finite retroreflector ($\Omega_R = 1$) is roughly $3(L/k)^{1/2}$. For smaller reflectors the width of this enhancement peak tends to increase, whereas it decreases as the size of the reflector increases.

13.4.5 Incident plane wave

For an *unbounded plane wave* ($\Theta_1 = 1$, $\Lambda_1 = 0$) incident on a finite smooth reflector, it follows that

$$\Theta = \Theta_2 = \frac{1}{1 + \Omega_R^2}, \quad \Lambda = \Lambda_2 = \frac{\Omega_R}{1 + \Omega_R^2}. \quad (72)$$

In this case, the irradiance of the reflected plane wave at the receiver in the absence of optical turbulence is

$$I^0(\mathbf{r}, 2L) = \frac{1}{1 + \Omega_R^2} \exp\left(-\frac{2r^2}{W^2}\right), \quad (73)$$

where the corresponding free-space spot size is

$$W = W_R \sqrt{1 + \Omega_R^2}. \quad (74)$$

The angular spread of the wave caused by the optical turbulence is described by

$$P(\mathbf{r}) = \exp\left\{-4\pi^2 k^2 L \int_0^\infty \kappa \Phi_n(\kappa) \left[1 - I_0(2\Lambda_2 \kappa r) \exp\left(-\frac{\Lambda_2 L \kappa^2}{k}\right)\right] d\kappa \right. \\ \left. - 4\pi^2 k^2 L \int_0^1 \int_0^\infty \kappa \Phi_n(\kappa) \left[1 - I_0(2\Lambda_2 \xi \kappa r) \exp\left(-\frac{\Lambda_2 L \kappa^2 \xi^2}{k}\right)\right] d\kappa d\xi \right\}. \quad (75)$$

From this expression, once again we deduce that the mean irradiance has the form

$$\langle I(\mathbf{r}, 2L) \rangle \cong \frac{W_R^2}{W_{LT}^2} \exp\left(-\frac{2r^2}{W_{LT}^2}\right) \exp[B_I^{iR}(\mathbf{r}, L)], \quad (76)$$

where the long-term spot size (based on the Kolmogorov spectrum) is given by the approximate expression [see Eq. (57)]

$$W_{LT} = W \sqrt{1 + 4.87 \sigma_1^2(L) \Lambda_2^{5/6}} \\ = W_R \sqrt{1 + \Omega_R^2} \sqrt{1 + 4.87 \sigma_1^2(L) \left(\frac{\Omega_R}{1 + \Omega_R^2}\right)^{5/6}}. \quad (77)$$

Thus, the additional spread in the long-term spot size (caused by optical turbulence) of a reflected plane wave is generally less than that of a corresponding reflected spherical wave except for very small targets [see Eq. (65)].

For a *plane mirror reflector*, the correlation function appearing in Eq. (76) becomes

$$\begin{aligned}
 B_I^{iR}(\mathbf{r}, L) = & 8\pi^2 k^2 L \int_0^1 \int_0^\infty \kappa \Phi_n(\kappa) \exp\left[-\frac{\Lambda_2 L \kappa^2 (1 + \xi^2)}{2k}\right] \\
 & \times \operatorname{Re}\left\{J_0[(1 - \Theta_2 + j\Lambda_2 - \bar{\Theta}_2 \xi + j\Lambda_2 \xi)\kappa r]\right. \\
 & \times \exp\left[-\frac{jL\kappa^2}{2k}(1 + \Theta_2 - 2\xi + \bar{\Theta}_2 \xi^2)\right]\Big\} d\kappa d\xi \\
 & - 8\pi^2 k^2 L \int_0^1 \int_0^\infty \kappa \Phi_n(\kappa) \exp\left(-\frac{\Lambda_2 L \kappa^2 \xi^2}{2k}\right) \\
 & \times \operatorname{Re}\left\{J_0[(\bar{\Theta}_2 + j\Lambda_2)\kappa \xi r] \exp\left[-\frac{jL\kappa^2}{2k}\xi(2 - \bar{\Theta}_2 \xi)\right]\right\} d\kappa d\xi,
 \end{aligned} \tag{78}$$

whereas, in the case of a *retroreflector*, the correlation function is

$$\begin{aligned}
 B_I^{iR}(\mathbf{r}, L) = & 8\pi^2 k^2 L \int_0^1 \int_0^\infty \kappa \Phi_n(\kappa) \exp\left[-\frac{\Lambda_2 L \kappa^2 (1 + \xi^2)}{2k}\right] \\
 & \times \operatorname{Re}\left\{J_0[(1 + \Theta_2 - j\Lambda_2 - \bar{\Theta}_2 \xi + j\Lambda_2 \xi)\kappa r]\right. \\
 & \times \exp\left[-\frac{jL\kappa^2}{2k}(1 - \xi)(1 + \Theta_2 - \bar{\Theta}_2 \xi)\right] \\
 & - J_0[(1 + \Theta_2 - j\Lambda_2 - \bar{\Theta}_2 \xi - j\Lambda_2 \xi)\kappa r] \\
 & \times \exp\left[-\frac{jL\kappa^2}{2k}(1 + \xi)(1 + \Theta_2 - \bar{\Theta}_2 \xi)\right]\Big\} d\kappa d\xi.
 \end{aligned} \tag{79}$$

In Fig. 13.4 the scaled quantity $B_I^{iR}(0, L)/\sigma_1^2(L)$ deduced from (78) and (79) appears as a dotted curve for both a retroreflector and a plane mirror (based on the Kolmogorov spectrum). Inner scale and outer scale effects for this case are similar to those based on an incident spherical wave (see Figs. 13.5 and 13.6), but are not separately illustrated.

For the special case of an unbounded retroreflector ($\Omega_R = 0$), Eq. (79) reduces to

$$\begin{aligned}
 B_I^{iR}(\mathbf{r}, L) = & 8\pi^2 k^2 L \int_0^1 \int_0^\infty \kappa \Phi_n(\kappa) J_0(2\kappa r) \\
 & \times \left\{ \cos\left(\frac{L\kappa^2 \xi}{k}\right) - \cos\left[\frac{L\kappa^2}{k}(2 - \xi)\right] \right\} d\kappa d\xi,
 \end{aligned} \tag{80}$$

from which the on-axis value $B_I^{iR}(0, L) = 1.56\sigma_1^2(L)$ is obtained by using the Kolmogorov power law spectrum. However, for an unbounded plane mirror, no

amplitude enhancement is associated with an incident plane wave [1,4]. To see this, we set $\Theta_2 = 1$ and $\Lambda_2 = 0$ in Eq. (78), which leads to

$$\begin{aligned} B_I^{iR}(\mathbf{r}, L) = & 8\pi^2 k^2 L \int_0^1 \int_0^\infty \kappa \Phi_n(\kappa) \exp\left[-\frac{jL\kappa^2}{k}(1-\xi)\right] d\kappa d\xi \\ & - 8\pi^2 k^2 L \int_0^1 \int_0^\infty \kappa \Phi_n(\kappa) \exp\left(-\frac{jL\kappa^2}{k}\xi\right) d\kappa d\xi, \end{aligned} \quad (81)$$

and then by replacing ξ with $1 - \xi$ in the first integral, we see that the correlation function vanishes everywhere.

13.5 Finite Smooth Target—Part II

In the previous section we examined the mean irradiance of a reflected optical wave from a finite smooth target. In doing so, we showed that the BSAE associated with a monostatic channel includes effects from folded-path correlations as well as reciprocal-path correlations. However, reciprocal-path correlations always dominate in the case of a retroreflector of any size so the BSAE is always present. For a plane smooth reflector, the reciprocal-path correlations dominate the folded-path correlations only when $\Omega_R \gg 1$ or $\Omega_R \ll 1$. For targets in which $\Omega_R \sim 1$ the folded-path correlations are dominant, which produces the opposite effect from an intensity enhancement. Moreover, as we will see below in the case of normalized statistics like the scintillation index and the modulus of the complex degree of coherence (Section 13.6), the reciprocal-path terms cancel so that only the folded-path terms remain.

The general *fourth-order cross-coherence function* associated with a reflected Gaussian-beam wave is defined by the ensemble average

$$\begin{aligned} \Gamma_4(\mathbf{r}_1, \mathbf{r}_2, \mathbf{r}_3, \mathbf{r}_4, 2L) &= \langle U(\mathbf{r}_1, 2L)U^*(\mathbf{r}_2, 2L)U(\mathbf{r}_3, 2L)U^*(\mathbf{r}_4, 2L) \rangle \\ &= \Gamma_4^0(\mathbf{r}_1, \mathbf{r}_2, \mathbf{r}_3, \mathbf{r}_4, 2L)M_4(\mathbf{r}_1, \mathbf{r}_2, \mathbf{r}_3, \mathbf{r}_4, 2L), \end{aligned} \quad (82)$$

where $\Gamma_4^0(\mathbf{r}_1, \mathbf{r}_2, \mathbf{r}_3, \mathbf{r}_4, 2L) = U_0(\mathbf{r}_1, 2L)U_0^*(\mathbf{r}_2, 2L)U_0(\mathbf{r}_3, 2L)U_0^*(\mathbf{r}_4, 2L)$ and

$$M_4(\mathbf{r}_1, \mathbf{r}_2, \mathbf{r}_3, \mathbf{r}_4, 2L) = \langle \exp[\psi(\mathbf{r}_1, 2L) + \psi^*(\mathbf{r}_2, 2L) + \psi(\mathbf{r}_3, 2L) + \psi^*(\mathbf{r}_4, 2L)] \rangle, \quad (83)$$

the latter of which describes the effects of atmospheric turbulence. By calculating the expected value in Eq. (83), it can be expressed in the form (omitting the path length argument for notational simplicity)

$$\begin{aligned}
M_4(\mathbf{r}_1, \mathbf{r}_2, \mathbf{r}_3, \mathbf{r}_4) &= M_2(\mathbf{r}_1, \mathbf{r}_2)M_2(\mathbf{r}_3, \mathbf{r}_4) \\
&\times \exp \left[\langle \psi_a^i(\pm \mathbf{r}_1) \psi_a^{i*}(\pm \mathbf{r}_4) \rangle + \langle \psi_a^R(\mathbf{r}_1) \psi_a^{R*}(\mathbf{r}_4) \rangle \right. \\
&\quad + \langle \psi_a^i(\pm \mathbf{r}_3) \psi_a^{i*}(\pm \mathbf{r}_2) \rangle + \langle \psi_a^R(\mathbf{r}_3) \psi_a^{R*}(\mathbf{r}_2) \rangle \\
&\quad + \langle \psi_a^i(\pm \mathbf{r}_1) \psi_a^i(\pm \mathbf{r}_3) \rangle + \langle \psi_a^R(\mathbf{r}_1) \psi_a^R(\mathbf{r}_3) \rangle \\
&\quad \left. + \langle \psi_a^{i*}(\pm \mathbf{r}_2) \psi_a^{i*}(\pm \mathbf{r}_4) \rangle + \langle \psi_a^{R*}(\mathbf{r}_2) \psi_a^{R*}(\mathbf{r}_4) \rangle \right] \quad (84) \\
&\times \exp \left[\langle \psi_a^i(\pm \mathbf{r}_1) \psi_a^{R*}(\mathbf{r}_4) \rangle + \langle \psi_a^R(\mathbf{r}_1) \psi_a^{i*}(\pm \mathbf{r}_4) \rangle \right. \\
&\quad + \langle \psi_a^i(\pm \mathbf{r}_3) \psi_a^{R*}(\mathbf{r}_2) \rangle + \langle \psi_a^R(\mathbf{r}_3) \psi_a^{i*}(\pm \mathbf{r}_2) \rangle \\
&\quad + \langle \psi_a^i(\pm \mathbf{r}_1) \psi_a^R(\mathbf{r}_3) \rangle + \langle \psi_a^R(\mathbf{r}_1) \psi_a^i(\pm \mathbf{r}_3) \rangle \\
&\quad \left. + \langle \psi_a^{i*}(\pm \mathbf{r}_2) \psi_a^{R*}(\mathbf{r}_4) \rangle + \langle \psi_a^{R*}(\mathbf{r}_2) \psi_a^{i*}(\pm \mathbf{r}_4) \rangle \right],
\end{aligned}$$

where the upper signs are associated with a plane mirror reflector, the lower signs with a retroreflector, and where $M_2(\mathbf{r}_1, \mathbf{r}_2) = \langle \exp[\psi(\mathbf{r}_1, 2L) + \psi^*(\mathbf{r}_2, 2L)] \rangle = P(\mathbf{r}_1, \mathbf{r}_2) \times N(\mathbf{r}_1, \mathbf{r}_2)$ is the second-order moment arising from the complex phase perturbations (Section 13.4). Here, we are primarily concerned only with normalized quantities that do not directly involve the second-order moment $M_2(\mathbf{r}_1, \mathbf{r}_2)$ nor, therefore, the reciprocal-path phase perturbation $\psi_b(\mathbf{r}, L)$. That is, only folded-path terms arise in our analysis in this section.

A useful specialization of the general fourth-order coherence function (82) is

$$\Gamma_4(\mathbf{r}_1, \mathbf{r}_1, \mathbf{r}_2, \mathbf{r}_2, 2L) = \langle I(\mathbf{r}_1, 2L) \rangle \langle I(\mathbf{r}_2, 2L) \rangle \exp[4B_\chi(\mathbf{r}_1, \mathbf{r}_2, 2L)], \quad (85)$$

where $\langle I(\mathbf{r}, 2L) \rangle$ denotes the mean irradiance. The function $B_\chi(\mathbf{r}_1, \mathbf{r}_2, 2L)$ appearing in Eq. (85) is the *covariance function of log amplitude* defined by

$$\begin{aligned}
B_\chi(\mathbf{r}_1, \mathbf{r}_2, 2L) &= \frac{1}{2} \text{Re} \left[\langle \psi_a^i(\pm \mathbf{r}_1) \psi_a^{i*}(\pm \mathbf{r}_2) \rangle + \langle \psi_a^i(\pm \mathbf{r}_1) \psi_a^i(\pm \mathbf{r}_2) \rangle \right] \\
&\quad + \frac{1}{2} \text{Re} \left[\langle \psi_a^R(\mathbf{r}_1) \psi_a^{R*}(\mathbf{r}_2) \rangle + \langle \psi_a^R(\mathbf{r}_1) \psi_a^R(\mathbf{r}_2) \rangle \right] \\
&\quad + \frac{1}{2} \text{Re} \left[\langle \psi_a^i(\pm \mathbf{r}_1) \psi_a^{R*}(\mathbf{r}_2) \rangle + \langle \psi_a^R(\mathbf{r}_1) \psi_a^{i*}(\pm \mathbf{r}_2) \rangle \right. \\
&\quad \left. + \langle \psi_a^i(\pm \mathbf{r}_1) \psi_a^R(\mathbf{r}_2) \rangle + \langle \psi_a^R(\mathbf{r}_1) \psi_a^i(\pm \mathbf{r}_2) \rangle \right]. \quad (86)
\end{aligned}$$

For statistically homogeneous and isotropic turbulence, the second-order moments of the complex phase perturbations appearing in (86) can be expressed in integral form as [see also Eq. (44)]

$$\begin{aligned}
& \langle \psi_a^i(\pm \mathbf{r}_1) \psi_a^i(\pm \mathbf{r}_2) \rangle + \langle \psi_a^R(\mathbf{r}_1) \psi_a^R(\mathbf{r}_2) \rangle \\
&= -4\pi^2 k^2 L \int_0^1 \int_0^\infty \kappa \Phi_n(\kappa) J_0(|\mathbf{r}_1 - \mathbf{r}_2| \gamma_a^i \kappa) \exp \left[-\frac{j\kappa^2}{k} \gamma_a^i B_a^i(\xi) \right] d\kappa d\xi \\
&\quad - 4\pi^2 k^2 L \int_0^1 \int_0^\infty \kappa \Phi_n(\kappa) J_0(|\mathbf{r}_1 - \mathbf{r}_2| \gamma_a^R \kappa) \exp \left[-\frac{j\kappa^2}{k} \gamma_a^R B_a^R(\xi) \right] d\kappa d\xi, \tag{87}
\end{aligned}$$

$$\begin{aligned}
& \langle \psi_a^i(\pm \mathbf{r}_1) \psi_a^{R*}(\mathbf{r}_2) \rangle + \langle \psi_a^R(\mathbf{r}_1) \psi_a^{i*}(\pm \mathbf{r}_2) \rangle \\
&= 4\pi^2 k^2 L \int_0^1 \int_0^\infty \kappa \Phi_n(\kappa) J_0(|\gamma_a^i \mathbf{r}_1 \mp \gamma_a^{R*} \mathbf{r}_2| \kappa) \exp \left\{ -\frac{j\kappa^2}{k} [\gamma_a^i B_a^i(\xi) - \gamma_a^{R*} B_a^{R*}(\xi)] \right\} d\kappa d\xi \\
&\quad + 4\pi^2 k^2 L \int_0^1 \int_0^\infty \kappa \Phi_n(\kappa) J_0(|\gamma_a^R \mathbf{r}_1 \mp \gamma_a^{i*} \mathbf{r}_2| \kappa) \exp \left\{ \frac{j\kappa^2}{k} [\gamma_a^{i*} B_a^{i*}(\xi) - \gamma_a^R B_a^R(\xi)] \right\} d\kappa d\xi, \tag{88}
\end{aligned}$$

$$\begin{aligned}
& \langle \psi_a^i(\pm \mathbf{r}_1) \psi_a^R(\mathbf{r}_2) \rangle + \langle \psi_a^R(\mathbf{r}_1) \psi_a^i(\pm \mathbf{r}_2) \rangle \\
&= -4\pi^2 k^2 L \int_0^1 \int_0^\infty \kappa \Phi_n(\kappa) J_0(|\gamma_a^i \mathbf{r}_1 \mp \gamma_a^R \mathbf{r}_2| \kappa) \exp \left\{ -\frac{j\kappa^2}{k} [\gamma_a^i B_a^i(\xi) + \gamma_a^R B_a^R(\xi)] \right\} d\kappa d\xi \\
&\quad - 4\pi^2 k^2 L \int_0^1 \int_0^\infty \kappa \Phi_n(\kappa) J_0(|\gamma_a^R \mathbf{r}_1 \mp \gamma_a^i \mathbf{r}_2| \kappa) \exp \left\{ -\frac{j\kappa^2}{k} [\gamma_a^R B_a^R(\xi) + \gamma_a^i B_a^i(\xi)] \right\} d\kappa d\xi, \tag{89}
\end{aligned}$$

The *normalized covariance function of irradiance* is defined in terms of the fourth- and second-order coherence functions according to

$$\begin{aligned}
b_I(\mathbf{r}_1, \mathbf{r}_2, 2L) &= \frac{\Gamma_4(\mathbf{r}_1, \mathbf{r}_1, \mathbf{r}_2, \mathbf{r}_2, 2L) - \Gamma_2(\mathbf{r}_1, \mathbf{r}_1, 2L) \Gamma_2(\mathbf{r}_2, \mathbf{r}_2, 2L)}{\Pi_{n=1,2} [\Gamma_4(\mathbf{r}_n, \mathbf{r}_n, \mathbf{r}_n, \mathbf{r}_n, 2L) - \Gamma_2^2(\mathbf{r}_n, \mathbf{r}_n, 2L)]^{1/2}} \\
&\cong \frac{B_\chi(\mathbf{r}_1, \mathbf{r}_2, 2L)}{[B_\chi(\mathbf{r}_1, \mathbf{r}_1, 2L) B_\chi(\mathbf{r}_2, \mathbf{r}_2, 2L)]^{1/2}}. \tag{90}
\end{aligned}$$

The last expression in (90) is a consequence of weak irradiance fluctuations.

13.5.1 Scintillation index: incident beam wave

The normalized variance or *scintillation index* of the reflected irradiance, deduced from the covariance function (86), is given by the quantity

$$\sigma_I^2(\mathbf{r}, 2L) = \exp[4B_\chi(\mathbf{r}, \mathbf{r}, 2L)] - 1, \tag{91}$$

which, under weak irradiance fluctuations, can be approximated by

$$\begin{aligned}\sigma_I^2(\mathbf{r}, 2L) = & 2\text{Re}[\langle \psi_a^i(\pm \mathbf{r}) \psi_a^{i*}(\pm \mathbf{r}) \rangle + \langle \psi_a^i(\pm \mathbf{r}) \psi_a^i(\pm \mathbf{r}) \rangle] \\ & + 2\text{Re}[\langle \psi_a^R(\mathbf{r}) \psi_a^{R*}(\mathbf{r}) \rangle + \langle \psi_a^R(\mathbf{r}) \psi_a^R(\mathbf{r}) \rangle] \\ & + 2\text{Re}[\langle \psi_a^i(\pm \mathbf{r}) \psi_a^{R*}(\mathbf{r}) \rangle + \langle \psi_a^R(\mathbf{r}) \psi_a^{i*}(\pm \mathbf{r}) \rangle] \\ & + \langle \psi_a^i(\pm \mathbf{r}) \psi_a^R(\mathbf{r}) \rangle + \langle \psi_a^R(\mathbf{r}) \psi_a^i(\pm \mathbf{r}) \rangle.\end{aligned}\quad (92)$$

It is well known that the scintillation index of a reflected wave at the optical axis ($r = 0$) is the same for both a retroreflector and a plane mirror [18]. However, at points off the beam axis the behavior of the scintillation index is quite different for the two types of reflectors.

For the general case of a *Gaussian-beam wave* incident on a finite reflector at range L , we find that the *scintillation index* (92) of the reflected wave can be expressed as the sum of three distinct terms, each propagating over a path of length L , viz.,

$$\sigma_I^2(\mathbf{r}, 2L) = \sigma_{I,i}^2(\mathbf{r}, L) + \sigma_{I,\text{beam}}^2(\mathbf{r}, L) + 2C_I^{iR}(\mathbf{r}, L). \quad (93)$$

The first term $\sigma_{I,i}^2(\mathbf{r}, L)$ is associated primarily with the incident beam wave involving the beam parameters Θ_1, Λ_1 of the illumination beam, but also contains target information through the beam parameters Θ_2, Λ_2 . Consequently, it should not be confused with the scintillation index of the illumination beam. It is explicitly defined by

$$\begin{aligned}\sigma_{I,i}^2(\mathbf{r}, 2L) = & 8\pi^2 k^2 L \int_0^1 \int_0^\infty \kappa \Phi_n(\kappa) \\ & \times \exp \left\{ -\frac{L\kappa^2}{k} [(1 - \bar{\Theta}_1 \xi)(\Lambda_2 - \Lambda_2 \xi + \Lambda \xi) + \Lambda_1 \xi (\Theta_2 + \bar{\Theta}_2 \xi + \Theta \xi)] \right\} \\ & \times \left[I_0[2\kappa r (\Lambda_2 - \Lambda_2 \xi + \Lambda \xi)] \right. \\ & \left. - \cos \left\{ \frac{L\kappa^2}{k} [(1 - \bar{\Theta}_1 \xi)(\Theta_2 + \bar{\Theta}_2 \xi + \Theta \xi) - \Lambda_1 \xi (\Lambda_2 - \Lambda_2 \xi + \Lambda \xi)] \right\} \right] d\kappa d\xi.\end{aligned}\quad (94)$$

The second term in (93) is identified with a Gaussian beam propagating from the reflector to the receiver and is described by

$$\begin{aligned}\sigma_{I,\text{beam}}^2(\mathbf{r}, L) = & 8\pi^2 k^2 L \int_0^1 \int_0^\infty \kappa \Phi_n(\kappa) \exp \left(-\frac{\Lambda_2 L \kappa^2 \xi^2}{k} \right) \\ & \times \left\{ I_0(2\Lambda_2 \kappa \xi r) - \cos \left[\frac{L\kappa^2}{k} \xi (1 - \bar{\Theta}_2 \xi) \right] \right\} d\kappa d\xi.\end{aligned}\quad (95)$$

Hence, this component has the same mathematical form as the scintillation index of a Gaussian-beam wave characterized by beam parameters Θ_2, Λ_2 in the plane of the receiver. The remaining term $C_I^{iR}(\mathbf{r}, L)$ in (93) is the *irradiance correlation*

function between incident and reflected waves that evolves through the folded-path terms. For a *plane mirror* reflector, it takes the form

$$\begin{aligned}
 C_I^{iR}(\mathbf{r}, L) = & 8\pi^2 k^2 L \text{Re} \int_0^1 \int_0^\infty \kappa \Phi_n(\kappa) \\
 & \times \exp \left\{ -\frac{jL\kappa^2}{2k} \left[(1 - \bar{\Theta}_1 \xi)(\Theta_2 + \bar{\Theta}_2 \xi + \Theta \xi) - \Lambda_1 \xi (\Lambda_2 - \Lambda_2 \xi + \Lambda \xi) \right] \right\} \\
 & \times \exp \left\{ -\frac{L\kappa^2}{2k} \left[\Lambda_2 (1 - \xi)^2 + \Lambda_1 \xi (\Theta_2 + \bar{\Theta}_2 \xi + \Theta \xi) + (1 - \bar{\Theta}_1 \xi)(\Lambda_2 - \Lambda_2 \xi + \Lambda \xi) \right] \right\} \\
 & \times \left[J_0 \{ \kappa r [(\Theta - j\Lambda)\xi - \xi - 2j\Lambda_2(1 - \xi)] \} \exp \left\{ \frac{jL\kappa^2}{2k} [\xi(1 - \xi) + \Theta_2(1 - \xi)^2] \right\} \right. \\
 & \left. - J_0 \{ \kappa r [(\Theta - j\Lambda)\xi - \xi] \} \exp \left\{ -\frac{jL\kappa^2}{2k} [\xi(1 - \xi) + \Theta_2(1 - \xi)^2] \right\} \right] d\kappa d\xi.
 \end{aligned} \tag{96}$$

The scintillation index described by Eq. (93) is also applicable in the case of a *retroreflected* wave, except in this latter case the irradiance correlation function is

$$\begin{aligned}
 C_I^{iR}(\mathbf{r}, L) = & 8\pi^2 k^2 L \text{Re} \int_0^1 \int_0^\infty \kappa \Phi_n(\kappa) \\
 & \times \exp \left\{ -\frac{jL\kappa^2}{2k} \left[(1 - \bar{\Theta}_1 \xi)(\Theta_2 + \bar{\Theta}_2 \xi + \Theta \xi) - \Lambda_1 \xi (\Lambda_2 - \Lambda_2 \xi + \Lambda \xi) \right] \right\} \\
 & \times \exp \left\{ -\frac{L\kappa^2}{2k} \left[\Lambda_2 (1 - \xi)^2 + \Lambda_1 \xi (\Theta_2 + \bar{\Theta}_2 \xi + \Theta \xi) + (1 - \bar{\Theta}_1 \xi)(\Lambda_2 - \Lambda_2 \xi + \Lambda \xi) \right] \right\} \\
 & \times \left[J_0 \{ \kappa r [(\Theta - j\Lambda)\xi + \xi + 2\Theta_2(1 - \xi)] \} \exp \left\{ \frac{jL\kappa^2}{2k} [\xi(1 - \xi) + \Theta_2(1 - \xi)^2] \right\} \right. \\
 & \left. - J_0 \{ \kappa r [(\Theta - j\Lambda)\xi + \xi + 2(\Theta_2 - j\Lambda_2)(1 - \xi)] \} \right. \\
 & \left. \times \exp \left\{ -\frac{jL\kappa^2}{2k} [\xi(1 - \xi) + \Theta_2(1 - \xi)^2] \right\} \right] d\kappa d\xi.
 \end{aligned} \tag{97}$$

The influence of the refractive index spectral model on the scintillation index at the optical axis of a reflected collimated beam wave, scaled by the Rytov variance $\sigma_1^2(L) = 1.23 C_n^2 k^{7/6} L^{11/6}$, is shown in Fig. 13.8 as a function of target (reflector) size $\Omega_R = 2L/kW_R^2$. Here, we have chosen an illumination beam in which $\Lambda_0 = 2L/kW_0^2 = 1$, for which the beam radius W_0 is roughly equal to the first Fresnel zone size $(L/k)^{1/2}$ at the target, and we picked two inner scale values as defined by the nondimensional parameter $Q_l = L\kappa_l^2/k = 10.89L/kl_0^2$. Results based on the Kolmogorov spectrum ($Q_l = \infty$) are shown for comparison. These curves, valid for both a plane mirror and a retroreflector, show that inner scale and high-wave-number rise in the modified atmospheric spectrum can increase the predicted scintillation index by more than 35% (with $Q_l = 10$) over that predicted by the Kolmogorov spectrum. Outer scale can be ignored in this case.

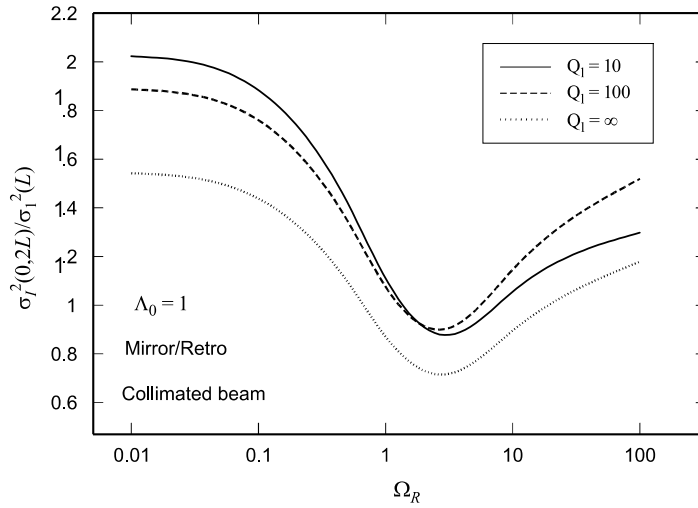


Figure 13.8 The scaled scintillation index on the optical axis for a reflected collimated beam wave as a function of inner scale and normalized reflector size $\Omega_R = 2L/kW_R^2$, where W_0 is the beam radius and W_R is the reflector radius. The case $Q_I = \infty$ corresponds to a Kolmogorov spectrum.

In Fig. 13.9 the scaled scintillation index for a collimated beam ($\Lambda_0 = 1$) is shown as a function of scaled transverse distance from the optical axis $(kr^2/L)^{1/2}$ for various target sizes, $\kappa_0 = 0$, and inner scale parameter $Q_I = 100$. For the small reflector ($\Omega_R = 100$) the spot size of the beam is approximately

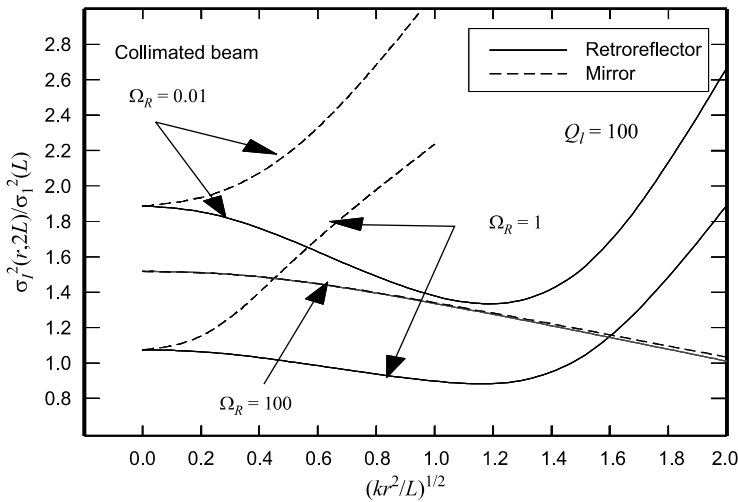


Figure 13.9 The scaled scintillation index of a reflected collimated beam ($\Lambda_0 = 1$) as a function of scaled transverse distance from the optical axis for three reflector sizes. The inner scale parameter is $Q_I = 100$ and outer scale is infinite.

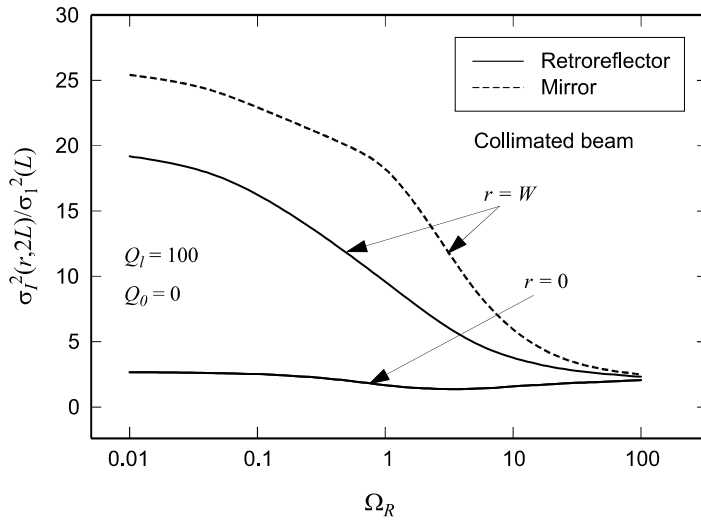


Figure 13.10 The scaled scintillation index for a reflected collimated beam ($\Lambda_0 = 1$) from two types of reflectors. The curves with $r = 0$ correspond to the optical axis and those with $r = W$ represent the diffractive beam edge.

14 times that of the Fresnel zone size, so the behavior depicted in Fig. 13.9 for this target concerns only that part of the beam near the optical axis. However, for the other two target sizes the illustrated behavior is valid out to the diffractive edge of the beam because the diffractive spot size is roughly 3 times that of the Fresnel zone. Note also in all cases that the reflected wave from a plane mirror increases faster in the radial direction away from the optical axis than that for a finite retroreflector. This can be explained by the fact that the correlation function for a finite retroreflector decreases in the radial direction whereas that for a finite mirror increases.

The radial behavior of the scaled scintillation index as a function of reflector size for both types of reflectors is further illustrated in Fig. 13.10 for $r = 0$ and $r = W$, the latter representing the diffractive edge of the reflected beam. On the optical axis the predicted scintillation index is the same for both types of reflectors, but off-axis fluctuations associated with a plane mirror for all $\Omega_R < 10$ are significantly greater than those associated with a retroreflector.

13.5.2 Scintillation index: incident spherical wave

For the limiting case of an incident *spherical wave* ($\Theta_1 = \Lambda_1 = 0$), we find that the scintillation index (93) collapses into a sum of only two terms in the form

$$\sigma_I^2(\mathbf{r}, 2L) = 2\sigma_{I,\text{beam}}^2(\mathbf{r}, L) + 2C_I^{iR}(\mathbf{r}, L), \quad (98)$$

where the first term is defined by (95) and, for a *plane mirror*, the correlation function (96) becomes

$$C_I^{iR}(\mathbf{r}, L) = 8\pi^2 k^2 L \int_0^1 \int_0^\infty \kappa \Phi_n(\kappa) \exp\left(-\frac{\Lambda_2 L \kappa^2 \xi^2}{k}\right) \text{Re} \left\{ J_0[(1 - \xi + 2j\Lambda_2 \xi)\kappa r] - J_0[(1 - \xi)\kappa r] \exp\left[-\frac{jL\kappa^2}{k} \xi(1 - \overline{\Theta}_2 \xi)\right] \right\} d\kappa d\xi. \quad (99)$$

For a *retroreflector* the corresponding correlation function (97) reduces to

$$C_I^{iR}(\mathbf{r}, L) = 8\pi^2 k^2 L \int_0^1 \int_0^\infty \kappa \Phi_n(\kappa) \exp\left(-\frac{\Lambda_2 L \kappa^2 \xi^2}{k}\right) \text{Re} \left\{ J_0[(1 - \xi + 2\Theta_2 \xi)\kappa r] - J_0[(1 - \xi + 2\Theta_2 \xi - 2j\Lambda_2 \xi)\kappa r] \exp\left[-\frac{jL\kappa^2}{k} \xi(1 - \overline{\Theta}_2 \xi)\right] \right\} d\kappa d\xi. \quad (100)$$

Note that on the optical axis in the receiver plane of a monostatic system, both correlation functions (99) and (100) further reduce to

$$\begin{aligned} C_I^{iR}(0, L) &\equiv \sigma_{I, \text{beam}}^2(0, L) \\ &= 8\pi^2 k^2 L \int_0^1 \int_0^\infty \kappa \Phi_n(\kappa) \exp\left(-\frac{\Lambda_2 L \kappa^2 \xi^2}{k}\right) \\ &\quad \times \left\{ 1 - \cos\left[\frac{L\kappa^2}{k} \xi(1 - \overline{\Theta}_2 \xi)\right] \right\} d\kappa d\xi. \end{aligned} \quad (101)$$

Therefore, for $r = 0$ and a Kolmogorov spectrum, Eq. (98) takes the form

$$\begin{aligned} \sigma_I^2(0, 2L) &= 2\sigma_{I, \text{beam}}^2(0, L) + 2C_I^{iR}(0, L) \\ &= 4 \times 3.86 \sigma_1^2 \text{Re} \left[j^{5/6} {}_2F_1\left(-\frac{5}{6}, \frac{11}{6}; \frac{17}{6}; \overline{\Theta}_2 + j\Lambda_2\right) - \frac{11}{16} \Lambda_2^{5/6} \right], \end{aligned} \quad (102)$$

where each component on the right-hand side in (102) is exactly the same. Consequently, the on-axis scintillation index (102) for both types of reflector is *four* times that of a Gaussian-beam wave (characterized by Θ_2, Λ_2) propagating from the mirror to the receiver. The influence of inner scale (based on the modified atmospheric spectrum) on the optical axis of a reflected spherical wave is shown in Fig. 13.11 as a function of reflector size Ω_R under the same conditions cited in Fig. 13.8 for a collimated beam. These curves show that inner scale and high-wave-number rise in the spectrum can increase the predicted scintillation index for an incident spherical wave by more than 20% (with $Q_I = 100$) over that predicted by the Kolmogorov spectrum.

In Fig. 13.12 the scaled scintillation index is shown as a function of $(kr^2/L)^{1/2}$ analogous to that in Fig. 13.9 for a collimated beam. Only the behavior near the beam center is shown for $\Omega_R = 0.01$ and $\Omega_R = 100$ because the spot size of the beam is approximately 28 and 14 times the Fresnel zone size, respectively. However, for $\Omega_R = 1$ the diffractive spot size is only 3 times that of the Fresnel

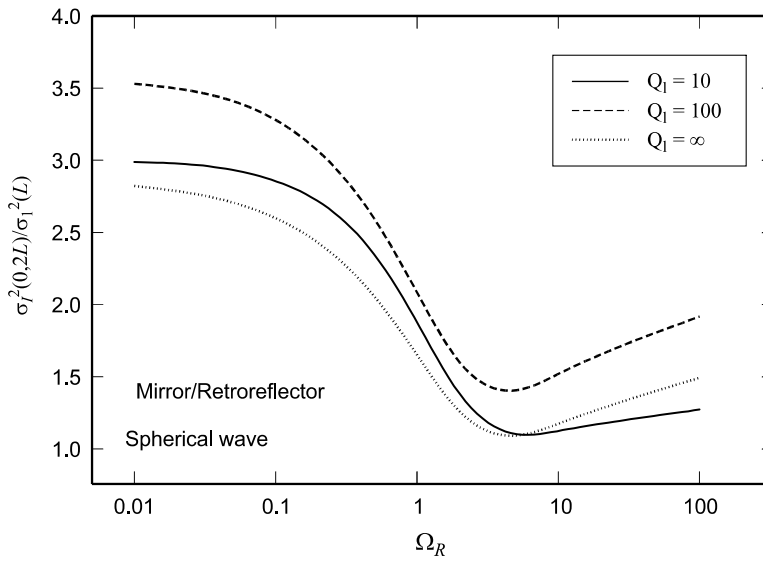


Figure 13.11 Same as Fig. 13.8 for an incident spherical wave.

zone. Figure 13.13 is a repeat of Fig. 13.10 for the incident spherical wave case. Unlike the collimated beam case, here we see that off-axis fluctuations for both types of reflectors are less than on-axis fluctuations for either large ($\Omega_R \ll 1$) or small ($\Omega_R \gg 1$) reflectors. This is caused by the fact that the correlation function represents 50% of the total on-axis fluctuations and off-axis fluctuations are minimal for large and small reflectors. Hence, in such cases the fluctuations

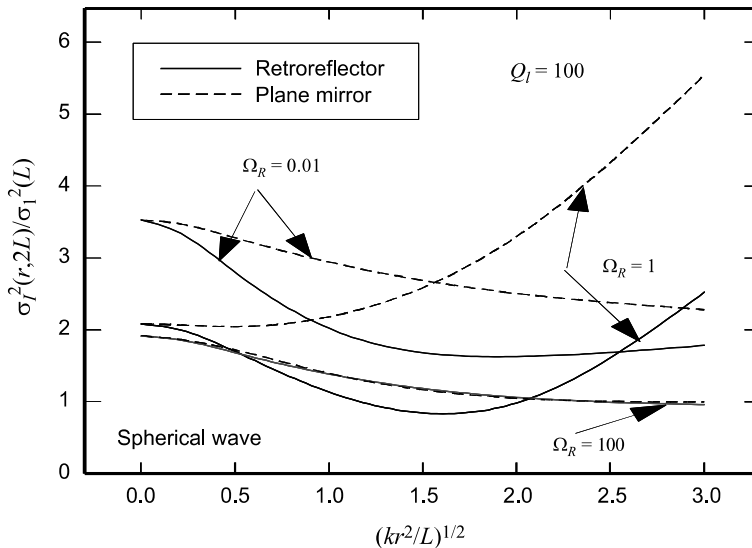


Figure 13.12 Same as Fig. 13.9 for an incident spherical wave.

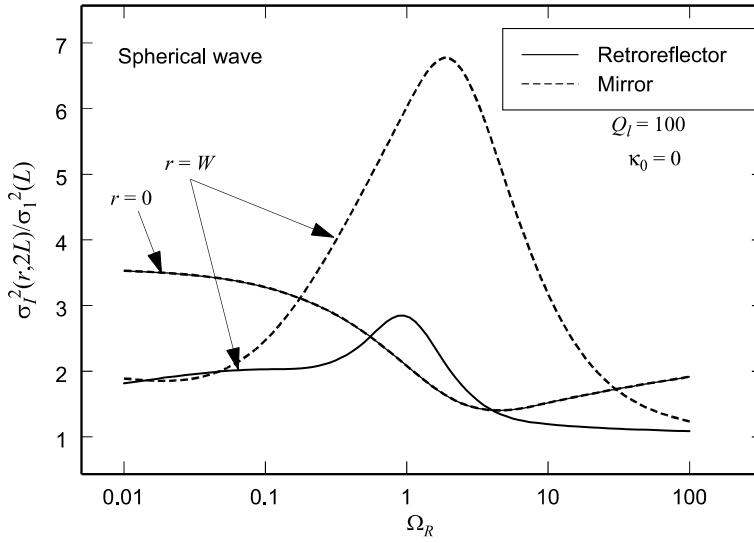


Figure 13.13 Same as Fig. 13.10 for an incident spherical wave.

decrease in the radial direction as the correlation function approaches zero. Last, if the illumination wave is a collimated beam, the correlation function is a small percentage of the total on-axis fluctuations, and off-axis fluctuations are quite large except for sufficiently small targets ($\Omega_R \gg 1$) where the reflected wave acts like a spherical wave.

13.5.3 Scintillation index: incident plane wave

When the incident wave is an unbounded *plane wave* ($\Theta_1 = 1, \Lambda_1 = 0$), the scintillation index of the wave reflected from a smooth reflector takes the form

$$\sigma_I^2(\mathbf{r}, 2L) = \sigma_{I,i}^2(\mathbf{r}, L) + \sigma_{I,\text{beam}}^2(\mathbf{r}, L) + 2C_I^{iR}(\mathbf{r}, L), \quad (103)$$

where the first two terms are defined explicitly by

$$\begin{aligned} \sigma_{I,i}^2(\mathbf{r}, L) &= 8\pi^2 k^2 L \int_0^1 \int_0^\infty \kappa \Phi_n(\kappa) \exp\left(-\frac{\Lambda_2 L \kappa^2}{k}\right) \\ &\quad \times \left\{ I_0(2\Lambda_2 \kappa r) - \cos\left[\frac{L\kappa^2}{k}(1 + \Theta_2 - \xi)\right] \right\} d\kappa d\xi, \end{aligned} \quad (104)$$

$$\begin{aligned} \sigma_{I,\text{beam}}^2(\mathbf{r}, L) &= 8\pi^2 k^2 L \int_0^1 \int_0^\infty \kappa \Phi_n(\kappa) \exp\left(-\frac{\Lambda_2 L \kappa^2 \xi^2}{k}\right) \\ &\quad \times \left\{ I_0(2\Lambda_2 \kappa \xi r) - \cos\left[\frac{L\kappa^2}{k}\xi(1 - \Theta_2 \xi)\right] \right\} d\kappa d\xi. \end{aligned} \quad (105)$$

The remaining term in (103) is the correlation term between incident and reflected waves. In the case of a *plane mirror*, the scintillation index associated with the irradiance correlation is described by

$$\begin{aligned}
 C_I^{iR}(\mathbf{r}, L) = & 8\pi^2 k^2 L \int_0^1 \int_0^\infty \kappa \Phi_n(\kappa) \exp\left[-\frac{\Lambda_2 L \kappa^2}{2k}(1 + \xi^2)\right] \\
 & \times \operatorname{Re}\left\{J_0[(1 - \Theta_2 + j\Lambda_2 - \bar{\Theta}_2 \xi + j\Lambda_2 \xi)\kappa r] \right. \\
 & \times \exp\left[-\frac{jL\kappa^2}{2k}(1 + \Theta_2 - 2\xi + \bar{\Theta}_2 \xi^2)\right] \\
 & - J_0[(1 - \Theta_2 + j\Lambda_2 - \bar{\Theta}_2 \xi - j\Lambda_2 \xi)\kappa r] \\
 & \left. \times \exp\left[-\frac{jL\kappa^2}{2k}(1 + \Theta_2 - \bar{\Theta}_2 \xi^2)\right]\right\} d\kappa d\xi.
 \end{aligned} \tag{106}$$

For a *retroreflector* target, Eq. (106) is replaced by

$$\begin{aligned}
 C_I^{iR}(\mathbf{r}, L) = & 8\pi^2 k^2 L \int_0^1 \int_0^\infty \kappa \Phi_n(\kappa) \exp\left[-\frac{\Lambda_2 L \kappa^2}{2k}(1 + \xi^2)\right] \\
 & \times \operatorname{Re}\left\{J_0[(1 + \Theta_2 - j\Lambda_2 - \bar{\Theta}_2 \xi + j\Lambda_2 \xi)\kappa r] \right. \\
 & \times \exp\left[-\frac{jL\kappa^2}{2k}(1 + \Theta_2 - 2\xi + \bar{\Theta}_2 \xi^2)\right] \\
 & - J_0[(1 + \Theta_2 - j\Lambda_2 - \bar{\Theta}_2 \xi - j\Lambda_2 \xi)\kappa r] \\
 & \left. \times \exp\left[-\frac{jL\kappa^2}{2k}(1 + \Theta_2 - \bar{\Theta}_2 \xi^2)\right]\right\} d\kappa d\xi.
 \end{aligned} \tag{107}$$

Note that for $r = 0$ the correlation terms (106) and (107) are exactly the same. Consequently, only off-axis scintillations differ between the two types of reflectors. The total scintillation index on the optical axis of a reflected plane wave is shown in Fig. 13.14. Note that for large reflectors, inner scale values on the order of the Fresnel zone ($Q_I = 10$) lead to scintillation values roughly 28% greater than those predicted by the Kolmogorov spectrum. In Fig. 13.15 the scaled scintillation index is plotted as a function of $(kr^2/L)^{1/2}$ for various size reflectors and inner scale values. Except for small targets ($\Omega_R = 100$), the off-axis behavior is quite distinct for the two types of reflectors with the greatest scintillations associated with the plane mirror. The scintillation index on the optical axis and at the diffractive beam edge is shown in Fig. 13.16. Inner scale values are the same as in Fig. 13.15. Once again, the general behavior depicted here is similar to that in Fig. 13.13 for an incident spherical wave, but off-axis fluctuations for finite plane mirrors ($\Omega_R \sim 1$) are much greater for an incident plane wave than for a spherical wave.

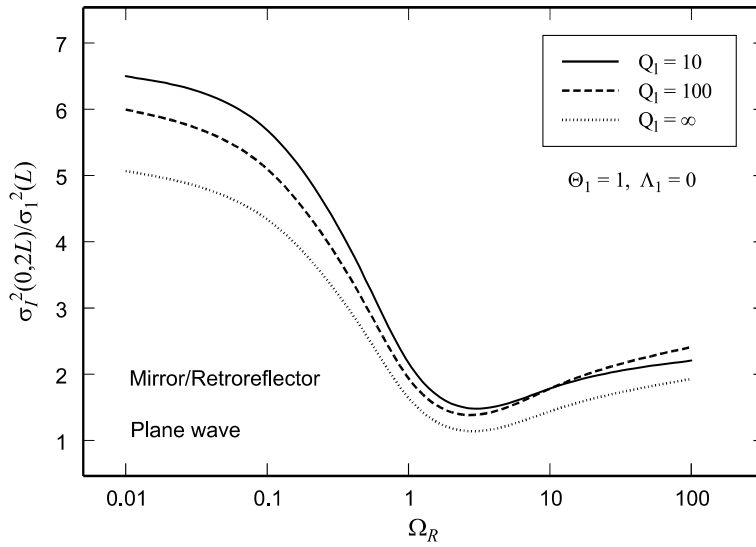


Figure 13.14 Same as Fig. 13.8 for an incident plane wave.

13.6 Finite Smooth Reflector—Part III

In addition to the BSAE associated with the mean irradiance, an effect also exists concerning the coherence properties of the received optical wave caused by double passage of the wave through the same inhomogeneities of the random medium. For

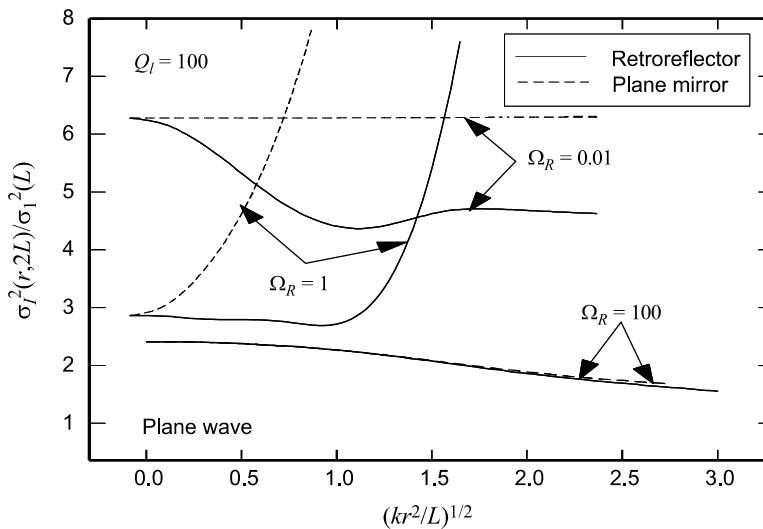


Figure 13.15 Same as Fig. 13.9 for an incident plane wave.

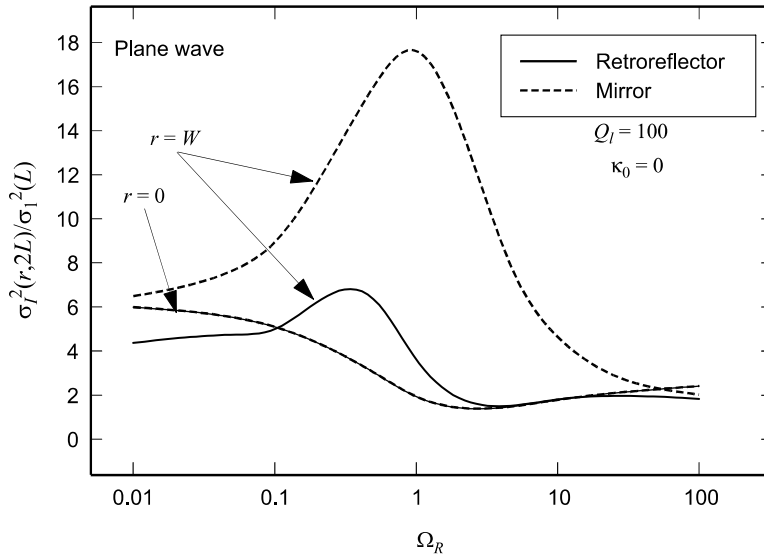


Figure 13.16 Same as Fig. 13.10 for an incident plane wave.

finite smooth reflecters, this effect appears as either an increase or decrease in the spatial coherence radius of the double-passage wave as compared with the same wave in the absence of the mutual correlations between the incident and reflected waves.

13.6.1 Spatial coherence: incident beam wave

As in the case of line-of-sight propagation, the spatial coherence properties of a reflected wave are characterized by the *modulus of the complex degree of coherence*. In the weak fluctuation regime, this function is defined by [14]

$$\text{DOC}(\mathbf{r}_1, \mathbf{r}_2, 2L) = \frac{|\Gamma_2(\mathbf{r}_1, \mathbf{r}_2, 2L)|}{\sqrt{\Gamma_2(\mathbf{r}_1, \mathbf{r}_1, 2L)\Gamma_2(\mathbf{r}_2, \mathbf{r}_2, 2L)}} \quad (108)$$

or, on simplifying,

$$\text{DOC}(\mathbf{r}_1, \mathbf{r}_2, 2L) = \exp\left[-\frac{1}{2}D(\mathbf{r}_1, \mathbf{r}_2, 2L)\right], \quad (109)$$

where $D(\mathbf{r}_1, \mathbf{r}_2, 2L)$ is the WSF associated with the double-passage wave. It has been shown that the WSF can be expressed as the sum

$$D(\mathbf{p}, \mathbf{r}, 2L) = \text{Re}[\Delta^i(\mathbf{p}, \mathbf{r}, L) + \Delta^R(\mathbf{p}, \mathbf{r}, L) + \Delta^{iR}(\mathbf{p}, \mathbf{r}, L)], \quad (110)$$

where

$$\begin{aligned} \Delta^i(\mathbf{p}, \mathbf{r}, L) = & 4\pi^2 k^2 L \int_0^1 \int_0^\infty \kappa \Phi_n(\kappa) \left\{ J_0[(\gamma_a^i - \gamma_a^{i*})\kappa r_1] + J_0[(\gamma_a^i - \gamma_a^{i*})\kappa r_2] \right. \\ & \left. - 2J_0[|(\gamma_a^i + \gamma_a^{i*})\mathbf{p}/2 + (\gamma_a^i - \gamma_a^{i*})\mathbf{r}|\kappa] \right\} \\ & \times \exp \left\{ -\frac{j\kappa^2}{2k} [\gamma_a^i B_a^i(\xi) - \gamma_a^{i*} B_a^{i*}(\xi)] \right\} d\kappa d\xi, \end{aligned} \quad (111)$$

$$\begin{aligned} \Delta^R(\mathbf{p}, \mathbf{r}, L) = & 4\pi^2 k^2 L \int_0^1 \int_0^\infty \kappa \Phi_n(\kappa) \left\{ J_0[(\gamma_a^R - \gamma_a^{R*})\kappa r_1] + J_0[(\gamma_a^R - \gamma_a^{R*})\kappa r_2] \right. \\ & \left. - 2J_0[|(\gamma_a^R + \gamma_a^{R*})\mathbf{p}/2 + (\gamma_a^R - \gamma_a^{R*})\mathbf{r}|\kappa] \right\} \\ & \times \exp \left[-\frac{j\kappa^2}{2k} (\gamma_a^R - \gamma_a^{R*}) B_a^R(\xi) \right] d\kappa d\xi, \end{aligned} \quad (112)$$

$$\begin{aligned} \Delta^{iR}(\mathbf{p}, \mathbf{r}, L) = & 4\pi^2 k^2 L \int_0^1 \int_0^\infty \kappa \Phi_n(\kappa) \left\{ J_0[(\gamma_a^i \mp \gamma_a^{R*})\kappa r_1] + J_0[(\gamma_a^i \mp \gamma_a^{R*})\kappa r_2] \right. \\ & \left. - 2J_0[|(\gamma_a^i + \gamma_a^{R*})\mathbf{p}/2 + (\gamma_a^i \mp \gamma_a^{R*})\mathbf{r}|\kappa] \right\} \\ & \times \exp \left\{ -\frac{j\kappa^2}{2k} [\gamma_a^i B_a^i(\xi) - \gamma_a^{R*} B_a^{R*}(\xi)] \right\} d\kappa d\xi \\ & + 4\pi^2 k^2 L \int_0^1 \int_0^\infty \kappa \Phi_n(\kappa) \left\{ J_0[(\gamma_a^R \mp \gamma_a^{i*})\kappa r_1] + J_0[(\gamma_a^R \mp \gamma_a^{i*})\kappa r_2] \right. \\ & \left. - 2J_0[|(\gamma_a^R \pm \gamma_a^{i*})\mathbf{p}/2 + (\gamma_a^R \mp \gamma_a^{i*})\mathbf{r}|\kappa] \right\} \\ & \times \exp \left\{ -\frac{j\kappa^2}{2k} [\gamma_a^R B_a^R(\xi) - \gamma_a^{i*} B_a^{i*}(\xi)] \right\} d\kappa d\xi. \end{aligned} \quad (113)$$

Equations (111) and (112) are valid for both types of reflectors, but not (113). In particular, the upper signs in Eq. (113) are associated with a plane mirror target and the lower signs are associated with a retroreflector target. Also, we are using the notation $r_1 = |\mathbf{r} + \mathbf{p}/2|$ and $r_2 = |\mathbf{r} - \mathbf{p}/2|$. Notice that the WSF and, hence, the modulus of the complex degree of coherence are independent of the reciprocal path terms that contributed to the BSAE of the mean irradiance (see Prob. 10).

13.6.2 Spatial coherence: incident spherical wave

The WSF generally depends not only on the separation distance $\rho = |\mathbf{r}_1 - \mathbf{r}_2|$, but also on the location of the two observation points \mathbf{r}_1 and \mathbf{r}_2 in the receiver plane. However, when the observation points are symmetrically located with respect to the optical axis, i.e., when $\mathbf{r}_2 = -\mathbf{r}_1$, or $r = 0$, the WSF depends only on ρ . Further simplifications in the WSF also occur for the case of a *spherical wave* (point

source) at the transmitter, characterized by $\Theta_1 = \Lambda_1 = 0$. By invoking both of these simplifying assumptions, it readily follows that the WSF can be expressed as

$$\begin{aligned} D(\mathbf{r}_1, -\mathbf{r}_1, 2L) &\equiv D(\rho, 2L) \\ &= \Delta^i(\rho, L) + \Delta^R(\rho, L) \pm \operatorname{Re}[\Delta^{iR}(\rho, L)], \end{aligned} \quad (114)$$

where

$$\Delta^i(\rho, L) = 8\pi^2 k^2 L \int_0^1 \int_0^\infty \kappa \Phi_n(\kappa) \exp\left(-\frac{\Lambda_2 L \kappa^2 \xi^2}{k}\right) [I_0(\Lambda_2 \kappa \xi \rho) - J_0(\Theta_2 \kappa \xi \rho)] d\kappa d\xi, \quad (115)$$

$$\begin{aligned} \Delta^R(\rho, L) &= 8\pi^2 k^2 L \int_0^1 \int_0^\infty \kappa \Phi_n(\kappa) \exp\left(-\frac{\Lambda_2 L \kappa^2 \xi^2}{k}\right) \\ &\quad \times \{I_0(\Lambda_2 \kappa \xi \rho) - J_0[(1 - \bar{\Theta}_2 \xi) \kappa \rho]\} d\kappa d\xi, \end{aligned} \quad (116)$$

$$\begin{aligned} \Delta^{iR}(\rho, L) &= 8\pi^2 k^2 L \int_0^1 \int_0^\infty \kappa \Phi_n(\kappa) \exp\left(-\frac{\Lambda_2 L \kappa^2 \xi^2}{k}\right) \{J_0[(1 - \xi + 2j\Lambda_2 \xi) \kappa \rho / 2] \\ &\quad + J_0[(1 - \xi - 2j\Lambda_2 \xi) \kappa \rho / 2] - 2J_0[(1 - \xi + 2\Theta_2 \xi) \kappa \rho / 2]\} d\kappa d\xi. \end{aligned} \quad (117)$$

Within the inertial subrange, Eqs. (115)–(117) lead to

$$\begin{aligned} D(\rho, 2L) &= \Delta^i(\rho, L) + \Delta^R(\rho, L) \pm \operatorname{Re}[\Delta^{iR}(\rho, L)] \\ &\cong 1.09 C_n^2 k^{7/6} L^{11/6} \left\{ \left[|\Theta_2|^{5/3} + a_2 \pm \left(\frac{1}{2}\right)^{5/3} (a_3 - a_4) \right] \left(\frac{k\rho^2}{L}\right)^{5/6} \right. \\ &\quad \left. + 1.24 \Lambda_2^{11/6} \left(\frac{k\rho^2}{L}\right) \right\}, \quad l_0 \ll \rho \ll L_0, \end{aligned} \quad (118)$$

where the upper sign is used with a plane mirror target and the lower sign with a retroreflector. Also, the parameters a_m , $m = 2, 3$, and 4 are defined by

$$a_2 = \begin{cases} \frac{1 - \Theta_2^{8/3}}{1 - \Theta_2}, & \Theta_2 \geq 0, \\ \frac{1 + |\Theta_2|^{8/3}}{1 - \Theta_2}, & \Theta_2 < 0, \end{cases} \quad (119)$$

$$a_3 = \begin{cases} \frac{1 - (2\Theta_2)^{8/3}}{1 - 2\Theta_2}, & \Theta_2 \geq 0, \\ \frac{1 + |2\Theta_2|^{8/3}}{1 - 2\Theta_2}, & \Theta_2 < 0, \end{cases} \quad (120)$$

$$a_4 = \frac{1}{1 + 4\Lambda_2^2} - \frac{(2\Lambda_2)^{8/3}}{(1 + 4\Lambda_2^2)^{1/2}} \cos\left[\tan^{-1}(2\Lambda_2) + \frac{4\pi}{3}\right]. \quad (121)$$

For separation distances less than the inner scale, the WSF based on the Tatarskii spectrum [Eq. (19) in Chap. 3] can be approximated by

$$D(\rho, 2L) = \begin{cases} 1.09C_n^2k^2Ll_0^{-1/3}\rho^2(1 + 2\Theta_2 + 4\Theta_2^2 + 4\Lambda_2^2), \rho \ll l_0, (\text{plane mirror}), \\ 1.09C_n^2k^2Ll_0^{-1/3}\rho^2, \rho \ll l_0, (\text{retroreflector}). \end{cases} \quad (122)$$

Note that in the case of a retroreflector, the WSF (122) is that associated with the reflected spherical wave (Section 6.4.2). The same is true of a plane mirror only in the case of a sufficiently small (point) target ($\Theta_2 = \Lambda_2 = 0$).

The implied *spatial coherence radius* ρ_0 associated with the backscattered wave is defined by the $1/e$ point of the modulus of the complex degree of coherence (108). Thus, the implied coherence radius ρ_0 obtained from (118) can be approximated by [14]

$$\frac{\rho_0}{\rho_{pl}} \cong 1.80 \left[|\Theta_2|^{5/3} + a_2 \pm \left(\frac{1}{2} \right)^{5/3} (a_3 - a_4) + 1.24\Lambda_2^{11/6} \right]^{-3/5}, l_0 \ll \rho_0 \ll L_0, \quad (123)$$

where $\rho_{pl} = (1.46C_n^2k^2L)^{-3/5}$ is the plane wave coherence radius over a path of length L (Section 6.4.1). In Fig. 13.17 the solid curve represents the coherence

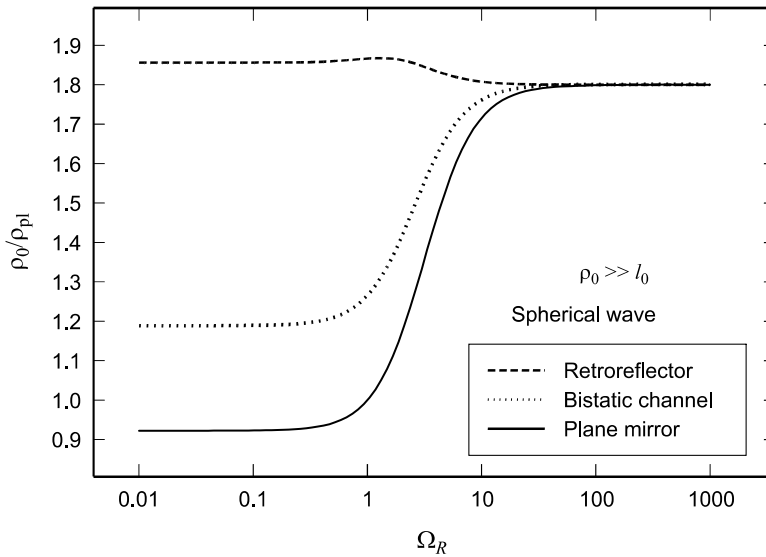


Figure 13.17 The transverse spatial coherence radius at the receiver of a reflected spherical wave scaled by the plane wave coherence radius and plotted as a function of reflector size.

ratio predicted by (123) for a plane mirror as a function of reflector size Ω_R . The dashed curve corresponds to the coherence ratio for a retroreflector and the dotted curve (bistatic case) represents the reflected wave in the absence of mutual correlations between the incident and reflected waves. Except for very small reflectors, the coherence radius for a retroreflected wave is always significantly greater than that for a plane mirror reflector. Inner scale effects (not shown) generally play a small role in the spatial coherence radius except for cases in which the inner scale and coherence radius are of comparable size. In this latter case, inner scale effects can lead to significantly different results.

13.7 Unresolved (Point) Target

When the transverse dimension of the target is significantly smaller than the size of the first Fresnel zone (i.e., far-field diffraction-dominated so that $\Omega_R \gg 1$), it is considered an *unresolved small target*, also commonly called a “point target.” In this case, the echo wave is essentially a spherical wave with the target acting like a pseudo point source, i.e., we find from Eqs. (15) that $\Theta_2 = \Lambda_2 \Rightarrow 0$.

We begin by examining the factors $P(\mathbf{r}_1, \mathbf{r}_2)$ and $N(\mathbf{r}_1, \mathbf{r}_2)$ that appear in the MCF and are defined for a smooth reflector by Eqs. (45), (46), and (47). For a point target, Eq. (45) leads to

$$P(\mathbf{r}_1, \mathbf{r}_2) = \exp\left[-T_i - \frac{1}{2}D_{\text{sp}}(\rho, L)\right], \quad (124)$$

where

$$T_i = 4\pi^2 k^2 L \int_0^1 \int_0^\infty \kappa \Phi_n(\kappa) \left[1 - \exp\left(-\frac{\Lambda_1 L \kappa^2 \xi^2}{k}\right)\right] d\kappa d\xi, \quad (125)$$

$$D_{\text{sp}}(\rho, L) = 8\pi^2 k^2 L \int_0^1 \int_0^\infty \kappa \Phi_n(\kappa) [1 - J_0(\kappa \xi \rho)] d\kappa d\xi. \quad (126)$$

The quantity (125) appearing in the form $\exp(-T_i) \cong 1/(1 + T_i)$ describes the decrease in the on-axis mean irradiance associated with the incident beam wave, and (126) is the spherical wave structure function (WSF) associated with the reflected wave. The second factor $N(\mathbf{r}_1, \mathbf{r}_2)$ defines the two-point BSAE, which once again we write as

$$N(\mathbf{r}_1, \mathbf{r}_2) = \exp[B_{\Gamma}^{iR}(\mathbf{r}_1, \mathbf{r}_2, L)], \quad (127)$$

where the two-point correlation function for a point target is

$$\begin{aligned}
 B_{\Gamma}^{iR}(\mathbf{p}, \mathbf{r}, L) = & 4\pi^2 k^2 L \int_0^1 \int_0^\infty \kappa \Phi_n(\kappa) \exp\left(-\frac{\Lambda_1 L \kappa^2 \xi^2}{2k}\right) \\
 & \times \left[J_0(|\mathbf{r} + \mathbf{p}/2| \kappa \xi) \exp\left(\frac{j\Theta_1 L \kappa^2 \xi^2}{2k}\right) \right. \\
 & \left. + J_0(|\mathbf{r} - \mathbf{p}/2| \kappa \xi) \exp\left(-\frac{j\Theta_1 L \kappa^2 \xi^2}{2k}\right) \right] d\kappa d\xi \\
 & - 4\pi^2 k^2 L \int_0^1 \int_0^\infty \kappa \Phi_n(\kappa) \exp\left(-\frac{\Lambda_1 L \kappa^2 \xi^2}{2k}\right) \\
 & \times \left\{ J_0(|\mathbf{r} + \mathbf{p}/2| \kappa \xi) \exp\left[-\frac{jL\kappa^2}{2k} \xi(2 - 2\xi + \Theta_1 \xi)\right] \right. \\
 & \left. + J_0(|\mathbf{r} - \mathbf{p}/2| \kappa \xi) \exp\left[\frac{jL\kappa^2}{2k} \xi(2 - 2\xi + \Theta_1 \xi)\right] \right\} d\kappa d\xi.
 \end{aligned} \tag{128}$$

Both (124) and (128) reduce to simpler expressions when the illumination wave is a *spherical wave* ($\Theta_1 = \Lambda_1 = 0$). Under this assumption, we find that

$$\begin{aligned}
 P(\mathbf{r}_1, \mathbf{r}_2) = & \exp\left[-\frac{1}{2} D_{\text{sp}}(\rho, L)\right], \\
 B_{\Gamma}^{iR}(\mathbf{p}, \mathbf{r}, L) = & 4\pi^2 k^2 L \int_0^1 \int_0^\infty \kappa \Phi_n(\kappa) J_0(|\mathbf{r} + \mathbf{p}/2| \kappa \xi) \\
 & \times \left\{ 1 - \exp\left[-\frac{jL\kappa^2}{k} \xi(1 - \xi)\right] \right\} d\kappa d\xi \\
 & + 4\pi^2 k^2 L \int_0^1 \int_0^\infty \kappa \Phi_n(\kappa) J_0(|\mathbf{r} - \mathbf{p}/2| \kappa \xi) \\
 & \times \left\{ 1 - \exp\left[\frac{jL\kappa^2}{k} \xi(1 - \xi)\right] \right\} d\kappa d\xi.
 \end{aligned} \tag{130}$$

Note that, for $\mathbf{r}_2 = -\mathbf{r}_1$ in (130), it follows that $B_{\Gamma}^{iR}(\mathbf{p}, 0, L) = B_{I, \text{sp}}(\rho/2, L)$, which is the irradiance covariance function of a spherical wave propagating between the point target and receiver plane. When the illumination wave approaches the limiting case of an *unbounded plane wave* ($\Theta_1 = 1, \Lambda_1 = 0$), it can be readily

deduced that $P(\mathbf{r}_1, \mathbf{r}_2)$ is again defined by Eq. (129), but in this case the correlation function (128) is

$$\begin{aligned}
 B_{\Gamma}^{iR}(\mathbf{p}, \mathbf{r}, L) = & 4\pi^2 k^2 L \int_0^1 \int_0^\infty \kappa \Phi_n(\kappa) J_0(|\mathbf{r} + \mathbf{p}/2| \kappa \xi) \\
 & \times \left\{ \exp\left(\frac{jL\kappa^2 \xi^2}{2k}\right) - \exp\left[-\frac{jL\kappa^2}{2k} \xi(2 - \xi)\right] \right\} d\kappa d\xi \\
 & + 4\pi^2 k^2 L \int_0^1 \int_0^\infty \kappa \Phi_n(\kappa) J_0(|\mathbf{r} - \mathbf{p}/2| \kappa \xi) \\
 & \times \left\{ \exp\left(-\frac{jL\kappa^2 \xi^2}{2k}\right) - \exp\left[\frac{jL\kappa^2}{2k} \xi(2 - \xi)\right] \right\} d\kappa d\xi.
 \end{aligned} \tag{131}$$

13.7.1 Backscatter amplification factor: weak fluctuations

The BSAE is described in general by Eq. (58), and by setting $\mathbf{r}_1 = \mathbf{r}_2 = \mathbf{r}$ in Eq. (128), we find that we find that the resulting correlation function of a backscattered Gaussian-beam wave takes the form

$$\begin{aligned}
 B_{\Gamma}^{iR}(\mathbf{r}, L) = & 8\pi^2 k^2 L \int_0^1 \int_0^\infty \kappa \Phi_n(\kappa) J_0(\kappa \xi r) \exp\left(-\frac{\Lambda_1 L \kappa^2 \xi^2}{2k}\right) \\
 & \times \left\{ \cos\left(\frac{L\kappa^2 \xi^2 \Theta_1}{2k}\right) - \cos\left[\frac{L\kappa^2}{2k} \xi(2 - 2\xi + \Theta_1 \xi)\right] \right\} d\kappa d\xi.
 \end{aligned} \tag{132}$$

Using the Kolmogorov spectrum, Eq. (132) with $r = 0$ leads to the approximation

$$\begin{aligned}
 B_{\Gamma}^{iR}(0, L) \cong & 1.54\sigma_1^2(L) \left[(1 + \Theta_1)^2 + \Lambda_1^2 \right]^{5/12} \cos\left[\frac{5}{6} \tan^{-1}\left(\frac{1 + \Theta_1}{\Lambda_1}\right)\right] \\
 & - 1.49\sigma_1^2(L)(\Theta_1^2 + \Lambda_1^2)^{5/12} \cos\left[\frac{5}{6} \tan^{-1}\left(\frac{\Theta_1}{\Lambda_1}\right)\right].
 \end{aligned} \tag{133}$$

In Fig. 13.18 the scaled correlation function $B_{\Gamma}^{iR}(0, L)/\sigma_1^2(L)$, as predicted by the Kolmogorov spectrum and the modified atmospheric spectrum, is shown for a collimated beam ($\Theta_0 = 1$) as a function of the Fresnel ratio at the transmitter Λ_0 and various values of the inner scale parameter $Q_l = L\kappa_l^2/k = 10.89L/kl_0^2$. Outer scale effects are negligible in this case. Here we see that the combined effect of inner scale and high-wave-number bump can produce higher correlations between the incident and reflected waves than those predicted by the Kolmogorov spectrum (dotted curve).

13.7.2 Backscatter amplification factor: strong fluctuations

To extend the analysis into the regime of moderate-to-strong irradiance fluctuations, we build upon the ideas presented in Chap. 9 for the scintillation index.

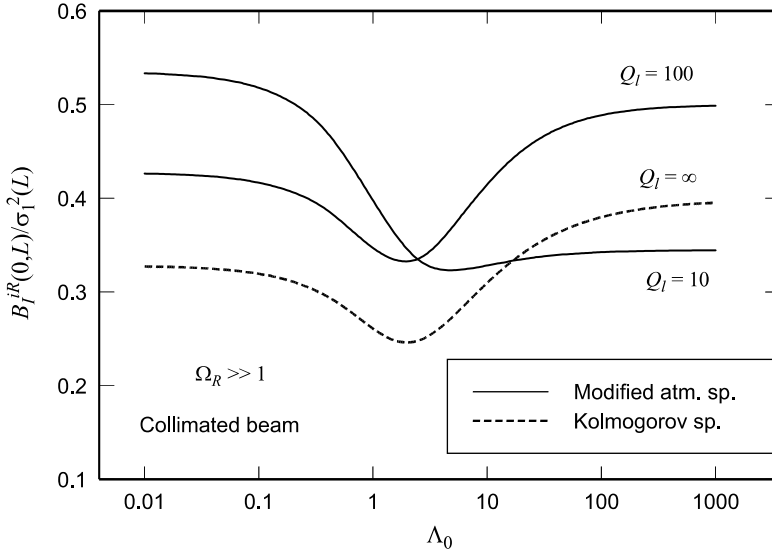


Figure 13.18 The scaled correlation function for a reflected collimated beam wave from a point reflector as a function of beam size $\Lambda_0 = 2L/kW_0^2$ and various values of the inner scale parameter $Q_l = 10.89L/kl_0^2$.

In particular, we represent the BSAE in the form

$$N(\mathbf{r}) = \exp[B_{\ln I}^{iR}(\mathbf{r}, L)] = \exp[B_{\ln X}^{iR}(\mathbf{r}, L) + B_{\ln Y}^{iR}(\mathbf{r}, L)], \quad (134)$$

where $B_{\ln I}^{iR}(\mathbf{r}, L)$ is the log-irradiance correlation function. Under weak irradiance fluctuations, it follows that

$$\begin{aligned} B_{\ln I}^{iR}(\mathbf{r}, L) &\cong B_I^{iR}(\mathbf{r}, L) \\ &= 8\pi^2 k^2 L \int_0^1 \int_0^\infty \kappa \Phi_n(\kappa) J_0(\kappa \xi r) \exp\left(-\frac{\Lambda_1 L \kappa^2 \xi^2}{2k}\right) \\ &\quad \times \left\{ \cos\left(\frac{L \kappa^2 \xi^2 \Theta_1}{2k}\right) - \cos\left[\frac{L \kappa^2}{2k} \xi(2 - 2\xi + \Theta_1 \xi)\right] \right\} d\kappa d\xi. \end{aligned} \quad (135)$$

The quantities $B_{\ln X}^{iR}(\mathbf{r}, L)$ and $B_{\ln Y}^{iR}(\mathbf{r}, L)$ in (134) are the large-scale and small-scale contributions to the log-irradiance correlation function. Because the correlation function (134) reduces to essentially zero at distances from the optical axis on the order of a Fresnel zone or less, we will present the following analysis only for the on-axis case ($r = 0$) and define [see Eq. (133)]

$$\begin{aligned} B_{\ln I}^{iR}(0, L) &\equiv \sigma_{B,C}^2 \cong 1.54 \sigma_1^2(L) [(1 + \Theta_1)^2 + \Lambda_1^2]^{5/12} \cos\left[\frac{5}{6} \tan^{-1}\left(\frac{1 + \Theta_1}{\Lambda_1}\right)\right] \\ &\quad - 1.49 \sigma_1^2(L) (\Theta_1^2 + \Lambda_1^2)^{5/12} \cos\left[\frac{5}{6} \tan^{-1}\left(\frac{\Theta_1}{\Lambda_1}\right)\right]. \end{aligned} \quad (136)$$

Examination of the ratio $\sigma_{B,C}^2/\sigma_1^2$ reveals that it decreases from 0.33 in the near field ($\Lambda_0 \ll 1$) to 0.26 when $\Lambda_0 \sim 1$, and then increases to 0.4 in the far field (see the dashed curve in Fig. 13.18). This behavior suggests that the on-axis correlation term (136) beyond the Rayleigh range ($\Lambda_0 > 1$) is roughly the same as that of the on-axis scintillation index associated with a Gaussian-beam wave (see Fig. 8.1 in Chap. 8). This observation is useful below in the development of the BSAE under moderate-to-strong irradiance fluctuations.

Let us first consider the small-scale log-irradiance variance $B_{\ln Y}^{iR}(0, L)$ defined by

$$B_{\ln Y}^{iR}(0, L) = 8\pi^2 k^2 L \int_0^1 \int_0^\infty \frac{\kappa^{14/3} \Phi_n(\kappa)}{(\kappa^2 + \kappa_Y^2)^{11/6}} \exp\left(-\frac{\Lambda_1 L \kappa^2 \xi^2}{2k}\right) \times \left\{ \cos\left(\frac{L \kappa^2 \xi^2 \Theta_1}{2k}\right) - \cos\left[\frac{L \kappa^2}{2k} \xi(2 - 2\xi + \Theta_1 \xi)\right] \right\} d\kappa d\xi. \quad (137)$$

Here, κ_Y is the cutoff spatial frequency that defines the largest small-scale inhomogeneity contributing to this component. Except for the limiting case of a transmitted spherical wave, we argue that each of the two cosine terms that appear under the integral in (137) contributes a negligibly small quantity to the small-scale effects under moderate-to-strong fluctuations. That is, the rapid fluctuations between positive and negative values of the cosine terms for large refractive wave numbers κ produce an average integral value of roughly zero. Thus, all small-scale effects associated with the correlation function in (134) begin to dissipate under moderate-to-strong irradiance fluctuations, leaving only large-scale effects that also eventually die out. Consequently, for modeling purposes we will group the small-scale effects that occur under weak fluctuations along with the large-scale effects into a single expression that reduces to only the large-scale effects under strong fluctuations.

In view of the above discussion, we assume the BSAE factor $N(0)$ can be written in the form

$$N(0) = \exp[B_{\ln I}^{iR}(0, L)] \cong \exp[B_{\ln X}^{iR}(0, L)]. \quad (138)$$

Under weak irradiance fluctuations, we let $B_{\ln X}^{iR}(0, L) \cong \sigma_{B,C}^2 (\sigma_1^2 \ll 1)$, where $\sigma_{B,C}^2$ is given by Eq. (136). Thus, by relying on the formulation for the large-scale log-irradiance variance given in Chap. 9, we can approximate the enhancement factor (138) under moderate-to-strong irradiance fluctuations in the absence of inner scale and/or outer scale effects by

$$N(0) = \langle C(0) \rangle = \exp\left[\frac{\sigma_{B,C}^2}{\left(1 + 0.58\sigma_{B,C}^{12/5}\right)^{7/6}}\right]. \quad (139)$$

In Fig. 13.19 we illustrate the BSAE $N(0)$ described by Eq. (139) for the case when the target is illuminated by a collimated beam. Here we see that the enhancement factor increases from unity to above 2 near the peak values and then decreases back toward unity as the optical wave approaches the saturation

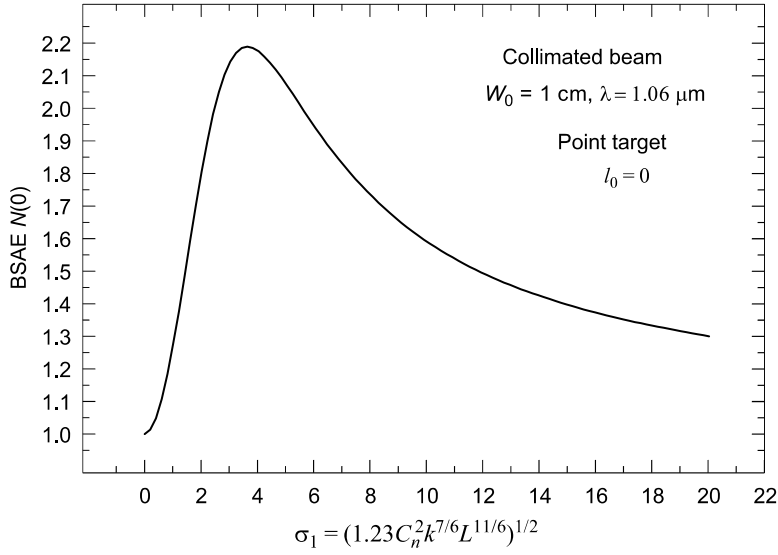


Figure 13.19 Enhancement factor $N(0)$ described by Eq. (139) as a function of the root-mean-square Rytov variance for a transmitted collimated beam wave. Inner scale and outer scale effects have been ignored.

regime. This behavior for weak fluctuations and the saturation regime is depicted by the asymptotic relations

$$N(0) \cong \begin{cases} 1 + \sigma_{B,C}^2, & \sigma_1^2 \ll 1 \\ 1 + \frac{1.89}{\sigma_{B,C}^{4/5}}, & \sigma_1^2 \gg 1, \Lambda_0 < \infty. \end{cases} \quad (140)$$

We have imposed the condition $\Lambda_0 < \infty$ to exclude the limiting case of a spherical wave. That is, the comparable model developed for the case when the illumination beam is a spherical wave leads to results distinct from (139) and (140) that cannot be deduced from these expressions [17].

When we cannot ignore inner scale and outer scale effects, the expression for $B_{\ln X}^{ie}(0, L)$ in Eq. (138) can be approximated beyond the Rayleigh range (and in the far field) by that for a standard Gaussian-beam wave, viz.,

$$B_{\ln X}^{iR}(0, L) = B_{\ln X}^{iR}(l_0) - B_{\ln X}^{iR}(L_0), \quad 1 < \Lambda_0 < \infty, \quad (141)$$

where, under the condition $1 < \Lambda_0 < \infty$, we use the approximations (see Chap. 9)

$$B_{\ln X}^{iR}(l_0) \cong \sigma_1^2(L) \left(\frac{1}{3} - \frac{1}{2} \bar{\Theta}_1 + \frac{1}{5} \bar{\Theta}_1^2 \right) \left(\frac{\eta_{CX} Q_l}{\eta_{CX} + Q_l} \right)^{7/6} \\ \times \left[1 + 1.75 \left(\frac{\eta_{CX}}{\eta_{CX} + Q_l} \right)^{1/2} - 0.25 \left(\frac{\eta_{CX}}{\eta_{CX} + Q_l} \right)^{7/12} \right], \quad (142)$$

$$B_{\ln X}^{iR}(L_0) \cong \sigma_1^2(L) \left(\frac{1}{3} - \frac{1}{2} \bar{\Theta}_1 + \frac{1}{5} \bar{\Theta}_1^2 \right) \left(\frac{\eta_{CX0} Q_l}{\eta_{CX0} + Q_l} \right)^{7/6} \\ \times \left[1 + 1.75 \left(\frac{\eta_{CX0}}{\eta_{CX0} + Q_l} \right)^{1/2} - 0.25 \left(\frac{\eta_{CX0}}{\eta_{CX0} + Q_l} \right)^{7/12} \right]. \quad (143)$$

Here, we have defined

$$\frac{1}{\eta_{CX}} = \frac{0.38}{1 - 3.21 \bar{\Theta}_1 + 5.29 \bar{\Theta}_1^2} + 0.94 \sigma_1^2 Q_l^{1/6} \left(\frac{\frac{1}{3} - \frac{1}{2} \bar{\Theta}_1 + \frac{1}{5} \bar{\Theta}_1^2}{1 + 2.20 \bar{\Theta}_1} \right)^{6/7}, \quad (144)$$

$$\eta_{CX0} = \frac{\eta_{CX} Q_0}{\eta_{CX} + Q_0}, \quad (145)$$

and $Q_0 = 64\pi^2 L / k L_0^2$, where L_0 is the outer scale.

13.7.3 Spatial coherence

In Section 13.6 we derived Eqs. (111)–(113) for calculating the WSF associated with an incident beam wave on a finite smooth target. If we now consider the limiting case of an unresolved (point) target, we have $\Theta_2 = \Lambda_2 = 0$ and, consequently, $\Theta = \Lambda = 0$. Therefore, these expressions reduce to

$$\Delta^i(\mathbf{p}, \mathbf{r}, L) \equiv 0, \\ \Delta^R(\mathbf{p}, \mathbf{r}, L) = 8\pi^2 k^2 L \int_0^1 \int_0^\infty \kappa \Phi_n(\kappa) [1 - J_0(\kappa \xi \rho)] d\kappa d\xi \\ = D_{\text{sp}}(\rho, L), \\ \text{Re}[\Delta^{iR}(\mathbf{p}, \mathbf{r}, L) \equiv 0. \quad (146)$$

The WSF (110) for a point target is, therefore, simply $D(\mathbf{p}, \mathbf{r}, 2L) = D_{\text{sp}}(\rho, L)$. As a consequence, it follows that the spatial coherence radius of a reflected Gaussian-beam wave for both bistatic and monostatic systems is the same as that for a spherical wave propagating over a path of length L from the unresolved target to the receiver.

13.7.4 Covariance and scintillation index: weak fluctuations

For a *Gaussian beam* incident on a point target, the log-amplitude covariance function described by Eq. (86) reduces to

$$B_X(\mathbf{p}, \mathbf{r}, 2L) = \sigma_{X, \text{beam}}^2(0, L) + B_{X, \text{sp}}(\rho, L) + 2C_X^{iR}(\mathbf{p}, \mathbf{r}, L), \quad (147)$$

where

$$\sigma_{\chi, \text{beam}}^2(0, L) = 4\pi^2 k^2 L \int_0^1 \int_0^\infty \kappa \Phi_n(\kappa) \exp\left(-\frac{\Lambda_1 L \kappa^2 \xi^2}{k}\right) \sin^2\left[\frac{L \kappa^2}{2k} \xi(1 - \bar{\Theta}_1 \xi)\right] d\kappa d\xi \quad (148)$$

is the longitudinal component of the log-amplitude variance of the incident Gaussian-beam wave, $B_{\chi, \text{sp}}(\rho, L)$ is the spherical wave log-amplitude covariance function of the reflected wave, and $C_{\chi}^{iR}(\mathbf{p}, \mathbf{r}, L)$ is the mutual intensity correlation between incident and reflected waves described by

$$\begin{aligned} C_{\chi}^{iR}(\mathbf{p}, \mathbf{r}, L) &= \pi^2 k^2 L \int_0^1 \int_0^\infty \kappa \Phi_n(\kappa) \exp\left(-\frac{\Lambda_1 L \kappa^2 \xi^2}{2k}\right) \\ &\quad \times [J_0(|\mathbf{r} + \mathbf{p}/2| \kappa \xi) + J_0(|\mathbf{r} - \mathbf{p}/2| \kappa \xi)] \\ &\quad \times \left\{ \cos\left(\frac{L \kappa^2 \xi^2 \Theta_1}{2k}\right) - \cos\left[\frac{L \kappa^2}{2k} \xi(2 - 2\xi + \Theta_1 \xi)\right] \right\} d\kappa d\xi. \end{aligned} \quad (149)$$

In general, the correlation function (149) depends on the location of the two points within the beam spot size. However, when $\mathbf{r}_2 = -\mathbf{r}_1$, Eq. (149) becomes a function of separation distance alone given by

$$\begin{aligned} C_{\chi}^{iR}(\rho, L) &= 2\pi^2 k^2 L \int_0^1 \int_0^\infty \kappa \Phi_n(\kappa) J_0(\rho \kappa \xi/2) \exp\left(-\frac{\Lambda_1 L \kappa^2 \xi^2}{2k}\right) \\ &\quad \times \left\{ \cos\left(\frac{L \kappa^2 \xi^2 \Theta_1}{2k}\right) - \cos\left[\frac{L \kappa^2}{2k} \xi(2 - 2\xi + \Theta_1 \xi)\right] \right\} d\kappa d\xi. \end{aligned} \quad (150)$$

In this case, the normalized covariance function of irradiance (90) can be expressed as

$$b_I(\rho, 2L) = b_{\chi}(\rho, 2L) = \frac{\sigma_{\chi, \text{beam}}^2(0, L) + B_{\chi, \text{sp}}(\rho, L) + 2C_{\chi}^{iR}(\rho, L)}{\sigma_{\chi, \text{beam}}^2(0, L) + \sigma_{\chi, \text{sp}}^2(L) + 2C_{\chi}^{iR}(\rho, L)}, \quad (151)$$

where $\sigma_{\chi, \text{sp}}^2(L)$ is the log-amplitude variance of a spherical wave. In the limit $\rho \rightarrow \infty$, the normalized covariance function (151) reduces not to zero but to the residual value

$$b_I(\rho, 2L) = \frac{\sigma_{\chi, \text{beam}}^2(0, L)}{\sigma_{\chi, \text{beam}}^2(0, L) + \sigma_{\chi, \text{sp}}^2(L)}, \quad \rho \rightarrow \infty. \quad (152)$$

Belen'kii [22] has discussed how the residual scintillation effect (152) can be used to advantage in remote sensing techniques.

For the special case of a point target, the *scintillation index* (93) developed for a finite smooth target with $\Theta_2 = \Lambda_2 = 0$ reduces (approximately) to

$$\sigma_I^2(\mathbf{r}, 2L) = 4B_{\chi}(0, \mathbf{r}, 2L) = \sigma_{I, \text{beam}}^2(0, L) + \sigma_{I, \text{sp}}^2(L) + 2C_I^{iR}(\mathbf{r}, L), \quad \Omega_R \gg 1. \quad (153)$$

Here, $\sigma_{I,\text{beam}}^2(0, L)$ is the same as the longitudinal (or on-axis) component of scintillation of the incident Gaussian-beam wave defined by

$$\sigma_{I,\text{beam}}^2(0, L) = 8\pi^2 k^2 L \int_0^1 \int_0^\infty \kappa \Phi_n(\kappa) \exp\left(-\frac{\Lambda_1 L \kappa^2 \xi^2}{k}\right) \times \left\{ 1 - \cos\left[\frac{L \kappa^2}{k} \xi(1 - \overline{\Theta}_1 \xi)\right] \right\} d\kappa d\xi. \quad (154)$$

Note that the radial dependency in this term for the reflected wave has vanished because of the particular nature of the target. The term $\sigma_{I,\text{sp}}^2(L)$ is the same as the scintillation index of a spherical wave propagating from the target to the receiver and defined by Eq. (154) with $\Lambda_1 = 0$ and $\overline{\Theta}_1 = 1$. The last term $C_I^{iR}(\mathbf{r}, L)$ is the correlation function between incident and reflected waves defined by

$$C_I^{iR}(\mathbf{r}, L) = 8\pi^2 k^2 L \int_0^1 \int_0^\infty \kappa \Phi_n(\kappa) J_0(r \kappa \xi) \exp\left(-\frac{\Lambda_1 L \kappa^2 \xi^2}{2k}\right) \times \left\{ \cos\left(\frac{L \kappa^2 \xi^2 \Theta_1}{2k}\right) - \cos\left[\frac{L \kappa^2}{2k} \xi(2 - 2\xi + \Theta_1 \xi)\right] \right\} d\kappa d\xi. \quad (155)$$

Maximum fluctuations described by (153) occur in the strictly backward direction ($r = 0$). Moreover, the correlation function (155) tends to zero at all off-axis points satisfying $r \gg \sqrt{L/k}$, effectively reducing the scintillation index (153) to a constant level. This means that for a receiver with a large collecting aperture a residual turbulent scintillation effect will occur rather than the standard aperture-averaging effect (Chap. 10) associated with one-way propagation systems.

Assuming a Kolmogorov spectrum, Eq. (154) leads to [recall Eq. (19) in Chap. 8]

$$\begin{aligned} \sigma_{I,\text{beam}}^2(0, L) &= 3.86\sigma_1^2(L) \text{Re} \left[j^{5/6} {}_2F_1\left(-\frac{5}{6}, \frac{11}{6}; \frac{17}{6}; \overline{\Theta}_1 + j\Lambda_1\right) - \frac{11}{16} \Lambda_1^{5/6} \right] \\ &\cong 3.86\sigma_1^2(L) \left\{ 0.4[(1 + 2\overline{\Theta}_1)^2 + 4\Lambda_1^2]^{5/12} \right. \\ &\quad \times \cos\left[\frac{5}{6} \tan^{-1}\left(\frac{1 + 2\overline{\Theta}_1}{2\Lambda_1}\right)\right] - \frac{11}{16} \Lambda_1^{5/6} \left. \right\}, \end{aligned} \quad (156)$$

where we have introduced an accurate approximation in the second line. Also, we have $\sigma_{I,\text{sp}}^2(L) = 0.4\sigma_1^2(L)$ and Eq. (155) with $r = 0$ leads to a similar approximation

$$\begin{aligned} C_I^{iR}(0, L) &\cong 1.54\sigma_1^2(L) [(1 + \overline{\Theta}_1)^2 + \Lambda_1^2]^{5/12} \cos\left[\frac{5}{6} \tan^{-1}\left(\frac{1 + \overline{\Theta}_1}{\Lambda_1}\right)\right] \\ &\quad - 1.49\sigma_1^2(L) (\overline{\Theta}_1^2 + \Lambda_1^2)^{5/12} \cos\left[\frac{5}{6} \tan^{-1}\left(\frac{\overline{\Theta}_1}{\Lambda_1}\right)\right]. \end{aligned} \quad (157)$$

The on-axis irradiance variance (153) for a reflected collimated beam ($\Theta_0 = 1$) yields the limiting results

$$\sigma_I^2(0, 2L) = \begin{cases} 1.6\sigma_1^2(L), & \Lambda_0 \gg 1 \\ 2.06\sigma_1^2(L), & \Lambda_0 \ll 1, \end{cases} \quad (158)$$

both based on a Kolmogorov spectrum. For off-axis points such that $r \gg \sqrt{L/k}$, the corresponding results are

$$\sigma_I^2(r, 2L) = \begin{cases} 0.8\sigma_1^2(L), & \Lambda_0 \gg 1, r \gg \sqrt{L/k} \\ 1.4\sigma_1^2(L), & \Lambda_0 \ll 1, r \gg \sqrt{L/k}. \end{cases} \quad (159)$$

In Fig. 13.20 we plot the scintillation index (153) scaled by the Rytov variance for an unresolved target illuminated by a collimated beam. Results are based on the Kolmogorov spectrum and plotted as a function of Fresnel ratio $\Lambda_0 = 2L/kW_0^2$ to illustrate the effect of transmitter beam size. Clearly, on-axis (solid curve) scintillation dominates that at points off axis (dashed curve) for $r \gg \sqrt{L/k}$ owing to the irradiance correlation function $C_I^R(\mathbf{r}, L)$ that attains its maximum on the optical axis (monostatic configuration) and decreases to zero when $r \gg \sqrt{L/k}$ (bistatic configuration).

13.7.5 Scintillation index: strong fluctuations

To extend the analysis of the previous section into the moderate-to-strong irradiance fluctuation regime, we start with a *bistatic channel* in which the scintillation index (153) under weak irradiance fluctuations takes the form

$$\sigma_I^2(\mathbf{r}, 2L)_{\text{bistatic}} \equiv \sigma_I^2(2L)_{\text{bistatic}} = \sigma_{\ln I, \text{beam}}^2(0, L) + \sigma_{\ln I, \text{sp}}^2(L), \quad \Omega_R \gg 1. \quad (160)$$

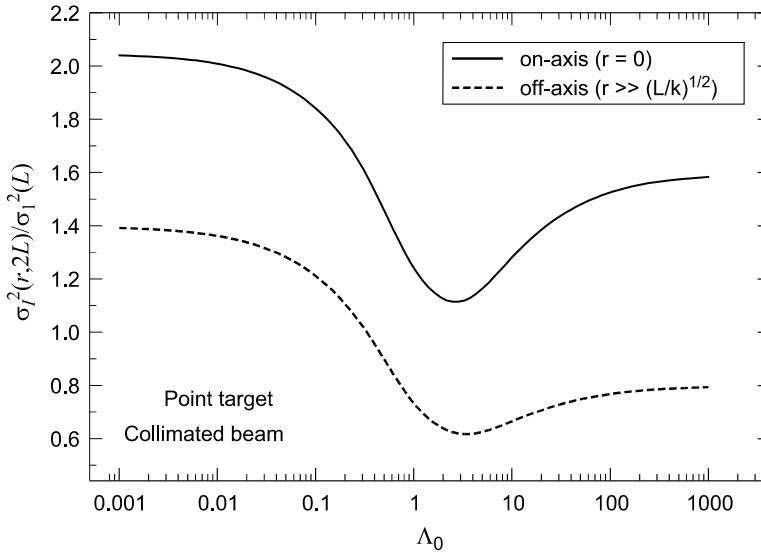


Figure 13.20 Scintillation index of a reflected collimated beam from an unresolved (point) target. Results are based on a Kolmogorov power-law spectrum.

Because in this case there is no radial dependency in either term on the right, we have written the total scintillation index as a function of only propagation distance $2L$. Also, we have expressed the quantities on the right in terms of log-irradiance fluctuations in accordance with the notation presented in Chap. 9. By following the general technique outlined in Chap. 9, we assume the scintillation index under all irradiance fluctuation conditions takes the form [17]

$$\sigma_I^2(2L)_{\text{bistatic}} = \exp[\sigma_{\ln X}^2(2L) + \sigma_{\ln Y}^2(2L)] - 1, \quad (161)$$

where the large- and small-scale components can be further expressed as

$$\begin{aligned} \sigma_{\ln X}^2(2L) &= \sigma_{\ln X, \text{beam}}^2(L) + \sigma_{\ln X, \text{sp}}^2(L), \\ \sigma_{\ln Y}^2(2L) &= \sigma_{\ln Y, \text{beam}}^2(L) + \sigma_{\ln Y, \text{sp}}^2(L). \end{aligned} \quad (162)$$

Now that we have identified each term on the right in (162) as a beam or spherical wave quantity, we can simply use the large- and small-scale expressions developed in Chap. 9 for the beam wave and spherical wave components. Under the assumption of a Kolmogorov spectrum, this leads to the specific form

$$\begin{aligned} \sigma_I^2(2L)_{\text{bistatic}} &= \exp \left[\frac{0.49\sigma_B^2}{\left[1 + 0.56(1 + \Theta_1)\sigma_B^{12/5}\right]^{7/6}} + \frac{0.49\beta_0^2}{\left(1 + 0.56\beta_0^{12/5}\right)^{7/6}} \right. \\ &\quad \left. + \frac{0.51\sigma_B^2}{\left(1 + 0.69\sigma_B^{12/5}\right)^{5/6}} + \frac{0.51\beta_0^2}{\left(1 + 0.69\beta_0^{12/5}\right)^{5/6}} \right] - 1, \end{aligned} \quad (163)$$

where $\sigma_B^2 \equiv \sigma_{I, \text{beam}}^2(0, L)$ is the weak fluctuation scintillation index defined by Eq. (156) and $\beta_0^2 = 0.5C_n^2 k^{7/6} L^{11/6}$ is the Rytov variance for a spherical wave.

When inner scale and outer scale effects are taken into account, the sum of large-scale log-irradiance fluctuations in (162) is described by

$$\sigma_{\ln X, \text{beam}}^2(L) + \sigma_{\ln X, \text{sp}}^2(L) = \sigma_{\ln X, BS}^2(l_0) - \sigma_{\ln X, BS}^2(L_0), \quad (164)$$

where

$$\begin{aligned} \sigma_{\ln X, BS}^2(l_0) &= 0.49\sigma_1^2 \left(\frac{1}{3} - \frac{1}{2}\overline{\Theta}_1 + \frac{1}{5}\overline{\Theta}_1^2 \right) \left(\frac{\eta_{BX}Q_l}{\eta_{BX} + Q_l} \right)^{7/6} \\ &\quad \times \left[1 + 1.75 \left(\frac{\eta_{BX}}{\eta_{BX} + Q_l} \right)^{1/2} - 0.25 \left(\frac{\eta_{BX}}{\eta_{BX} + Q_l} \right)^{7/12} \right] \\ &\quad + 0.02\sigma_1^2 \left(\frac{\eta_{SX}Q_l}{\eta_{SX} + Q_l} \right)^{7/6} \\ &\quad \times \left[1 + 1.75 \left(\frac{\eta_{SX}}{\eta_{SX} + Q_l} \right)^{1/2} - 0.25 \left(\frac{\eta_{SX}}{\eta_{SX} + Q_l} \right)^{7/12} \right], \end{aligned} \quad (165)$$

$$\begin{aligned}
\sigma_{\ln X, BS}^2(L_0) = & 0.49\sigma_1^2 \left(\frac{1}{3} - \frac{1}{2}\overline{\Theta}_1 + \frac{1}{5}\overline{\Theta}_1^2 \right) \left(\frac{\eta_{BX0}Q_l}{\eta_{BX0} + Q_l} \right)^{7/6} \\
& \times \left[1 + 1.75 \left(\frac{\eta_{BX0}}{\eta_{BX0} + Q_l} \right)^{1/2} - 0.25 \left(\frac{\eta_{BX0}}{\eta_{BX0} + Q_l} \right)^{7/12} \right] \\
& + 0.02\sigma_1^2 \left(\frac{\eta_{SX0}Q_l}{\eta_{SX0} + Q_l} \right)^{7/6} \\
& \times \left[1 + 1.75 \left(\frac{\eta_{SX0}}{\eta_{SX0} + Q_l} \right)^{1/2} - 0.25 \left(\frac{\eta_{SX0}}{\eta_{SX0} + Q_l} \right)^{7/12} \right]. \quad (166)
\end{aligned}$$

The parameters appearing in (165) and (166) are defined by

$$\frac{1}{\eta_{BX}} = \frac{0.38}{1 - 3.21\overline{\Theta}_1 + 5.29\overline{\Theta}_1^2} + 0.47\sigma_1^2 Q_l^{1/6} \left(\frac{\frac{1}{3} - \frac{1}{2}\overline{\Theta}_1 + \frac{1}{5}\overline{\Theta}_1^2}{1 + 2.20\overline{\Theta}_1} \right)^{6/7}. \quad (167)$$

$$\eta_{SX} = \frac{8.56}{1 + 0.078\sigma_1^2 Q_l^{1/6}}, \quad (168)$$

$$\eta_{BX0} = \frac{\eta_{BX}Q_0}{\eta_{BX} + Q_0}, \quad \eta_{SX0} = \frac{\eta_{SX}Q_0}{\eta_{SX} + Q_0}. \quad (169)$$

Similarly, the small-scale log-irradiance variance (on axis) is

$$\sigma_{\ln Y, BS}^2(l_0) = \frac{0.51\sigma_G^2}{(1 + 0.69\sigma_G^{12/5})^{5/6}} + \frac{0.51\sigma_{SP}^2}{(1 + 0.69\sigma_{SP}^{12/5})^{5/6}}, \quad (170)$$

where σ_G^2 is the weak fluctuation beam wave scintillation index based on the modified atmospheric spectrum. Its specific form is

$$\begin{aligned}
\sigma_G^2 = & 3.86\sigma_1^2 \left\{ 0.40 \frac{[(1 + 2\overline{\Theta}_1)^2 + (2\Lambda_1 + 3/Q_l)^2]^{11/12}}{[(1 + 2\overline{\Theta}_1)^2 + 4\Lambda_1^2]^{1/2}} \left[\sin\left(\frac{11}{6}\varphi_2 + \varphi_1\right) \right. \right. \\
& + \frac{2.61}{[(1 + 2\overline{\Theta}_1)^2 Q_l^2 + (3 + 2\Lambda_1 Q_l)^2]^{1/4}} \sin\left(\frac{4}{3}\varphi_2 + \varphi_1\right) \\
& - \frac{0.52}{[(1 + 2\overline{\Theta}_1)^2 Q_l^2 + (3 + 2\Lambda_1 Q_l)^2]^{7/24}} \sin\left(\frac{5}{4}\varphi_2 + \varphi_1\right) \Big] \\
& - \frac{13.40\Lambda_1}{Q_l^{11/6}[(1 + 2\overline{\Theta}_1)^2 + 4\Lambda_1^2]} - \frac{11}{6} \left[\left(\frac{1 + 0.31\Lambda_1 Q_l}{Q_l} \right)^{5/6} \right. \\
& \left. \left. + \frac{1.10(1 + 0.27\Lambda_1 Q_l)^{1/3}}{Q_l^{5/6}} - \frac{0.19(1 + 0.24\Lambda_1 Q_l)^{1/4}}{Q_l^{5/6}} \right] \right\}, \quad (171)
\end{aligned}$$

where $Q_l = 10.89L/kl_0^2$ is the inner scale parameter and

$$\varphi_1 = \tan^{-1}\left(\frac{2\Lambda_1}{1+2\Theta_1}\right), \quad \varphi_2 = \tan^{-1}\left[\frac{(1+2\Theta_1)Q_l}{3+2\Lambda_1Q_l}\right]. \quad (172)$$

Similarly, the expression σ_{SP}^2 is the weak fluctuation scintillation index of a spherical wave defined by

$$\begin{aligned} \sigma_{SP}^2 \cong 9.65\beta_0^2 \Big\{ & 0.40(1+9/Q_l^2)^{11/12} \left[\sin\left(\frac{11}{6}\tan^{-1}\frac{Q_l}{3}\right) \right. \\ & \left. + \frac{2.61}{(9+Q_l^2)^{1/4}} \sin\left(\frac{4}{3}\tan^{-1}\frac{Q_l}{3}\right) - \frac{0.52}{(9+Q_l^2)^{7/24}} \sin\left(\frac{5}{4}\tan^{-1}\frac{Q_l}{3}\right) \right] - \frac{3.50}{Q_l^{5/6}} \Big\}. \end{aligned} \quad (173)$$

The total scintillation is then described at all points within the plane of the received optical wave by

$$\begin{aligned} \sigma_I^2(2l)_{\text{bistatic}} = \exp[& \sigma_{\ln X, BS}^2(L_0) - \sigma_{\ln X, BS}^2(L_0) \\ & + \frac{0.51\sigma_G^2}{(1+0.69\sigma_G^{12/5})^{5/6}} + \frac{0.51\sigma_{SP}^2}{(1+0.69\sigma_{SP}^{12/5})^{5/6}}] - 1. \end{aligned} \quad (174)$$

In the saturation regime ($\beta_0^2 \rightarrow \infty$) the small-scale log-irradiance variance (170) has the asymptotic limit $\sigma_{\ln Y, BS}^2(l_0) \rightarrow \ln 2 + \ln 2 = 2 \ln 2$, regardless of inner-scale/outer-scale effects. Thus, the limiting value of the scintillation index in the saturation regime of the return Gaussian-beam wave from an unresolved (point) target is 3, not unity as in the one-way propagation channel.

In a *monostatic channel*, the receiver-plane scintillation index under weak irradiance fluctuations has the general form [12,23]right]

$$\begin{aligned} \sigma_I^2(\mathbf{r}, 2L)_{\text{monostatic}} &= \sigma_I^2(\mathbf{r}, 2L)_{\text{bistatic}} + 2C_{\ln I}^{iR}(\mathbf{r}, L) \\ &= \sigma_{\ln I, \text{beam}}^2(0, L) + \sigma_{\ln I, \text{sp}}^2(L) + 2C_{\ln I}^{iR}(\mathbf{r}, L), \end{aligned} \quad (175)$$

where fluctuations induced by the correlation between incident and echo waves are defined by (155). Once again we have written the expressions in terms of the log-irradiance fluctuations, but, unlike the bistatic case, here the scintillation index (175) depends on position \mathbf{r} in the beam profile at the receiver. Nonetheless, we will develop the strong fluctuation results below based only on $r = 0$. That is, for $r > 0$ the monostatic channel essentially reduces to that of a bistatic channel over relatively short transverse distances. Because the added scintillation on the optical axis caused by the correlation term $C_{\ln I}^{iR}(0, L)$ is the same as the correlation function (135) occurring in the the BSAE, i.e., $C_{\ln I}^{iR}(0, L) = B_{\ln X}^{iR}(0, L)$, the strong fluctuation representation of the irradiance correlation is [see Eq. (139)]

$$C_I^{iR}(0, L) = \exp[B_{\ln X}^{iR}(0, L)] - 1. \quad (176)$$

In developing the expression for the monostatic channel scintillation index we start with the scintillation model described by (38) but with $r = 0$. Here the normalized second moment of the modulation term $C(0)$ can be expressed as [17]

$$\frac{\langle C^2(0) \rangle}{\langle C(0) \rangle^2} = 1 + \frac{2C_I^{iR}(0, L)}{\exp[2B_{\ln I}^{iR}(0, L)]} = 1 + \frac{2 \exp[B_{\ln I}^{iR}(0, L)] - 2}{\exp[2B_{\ln I}^{iR}(0, L)]}, \quad (177)$$

from which we deduce

$$\sigma_I^2(0, 2L)_{\text{monostatic}} = \sigma_I^2(2L)_{\text{bistatic}} + 2 \{ \exp[-B_{\ln I}^{iR}(0, L)] - \exp[-2B_{\ln I}^{iR}(0, L)] \} [1 + \sigma_I^2(2L)_{\text{bistatic}}]. \quad (178)$$

Under the assumption of a Kolmogorov spectrum the bistatic channel scintillation is defined by (163) and $B_{\ln X}^{iR}(0, L)$ by (139). When inner-scale and outer-scale effects cannot be ignored, the bistatic scintillation index is defined by (174) and the far-field approximation ($\Lambda_0 > 1$) to $B_{\ln X}^{iR}(0, L)$ is defined by (141)–(145).

In Fig. 13.21 we show the on-axis scintillation index as a function of $\sigma_1(L)$ for both a bistatic channel and a monostatic channel associated with a collimated Gaussian-beam wave reflected from a point target. The assumed spot radius of the beam at the transmitter is $W_0 = 1$ cm, the optical wavelength is set at $\lambda = 1.06 \mu\text{m}$ and inner-scale and outer-scale effects are ignored. For illustrative purposes we also show the same Gaussian-beam wave propagating one way from the transmitter to the target (i.e., the illumination beam). Under weak fluctuations there is a twofold increase in the scintillation for the double-passage wave in a bistatic channel over that of the illumination beam, and at peak values of the scintillation index our strong-fluctuation model predicts roughly a fourfold increase. In a monostatic channel, however, weak fluctuation theory predicts a fourfold

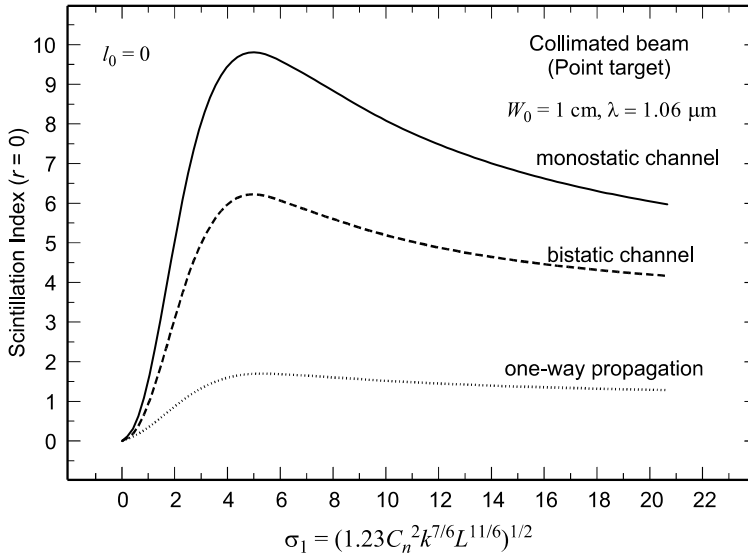


Figure 13.21 The on-axis scintillation index of collimated Gaussian-beam wave reflected from a point target as a function of the root-mean-square Rytov variance.

increase over the one-way path and our model predicts a sixfold increase near peak values of the scintillation. Similar to the bistatic case, the saturation limit for the scintillation index of a Gaussian-beam wave in a monostatic channel is 3.

13.8 Diffuse Target

Surfaces that are rough on the scale of a wavelength are often modeled as a *diffuse surface*, or *Lambertian reflector*. Basically, this means that the correlation width of the surface roughness is much smaller than the coherence radius of the illumination beam. In this case the correlation width of the surface roughness is described by a delta function (see also Section 16.8). Although a true Lambertian surface does not exist, it is still a useful model for theoretical studies involving optical scattering by a rough surface or by atmospheric aerosols. Our analysis below will be based on a diffuse target model, relying largely on results in Ref. [18] for analytic expressions under weak fluctuation conditions.

13.8.1 Mean irradiance and BSAE

The *mean irradiance* of a Gaussian-beam wave reflected from a finite diffuse surface in a monostatic channel can be expressed in the form

$$\langle(\mathbf{r}, 2L)\rangle \cong \frac{T_0^2}{2L^2} \frac{W_0^2}{(1 + \Omega_R/\Lambda_1) \left[1 + 1.33\sigma_1^2 \left(\frac{\Lambda_1 \Omega_R}{\Lambda_1 + \Omega_R} \right)^{5/6} \right]} \exp[B_I^{iR}(\mathbf{r}, L)], \quad (179)$$

where T_0 is a reflection coefficient and $\Omega_R = 2L/kW_R^2$ is once again a nondimensional parameter characterizing the finite radius W_R of the target. In this case the only radial dependency in the mean irradiance appears in the enhancement term. The correlation function in (179) for a Gaussian beam incident on a finite diffuse surface is

$$\begin{aligned} B_I^{iR}(\mathbf{r}, L) = & 8\pi^2 k^2 L \int_0^1 \int_0^\infty \kappa \Phi_n(\kappa) J_0(\kappa \xi r) \exp \left[-\frac{L\kappa^2 \xi^2}{2k} \left(\frac{\Lambda_1 \Omega_R + \Theta_1/2}{\Lambda_1 + \Omega_R} \right) \right] \\ & \times \left\{ \cos \left[\frac{L\kappa^2 \xi^2}{2k} \left(\frac{\Theta_1 \Omega_R}{\Lambda_1 + \Omega_R} \right) \right] - \cos \left[\frac{L\kappa^2 \xi}{2k} \left(2 - 2\xi + \frac{\Theta_1 \Omega_R \xi}{\Lambda_1 + \Omega_R} \right) \right] \right\} d\kappa d\xi. \end{aligned} \quad (180)$$

For the limiting case of a diffuse point target ($\Omega_R \gg 1$), the correlation function (180) reduces to that given by Eq. (132) for an unresolved (point) target. It also follows that in the case of an incident spherical wave, Eq. (180) reduces to

$$\begin{aligned} B_I^{iR}(\mathbf{r}, L) & \equiv B_{I,sp}(\mathbf{r}, L) \\ & = 8\pi^2 k^2 L \int_0^1 \int_0^\infty \kappa \Phi_n(\kappa) J_0(\kappa \xi r) \left\{ 1 - \cos \left[\frac{L\kappa^2}{k} \xi(1 - \xi) \right] \right\} d\kappa d\xi, \end{aligned} \quad (181)$$

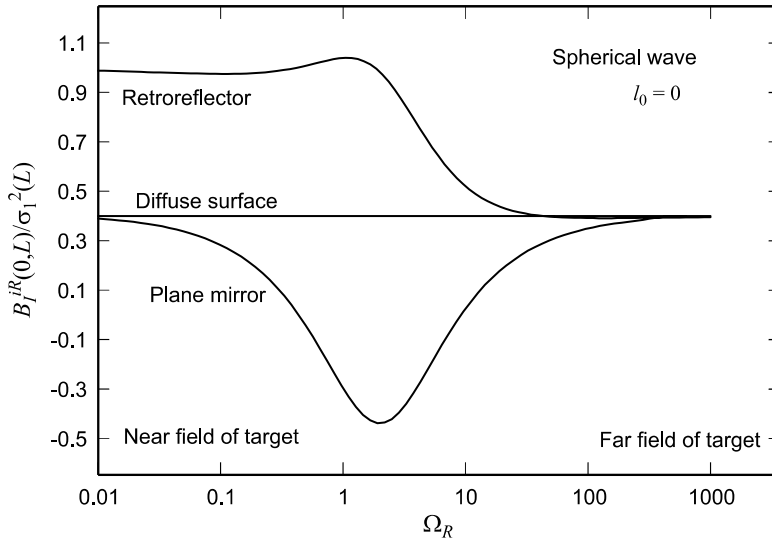


Figure 13.22 The scaled correlation function for a reflected spherical wave from three distinct types of targets.

which is interesting in that it reveals that the amplification factor $N(\mathbf{r}) = \exp[B_f^R(\mathbf{r}, L)]$ is independent of the size of the scattering surface in this case! That is, the size of the surface affects only the absolute intensity of the received signal when the target is illuminated by a spherical wave.

A comparison of the scaled correlation functions based on three target models and the special case of an incident spherical wave is shown in Fig. 13.22 as a function of target size and $r = 0$. For illustrative purposes we have taken the case of zero inner scale and infinite outer scale governed by the Kolmogorov spectrum. In Fig. 13.23 we illustrate the same for various-size collimated beams. Here we see that the behavior is not the same as for the spherical wave case (also shown for comparison) and, in fact, is strongly dependent on transmitter beam size in comparison with the target size. As the transmitter beam gets larger and the target is also large ($\Omega_R < 10^{-2}$), we find that the correlation function gets closer to zero. However, the correlation function of a large beam reflected from a very small diffuse target ($\Omega_R > 10^2$) approaches that of a spherical wave.

13.8.2 Spatial coherence

In the case of a diffuse surface, it has been shown that the modulus of the complex degree of coherence is the same as that for an incident spherical wave on a point target (Section 13.7.3), except that it is multiplied by the factor $\exp(-k\rho^2/4L\Omega_R)$ [18]. Waves reflected from a diffuse surface, therefore, suffer an additional deterioration in coherence as compared with a point target. In particular, a sufficiently large diffuse surface ($\Omega_R \ll 1$) ensures that the reflected wave field becomes completely incoherent.

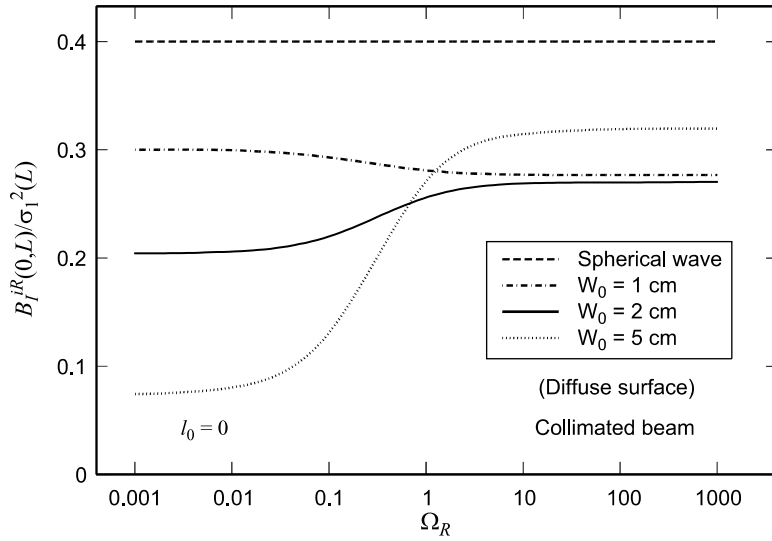


Figure 13.23 The scaled correlation function for a reflected collimated beam wave from a diffuse target. The limiting case of a spherical wave is also shown.

13.8.3 Scintillation index—Part I

The scattering properties of physical diffuse targets such as atmospheric aerosols, a sea surface, or a rough surface can vary with time when scanned by a laser radar. Suppose we let τ_c denote the characteristic correlation time between fluctuations in surface irregularities in the target and τ_d denote the time constant of the detector at the receiver. The relative size of these time constants is important in the development of our scintillation models.

To begin, we consider the scenario where the illumination beam is the limiting case of a spherical wave and assume the detector does not respond directly with the temporal variations in the reflected wave caused by the rough surface, i.e., $\tau_d \gg \tau_c$. The scintillation index of the reflected spherical wave under weak irradiance fluctuations can be expressed as

$$\sigma_I^2(\mathbf{r}, 2L) = 2\sigma_{I, \text{diff}}^2(L) + 2C_{I, \text{diff}}^{iR}(\mathbf{r}, L), \quad (182)$$

where

$$C_{I, \text{diff}}^{iR}(\mathbf{r}, L) = 8\pi^2 k^2 L \int_0^1 \int_0^\infty \kappa \Phi_n(\kappa) \exp\left(-\frac{L\kappa^2 \xi^2}{2k\Omega_R}\right) J_0[(1-\xi)\kappa r] \\ \times \left\{ 1 - \cos\left[\frac{L\kappa^2}{k} \xi(1-\xi)\right] \right\} d\kappa d\xi, \quad (183)$$

$$\sigma_{I, \text{diff}}^2(L) = C_{I, \text{diff}}^{iR}(0, L). \quad (184)$$

To develop mathematical models for the scintillation index, we first consider the case of a *bistatic channel*, which leads to

$$\sigma_I^2(\mathbf{r}, 2L)_{\text{bistatic}} = 2\sigma_{I, \text{diff}}^2(L). \quad (185)$$

Note that the term (184) is mathematically equivalent to the flux variance of a spherical wave [see Eq. (70) in Chap. 10] that results from the use of a large collecting aperture for the detector. Of course, this is a consequence of the fact that a diffuse target acts like a finite incoherent source that produces an aperture-averaging effect at the receiver. Based on strong fluctuation theory, we deduce that the scintillation index can be written as

$$\begin{aligned} \sigma_I^2(\mathbf{r}, 2L)_{\text{bistatic}} &= \exp[2\sigma_{\ln I, \text{diff}}^2(L)] - 1 \\ &= \{\exp[\sigma_{\ln I, \text{diff}}^2(L)] - 1\} \{\exp[\sigma_{\ln I, \text{diff}}^2(L)] + 1\} \\ &= \sigma_{I, \text{diff}}^2(L)[2 + \sigma_{I, \text{diff}}^2(L)], \end{aligned} \quad (186)$$

where we have simply factored the top expression and identified each of the factors based on $\sigma_{\ln I, \text{diff}}^2(L) = \exp[\sigma_{\ln I, \text{diff}}^2(L)] - 1$. Hence, based on the expression given by Eq. (77) in Chap. 10 with $d = (kW_R^2/L)^{1/2} = \sqrt{2/\Omega_R}$, we deduce that the scintillation index for a bistatic channel is that given by (186) where

$$\begin{aligned} \sigma_{I, \text{diff}}^2(L) &\cong \exp \left[\frac{0.49\beta_0^2}{\left(1 + 0.36\Omega_R^{-1} + 0.56\beta_0^{12/5}\right)^{7/6}} \right. \\ &\quad \left. + \frac{0.51\beta_0^2(1 + 0.69\beta_0^{12/5})^{-5/6}}{1 + 1.80\Omega_R^{-1} + 1.24\Omega_R^{-1}\beta_0^{12/5}} \right] - 1. \end{aligned} \quad (187)$$

Accounting for a finite inner scale and finite outer scale through the modified atmospheric spectrum, we have that

$$\begin{aligned} \sigma_{I, \text{diff}}^2(L) &= \exp \left[\sigma_{\ln X}^2(\Omega_R, l_0) - \sigma_{\ln X}^2(\Omega_R, L_0) \right. \\ &\quad \left. + \frac{0.51\sigma_{SP}^2(1 + 0.69\sigma_{SP}^{12/5})^{-5/6}}{1 + 1.80\Omega_R^{-1}(\beta_0/\sigma_{SP})^{12/5} + 1.24\Omega_R^{-1}\beta_0^{12/5}} \right] - 1, \end{aligned} \quad (188)$$

where

$$\begin{aligned} \sigma_{\ln X}^2(\Omega_R, l_0) &\cong 0.04\beta_0^2(L) \left(\frac{\eta_{Xd}Q_l}{\eta_{Xd} + Q_l} \right)^{7/6} \\ &\quad \times \left[1 + 1.75 \left(\frac{\eta_{Xd}}{\eta_{Xd} + Q_l} \right)^{1/2} - 0.25 \left(\frac{\eta_{Xd}}{\eta_{Xd} + Q_l} \right)^{7/12} \right], \end{aligned} \quad (189)$$

$$\sigma_{\ln X}^2(\Omega_R, L_0) \cong 0.04\beta_0^2(L) \left(\frac{\eta_{Xd0} Q_l}{\eta_{Xd0} + Q_l} \right)^{7/6} \times \left[1 + 1.75 \left(\frac{\eta_{Xd0}}{\eta_{Xd0} + Q_l} \right)^{1/2} - 0.25 \left(\frac{\eta_{Xd0}}{\eta_{Xd0} + Q_l} \right)^{7/12} \right], \quad (190)$$

$$\eta_x = \frac{8.56}{1 + 0.20\beta_0^2 Q_l^{1/6}}, \quad (191)$$

$$\eta_{Xd} = \frac{\eta_x}{1 + 0.04\Omega_R^{-1}\eta_x} = \frac{8.56}{1 + 0.36\Omega_R^{-1} + 0.20\beta_0^2 Q_l^{1/6}}, \quad (192)$$

$$\eta_{Xd0} = \frac{\eta_{Xd} Q_0}{\eta_{Xd} + Q_0}. \quad (193)$$

In the case of a *monostatic channel*, we obtain (along the optical axis $r = 0$)

$$\sigma_{I'}^2(0, 2L)_{\text{monostatic}} = \sigma_{I, \text{diff}}^2(L) [2 + \sigma_{I, \text{diff}}^2(L)] + \frac{2\sigma_{I, \text{diff}}^2(L)}{[1 + \sigma_{I, \text{sp}}^2(L)]^2} \{1 + \sigma_{I, \text{diff}}^2(L) [2 + \sigma_{I, \text{diff}}^2(L)]\}, \quad (194)$$

where, based on a Kolmogorov spectrum, $\sigma_{I, \text{diff}}^2(L)$ is defined by (187) and

$$\sigma_{I, \text{sp}}^2(L) = \exp \left[\frac{0.49\beta_0^2}{(1 + 0.56\beta_0^{12/5})^{7/6}} + \frac{0.51\beta_0^2}{(1 + 0.69\beta_0^{12/5})^{-5/6}} \right] - 1. \quad (195)$$

Otherwise, we use (188) above and (83) in Chap. 9 when inner scale and/or outer scale effects are included.

The scintillation index for a spherical wave reflected from a diffuse surface is shown in Fig. 13.24 by the dotted curves. We have used the modified atmospheric spectrum and chosen an inner scale such that $Q_l = 10.89L/kl_0^2 = 100$. For comparison, we have also plotted similar curves arising from a finite plane mirror and a retroreflector. Note that off-axis fluctuations ($r = W$) depicting a bistatic channel for the diffuse surface are less than on-axis fluctuations ($r = 0$) depicting a monostatic channel for any size target. Moreover, the fluctuations decrease to zero as the target size increases in both bistatic and monostatic channels. Off-axis fluctuations for smooth targets (plane mirror and retroreflector) are less than on-axis fluctuations only for very small targets or very large targets.

13.8.4 Scintillation index—Part II

When the time constant of the detector satisfies $\tau_d \ll \tau_c$, the detector follows the temporal distortions of the reflected radiation due to time variations in surface irregularities. In this case the received irradiance exhibits a multiplicative speckle

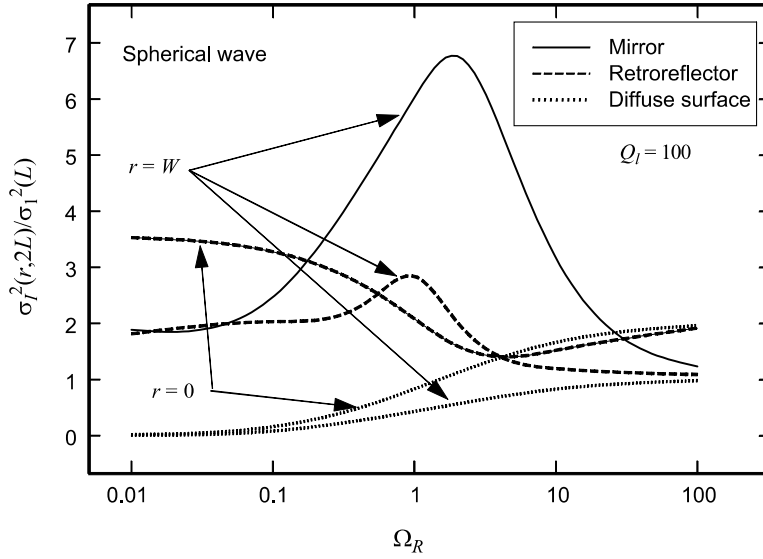


Figure 13.24 The scaled scintillation index for a reflected spherical wave from three types of finite targets with inner scale parameter $Q_I = 10.89 L/k\ell_0^2 = 100$. The curves with $r = 0$ correspond to the optical axis and those with $r = W$ represent the diffractive beam edge.

term [24] which we introduce through another modulation of the irradiance of the received wave, i.e.,

$$I = SI_1, \quad (196)$$

where S is the random surface quantity describing temporal variations in the surface irregularities and I_1 denotes the irradiance that would be detected at the receiver if the surface irregularities were “frozen” in time. In general we assume negative exponential statistics [25] for S so that if the irradiance is normalized, $\langle S \rangle = 1$ and $\langle S^2 \rangle = 2$. Therefore, the resulting scintillation index under weak irradiance fluctuations takes the form

$$\sigma_I^2(\mathbf{r}, 2L) = 1 + 4\sigma_{I,\text{diff}}^2(L) + 4C_{I,\text{diff}}^{iR}(\mathbf{r}, L), \quad (197)$$

where the terms on the right-hand side are those defined by (183) and (184). Under general conditions, the scintillations are readily deduced from the results given above. For a bistatic channel, this yields

$$\sigma_I^2(\mathbf{r}, 2L)_{\text{bistatic}} = 1 + 2\sigma_{I,\text{diff}}^2(L)[2 + \sigma_{I,\text{diff}}^2(L)], \quad (198)$$

where $\sigma_{I,\text{diff}}^2(L)$ is defined by (187) or (188). Similarly, for the monostatic channel the comparable expression is ($r = 0$)

$$\begin{aligned} \sigma_I^2(0, 2L)_{\text{monostatic}} = & 1 + 2\sigma_{I,\text{diff}}^2(L)[2 + \sigma_{I,\text{diff}}^2(L)] \\ & + \frac{4\sigma_{I,\text{diff}}^2(L)}{[1 + \sigma_{I,\text{sp}}^2(L)]^2} \{1 + \sigma_{I,\text{diff}}^2(L)[2 + \sigma_{I,\text{diff}}^2(L)]\}. \end{aligned} \quad (199)$$

For a limiting case of a point diffuse surface ($W_R \ll \sqrt{L/K}$) and Kolmogorov spectrum, we find that (198) and (199) in the saturation regime reduce to the asymptotic expressions

$$\sigma_I^2(0, 2L) \cong \begin{cases} 7 + \frac{15.12}{\beta_0^{4/5}}, & \beta_0^2 \gg 1 \quad (\text{bistatic}) \\ 11 + \frac{22.8}{\beta_0^{4/5}}, & \beta_0^2 \gg 1 \quad (\text{monostatic}). \end{cases} \quad (200)$$

For comparison, we remark that Banakh and Mironov [18] previously obtained the asymptotic result for a monostatic channel given by

$$\sigma_I^2(0, 2L) \cong \frac{11 + 66.13\beta_0^{-4/5}}{1 + 1.89\beta_0^{-4/5}} \cong 11 + \frac{44.16}{\beta_0^{4/5}}, \quad \beta_0^2 \gg 1. \quad (201)$$

Note that there is a factor of 2 difference in the second term of the monostatic expressions in (200) and (201). The cause of this difference is unknown but it may be attributed to a difference in method leading to the asymptotic expansions. We will point out that (199) and (201) predict quite similar results over a wide range of turbulence conditions.

In Fig. 13.25 we plot the on-axis double-pass scintillation index (199) for a monostatic channel as a function of normalized target size and conditions of irradiance fluctuations corresponding to weak, moderate, and strong. In all cases the scintillation index approaches the limiting value of unity for an infinitely large target, but in the saturation regime where $\beta_0^2 = 36$, there is a leveling effect between 0.5 and 5 on the horizontal axis caused by the emergence of the two-scale phenomenon that led to the extended Rytov method discussed in Chap. 9.

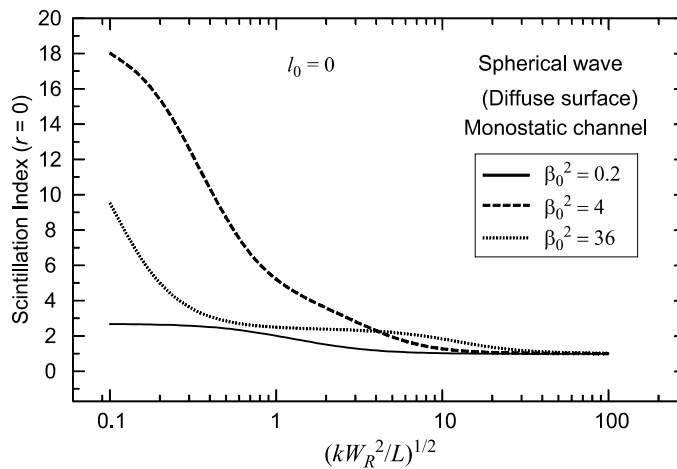


Figure 13.25 Scintillation index for a spherical wave reflected from a diffuse (Lambert) surface of radius W_R . Inner scale effects are neglected.

13.9 Summary and Discussion

In this chapter we have developed analytic expressions for several enhanced backscatter (EBS) effects associated with the double passage of an optical wave through the same inhomogeneities of a random medium after reflection from various targets of finite size. The EBS effects include a narrow peak in the mean irradiance known as the backscatter amplification effect (BSAE), an increase in the normalized variance of irradiance, and an increase or decrease in spatial coherence dependent upon target characteristics. Targets considered in this analysis include smooth surfaces (mirrors and retroreflectors) and diffuse surfaces (Lambertian target). In addition, this analysis includes the influence of inner scale and the high-wave-number rise associated with the modified atmospheric spectrum.

In particular, for smooth surface targets, the modified atmospheric spectrum with high-wave-number rise and inner scale generally predicts greater amplitude enhancements in the reflected wave than predicted by the pure power-law spectrum of Kolmogorov. But, a finite outer scale in the spectral model leads to a reduction in the amount of beam spreading caused by turbulence and, in the case of a retroreflector, also leads to a reduction in the peak amplitude enhancement on the optical axis. This last result is in contrast with a plane mirror reflector where outer scale effects tend to increase the peak amplitude enhancement on the optical axis. The theory also predicts that, except for small reflectors, the coherence radius associated with a retroreflector can be as much as 2 times larger than that associated with a plane mirror, and 1.5 times that of a bistatic configuration for a plane mirror. In addition, values of the normalized irradiance variance based on the modified atmospheric spectrum of refractive-index fluctuations with high-wave-number rise and inner scale parameter can be up to 35% greater than those predicted by the Kolmogorov power law spectrum when the inner scale is comparable in size with the first Fresnel zone.

In general, the statistics associated with a diffuse surface are very different from those of a smooth reflector. For example, the amplification factor $N(\mathbf{r}) = \exp[B_I^{iR}(\mathbf{r}, L)]$ associated with the BSAE is independent of the size of the scattering surface in the case of an incident spherical wave. That is, the size of the surface affects only the absolute intensity of the received signal. For other incident waves, like a general Gaussian beam, the size of the diffuse surface can play a significant role. In the strictly backward direction, the peak enhancement in the irradiance from an incident spherical wave is determined by the scintillation index of the incident wave. Off-axis ($r = W$) fluctuations in the irradiance for the diffuse surface are less than on-axis ($r = 0$) fluctuations for any size target, and the fluctuations decrease to zero (or unity if temporal variations of the target are taken into account) as the target size increases. Off-axis fluctuations for smooth targets (plane mirror and retroreflector) are less than on-axis fluctuations only for very small targets or very large targets.

Last, it should be pointed out that the Gaussian mirror models used in this analysis do not predict exactly the same behavior that would occur if edge diffraction effects were taken into account [26]. Banakh [27,28] has shown that edge

diffraction on a reflector (both plane mirror and retroreflector) has a profound effect on the irradiance distribution of the reflected wave under weak fluctuations. This effect has important consequences on the resolution of coherent images of a target in random media and on adaptive optics systems that use reflected radiation as a reference signal. Therefore, results based on the Gaussian models used here to describe the finite dimension of the reflector must be treated as average behavior, not absolute behavior, of the reflected wave.

13.10 Worked Examples

Example 1: Plot the spot size ratio W/W_0 for a collimated beam reflected from a smooth finite target as a function of Fresnel ratio Ω_R depicting reflector size.

Solution: Here we select a collimated beam characterized by $\Theta_0 = \Lambda_0 = 1$. In this case, we find that $\Theta_1 = \Lambda_1 = 1/2$ from (14), and with Λ_2 defined by (15), the ratio we seek can be found from the relation

$$\frac{W}{W_0} = \sqrt{\frac{\Lambda_0}{\Lambda_2}}.$$

In Fig. 13.26 we show this ratio as a function of $\Omega_R = 2L/kW_R^2$, where W_R is the reflector spot size. The spot size of the reflected beam is clearly minimum for $\Omega_R \sim 1$.

□

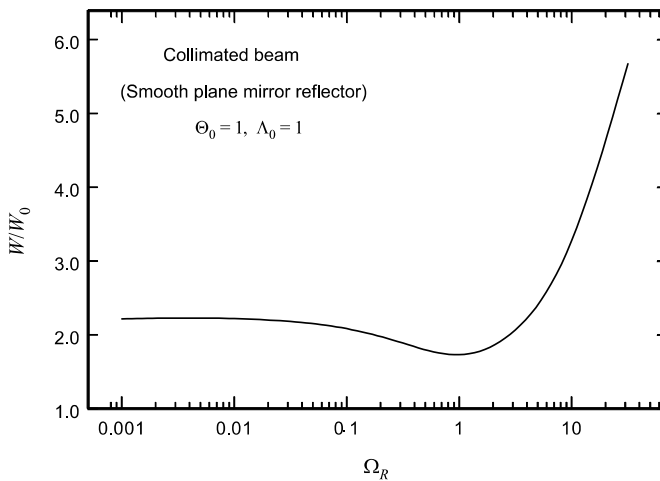


Figure 13.26 Spot size of reflected beam, scaled by the spot size of the transmitted beam, shown as a function of target Fresnel ratio.

Example 2: Consider an unresolved target located at range 5 km. If a lidar system uses a 4 cm diameter collimated beam operating in a monostatic configuration at wavelength $\lambda = 1.06 \mu\text{m}$ and $C_n^2 = 2 \times 10^{-13} \text{m}^{-2/3}$, calculate the following:

- (a) The BSAE on the optical axis.
- (b) The corresponding scintillation index for the same lidar system operating in a bistatic configuration.
- (c) What is the on-axis scintillation index for a monostatic system?
- (d) What is the on-axis scintillation index for the illumination beam?

Solution: We first calculate the quantities:

$$\Theta_0 = 1 - \frac{L}{F_0} = 1, \quad \Lambda_0 = \frac{2L}{kW_0^2} = 4.2176, \quad \sigma_1^2 = 1.23C_n^2 k^{7/6} L^{11/6} = 118.6$$

$$\Theta = 0.0532, \quad \Lambda = 0.2245, \quad \beta_0^2 = 0.5C_n^2 k^{7/6} L^{11/6} = 48.21$$

$$(a) \quad N(0) = \exp \left[\frac{\sigma_{B,C}^2}{\left(1 + 0.58\sigma_{B,C}^{12/5}\right)^{7/6}} \right] = 1.59.$$

$$(b) \quad \sigma_I^2(2L)_{\text{bistatic}} = \exp \left[\frac{0.49\sigma_B^2}{\left[1 + 0.56(1 + \Theta_1)\sigma_B^{12/5}\right]^{7/6}} + \frac{0.49\beta_0^2}{\left(1 + 0.56\beta_0^{12/5}\right)^{7/6}} \right. \\ \left. + \frac{0.51\sigma_B^2}{\left(1 + 0.69\sigma_B^{12/5}\right)^{5/6}} + \frac{0.51\beta_0^2}{\left(1 + 0.69\beta_0^{12/5}\right)^{5/6}} \right] - 1 \\ = 5.11.$$

$$(c) \quad \sigma_I^2(0, 2L)_{\text{monostatic}} = \sigma_I^2(2L)_{\text{bistatic}} \\ + 2 \left\{ \exp[-B_{\ln I}^{iR}(0, L)] - \exp[-2B_{\ln I}^{iR}(0, L)] \right\} \\ \times \left[1 + \sigma_I^2(2L)_{\text{bistatic}} \right] \\ = 7.95.$$

$$(d) \quad \sigma_I^2(0, L) = 1.51.$$

□

Problems

Section 13.3

1. If a Gaussian beam incident on a finite smooth target is characterized by beam parameters Θ_1 and Λ_1 and if the target size is characterized by Ω_R , show that Eqs. (9) in Chap. 10 lead to

$$\Theta_2 = \frac{2 - \Theta_1}{(2 - \Theta_1)^2 + (\Lambda_1 + \Omega_R)^2}, \quad \Lambda_2 = \frac{\Lambda_1 + \Omega_R}{(2 - \Theta_1)^2 + (\Lambda_1 + \Omega_R)^2}.$$

2. For a point target ($\Omega_R \rightarrow \infty$), deduce from Eqs. (23)–(26) that
 - (a) $\gamma_a^i = 0, \gamma_a^R = \xi$.
 - (b) $\gamma_a^i B_a^i(\xi) = L\xi(1 - \overline{\Theta}_1\xi) - j\Lambda_1 L\xi^2$.
3. For a plane mirror point target ($\Omega_R \rightarrow \infty$), use Eqs. (28)–(31) to determine the products $\gamma_b^i B_b^i(\xi)$ and $\gamma_b^R B_b^R(\xi)$.
4. For a retroreflector point target ($\Omega_R \rightarrow \infty$), use Eqs. (32)–(35) to determine the products $\gamma_b^i B_b^i(\xi)$ and $\gamma_b^R B_b^R(\xi)$.

Section 13.4

5. If $\mathbf{r}_1 = \mathbf{r}_2 = \mathbf{r}$, show that Eq. (45) reduces to Eq. (51).
6. If $\mathbf{r}_1 = \mathbf{r}_2 = \mathbf{r}$, show that Eq. (47) reduces to Eq. (66) for an incident spherical wave.
7. For the case of a spherical wave incident on a finite smooth target of radius W_R ,
 - (a) show that the spot radius in the transceiver plane is

$$W = W_R \sqrt{4 + \Omega_R^2}.$$

- (b) As the target size increases, deduce that the spot radius in the transceiver plane approaches twice the radius of the target.
8. For a spherical wave incident on a finite smooth target, the angular spread of the wave in the transceiver plane is described by Eq. (63).
 - (a) Show that

$$P(\mathbf{r}) = \exp[-2T_R + 4\sigma_r^2(\mathbf{r}, L)] \cong \frac{1}{1 + 2T_R} \exp[+4\sigma_r^2(\mathbf{r}, L)],$$

where T_R is defined by Eq. (54) and

$$\sigma_r^2(\mathbf{r}, L) = 2\pi^2 k^2 L \int_0^1 \int_0^\infty \kappa \Phi_n(\kappa) \exp\left(-\frac{\Lambda_2 L x^2 \xi^2}{k}\right) [1 - I_0(2\Lambda_2 \kappa \xi r)] d\kappa d\xi.$$

- (b) From part (a) and the Kolmogorov spectrum, deduce that the long-term spot size is

$$W_{LT} \cong W_R \sqrt{1 + 2.65\sigma_1^2(L)\Lambda_2^{5/6}}.$$

9. Given the correlation function (66) for a spherical wave incident on a plane mirror target,
 (a) show that the Kolmogorov spectrum and $r = 0$ leads to the expression

$$B_I^{iR}(0, L) = \left(0.4 - 2.65\Lambda_2^{5/6}\right)\sigma_1^2(L).$$

- (b) Deduce from the result in part (a) that there is negative irradiance enhancement for target sizes satisfying

$$0.44 < \Omega_R < 9.24.$$

- (c) Use the von Kármán spectrum [Eq. (20) in Chap. 3] with $l_0 = 0$ to deduce that

$$B_I^{iR}(0, L)/\sigma_1^2(L) = 0.4 - 2.65\Lambda_2^{5/6}[1 - 0.96(\Lambda_2 Q_0)^{1/6}], \quad Q_0 = L\kappa_0^2/k.$$

10. If a spherical wave is incident on an unbounded retroreflector, show that

$$\begin{aligned} B_I^{ir}(\mathbf{r}, L) &= B_{I, pl}(\mathbf{r}, L) \\ &= 8\pi^2 k^2 L \int_0^1 \int_0^\infty \kappa \Phi_n(\kappa) J_0(\kappa r) \left[1 - \cos\left(\frac{L\kappa^2 \xi}{k}\right)\right] d\kappa d\xi. \end{aligned}$$

11. If an unbounded plane wave is incident on an unbounded plane mirror, show that

$$B_I^{iR}(\rho, L) = 8\pi^2 k^2 L \int_0^1 \int_0^\infty \kappa \Phi_n(\kappa) [J_0(\kappa \rho) - 1] \cos\left(\frac{L\kappa^2 \xi}{k}\right) d\kappa d\xi.$$

12. If an unbounded plane wave is incident on an unbounded retroreflector, show that

$$\begin{aligned} B_I^{iR}(\mathbf{p}, \mathbf{r}, L) &= 8\pi^2 k^2 L \int_0^1 \int_0^\infty \kappa \Phi_n(\kappa) J_0(2\kappa r) \cos\left(\frac{L\kappa^2 \xi}{k}\right) d\kappa d\xi \\ &\quad - 4\pi^2 k^2 L \int_0^1 \int_0^\infty \kappa \Phi_n(\kappa) \left\{ J_0(|2\mathbf{r} + \mathbf{p}|\kappa) \exp\left[-\frac{jL\kappa^2}{k}(2 - \xi)\right] \right. \\ &\quad \left. + J_0(|2\mathbf{r} - \mathbf{p}|\kappa) \exp\left[\frac{jL\kappa^2}{k}(2 - \xi)\right] \right\} d\kappa d\xi. \end{aligned}$$

13. If a spherical wave is incident on an unbounded plane mirror, show that

$$\begin{aligned}
 B_{\Gamma}^{iR}(\mathbf{p}, \mathbf{r}, L) = & 4\pi^2 k^2 L \int_0^1 \int_0^\infty \kappa \Phi_n(\kappa) \\
 & \times \left\{ J_0(|\xi \mathbf{r} + \mathbf{p}/2| \kappa) - J_0(|\mathbf{r} + \mathbf{p}/2| \kappa \xi) \exp \left[-\frac{jL\kappa^2}{k} \xi(1 - \xi) \right] \right\} d\kappa d\xi \\
 & + 4\pi^2 k^2 L \int_0^1 \int_0^\infty \kappa \Phi_n(\kappa) \\
 & \times \left\{ J_0(|\xi \mathbf{r} - \mathbf{p}/2| \kappa) - J_0(|\mathbf{r} - \mathbf{p}/2| \kappa \xi) \exp \left[\frac{jL\kappa^2}{k} \xi(1 - \xi) \right] \right\} d\kappa d\xi.
 \end{aligned}$$

14. If a spherical wave is incident on an unbounded retroreflector, show that

$$\begin{aligned}
 B_{\Gamma}^{iR}(\mathbf{p}, \mathbf{r}, L) = & 4\pi^2 k^2 L \int_0^1 \int_0^\infty \kappa \Phi_n(\kappa) \\
 & \times \left\{ J_0(|\mathbf{r} + \xi \mathbf{p}/2| \kappa) - J_0(|\mathbf{r} + \mathbf{p}/2| \kappa) \exp \left[-\frac{jL\kappa^2}{k} (1 - \xi) \right] \right\} d\kappa \xi \\
 & + 4\pi^2 k^2 L \int_0^1 \int_0^\infty \kappa \Phi_n(\kappa) \\
 & \times \left\{ J_0(|\mathbf{r} - \xi \mathbf{p}/2| \kappa) - J_0(|\mathbf{r} - \mathbf{p}/2| \kappa) \exp \left[\frac{jL\kappa^2}{k} (1 - \xi) \right] \right\} d\kappa d\xi.
 \end{aligned}$$

15. If a 4 cm diameter smooth target moving away from the transmitter is illuminated by a spherical wave at 100 m there will be enhanced backscatter in the reflected wave. Assuming weak irradiance fluctuation conditions and $\lambda = 1.06 \mu\text{m}$,

- (a) at approximately what distance beyond 100 m will there be no enhanced backscatter?
 (b) At what further distance will the same target once again produce enhanced backscatter?

Ans. (a) Approximately 525 m.

16. A 10 cm diameter smooth target at 500 m from the transmitter is illuminated by an incident plane wave. If $\lambda = 1.06 \mu\text{m}$ and $C_n^2 = 5 \times 10^{-14} \text{ m}^{-2/3}$, what is the long-term spot diameter of the reflected wave?

Section 13.5

17. Given that the fourth-order moment $M(\mathbf{r}_1, \mathbf{r}_2, \mathbf{r}_3, \mathbf{r}_4)$ is defined by Eq. (83), deduce the result of Eq. (84).

Hint: Use Eq. (14) in Chap. 6.

18. Given the general correlation function (96) for a Gaussian-beam wave incident on a smooth finite plane reflector, show that it reduces to (99) in the limiting case of a spherical wave.
19. Given the general correlation function (97) for a Gaussian-beam wave incident on a smooth finite retroreflector, show that it reduces to (100) in the limiting case of a spherical wave.
20. Calculate the on-axis scintillation index (98) for a reflected spherical wave from a 10-cm plane mirror target at 500 m if $\lambda = 1.06 \mu\text{m}$ and $C_n^2 = 5 \times 10^{-14} \text{m}^{-2/3}$.

Section 13.6

21. Given the MCF defined by Eq. (39),
(a) show that it can be expressed in the form

$$\Gamma_2(\mathbf{r}_1, \mathbf{r}_2, 2L) = \sqrt{\langle I(\mathbf{r}_1, 2L) \rangle \langle I(\mathbf{r}_2, 2L) \rangle} \exp \left[-\frac{1}{2} \Delta(\mathbf{p}, \mathbf{r}, 2L) \right] \\ \times \exp \left\{ \frac{j}{2} \text{Im}[E_b^{iR}(\mathbf{r}_1, \mathbf{r}_2)] - \frac{jk}{2F} (r_1^2 - r_2^2) \right\},$$

where

$$\Delta(\mathbf{p}, \mathbf{r}, 2L) = \Delta^i(\mathbf{p}, \mathbf{r}, 2L) + \Delta^R(\mathbf{p}, \mathbf{r}, 2L) + \Delta^{iR}(\mathbf{p}, \mathbf{r}, 2L), \\ E_b^{iR}(\mathbf{r}_1, \mathbf{r}_2) = \langle \psi_b^i(0, L) \psi_b^R(\mathbf{r}_1, L) \rangle + \langle \psi_b^{i*}(0, L) \psi_b^{R*}(\mathbf{r}_2, L) \rangle.$$

- (b) Verify that the result in part (a) leads to the DOC defined by Eq. (109).
22. In the case of a spherical wave incident on a finite smooth target and $\mathbf{r}_2 = -\mathbf{r}_1$, show that the WSF (110) reduces to Eq. (114).
23. For separation distances $\rho \ll l_0$ and the von Kármán spectrum, show that in the case of a retroreflector, the WSF (114) reduces to

$$D(\rho, 2L) = 1.09 C_n^2 k^2 L l_0^{-1/3} \rho^2, \quad \rho \ll l_0.$$

Section 13.7

24. For a point target and Kolmogorov spectrum, show that Eq. (124) reduces to

$$P(\mathbf{r}_1, \mathbf{r}_2) = \exp \left(-1.63 C_n^2 k^{7/6} L^{11/6} \Lambda_2^{5/6} - 0.55 C_n^2 k^2 L \rho^{5/3} \right), \quad \rho = |\mathbf{r} - \mathbf{r}_2|.$$

25. Show that Eq. (128) for the two-point correlation function reduces to Eq. (130) in the case of an incident spherical wave and to Eq. (131) in the case of an incident plane wave.
26. In the case of a point target, show that the WSF (110) reduces to the results given by Eqs. (146).

27. In the case of a spherical wave incident on a point target, deduce that the normalized covariance function (151) has the residual value

$$b_I(\rho, 2L) = \frac{1}{2}, \quad \rho \rightarrow \infty.$$

28. In the case of a point target, verify that the scintillation index is given by Eq. (153).
29. For a spherical wave incident on a point target, show that the correlation function (155) reduces to

$$C_I^{iR}(\mathbf{r}, L) = 8\pi^2 k^2 L \int_0^\infty \int_0^\infty \kappa \Phi_n(\kappa) J_0(r\kappa\xi) \left\{ 1 - \cos\left[\frac{L\kappa^2}{k}\xi(1-\xi)\right] \right\} d\kappa d\xi.$$

30. For a spherical wave incident on a point target, show that the scintillation index in the strictly backward direction is given by (assume a Kolmogorov spectrum)

$$\sigma_I^2(0, 2L) = 1.6\sigma_1^2(L).$$

Section 13.8

31. In the limiting case of an unresolved (point) diffuse target, show that the correlation function (180) reduces to

$$B_I^{iR}(\mathbf{r}, L) = 8\pi^2 k^2 L \int_0^1 \int_0^\infty \kappa \Phi_n(\kappa) J_0(\kappa\xi r) \exp\left(-\frac{\Lambda_1 L \kappa^2 \xi^2}{2k}\right) \\ \times \left\{ \cos\left(\frac{L\kappa^2 \xi^2 \Theta_1}{2k}\right) - \cos\left[\frac{L\kappa^2}{2k}\xi(2-2\xi+\Theta_1\xi)\right] \right\} d\kappa d\xi.$$

32. For the special case of a spherical wave incident on a point diffuse target, show that the scintillation index in the strictly backward direction is given by (assume a Kolmogorov spectrum)

$$\sigma_I^2(0, 2L) = 1.6\sigma_1^2(L).$$

33. Starting with Eq. (197), show that it can be written in the form

$$\sigma_I^2(\mathbf{r}, 2L)_{\text{bistatic}} = 1 + 2\sigma_{I, \text{diff}}^2(L)[2 + \sigma_{I, \text{diff}}^2(L)].$$

34. Derive Eq. (199).

35. Based on Eqs. (198) for a bistatic channel and (199) for a monostatic channel, derive the asymptotic results

$$\sigma_I^2(0, 2L) \cong \begin{cases} 7 + \frac{15.12}{\beta_0^{4/5}}, & \beta_0^2 \gg 1 \quad (\text{bistatic}) \\ 11 + \frac{22.8}{\beta_0^{4/5}}, & \beta_0^2 \ll 1 \quad (\text{monostatic}). \end{cases}$$

References

1. J. I. Marcum and P. Swerling, "Studies of target detection by pulsed radar," *IRE Trans. On Information Theory*, Special Monograph **IT-6**, 59–308 (1960).
2. M. S. Belen'kii and V. L. Mironov, "Diffraction of optical radiation on a mirror disc in a turbulent atmosphere," *Kvantovaya Electron. (Moscow)* **5**, 38–45 (1972).
3. A. G. Vinogradov, Yu. A. Kravtsov, and V. I. Tatarskii, "Backscatter amplification effect for bodies located in a medium with random inhomogeneities," *Izv. Vyssh. Uchebn. Radiofiz.* **16**, 1064–1070 (1973).
4. A. S. Gurvich and S. S. Kasharov, "Problem of enhancement of scattering in a turbulent medium," *Radiophys. Quant. Electron.* **20**, 547–549 (1977).
5. Yu. A. Kravtsov and A. I. Saichev, "Effects of double passage of waves in randomly inhomogeneous media," *Sov. Phys. Usp.* **25**, 494–508 (1982).
6. V. P. Aksenov, V. A. Banakh, V. M. Buldakov, V. L. Mironov, and O. V. Tikhomirova, "Distribution of fluctuations of light intensity behind the objective of a telescope after reflection in a turbulent atmosphere," *Sov. J. Quantum Electron.* **15**, 1404–1406 (1985).
7. E. Jakeman, "Enhanced backscattering through a deep random phase screen," *J. Opt. Soc. Am. A* **5**, 1638–1648 (1988).
8. P. R. Tapster, A. R. Weeks, and E. Jakeman, "Observation of backscattering enhancement through atmospheric phase screens," *J. Opt. Soc. Am. A* **6**, 517–522 (1989).
9. G. Welsh and R. L. Phillips, "Simulation of enhanced backscatter by a phase screen," *J. Opt. Soc. Am. A* **7**, 578–584 (1990).
10. Yu. N. Barabanenkov, Yu. A. Kravtsov, V. D. Ozrin, and A. I. Saichev, "Enhanced backscattering in optics," in *Progress in Optics*, E. Wolf, ed., **29**, 65–197, Elsevier Science Publishers B.V. (1991).
11. J. F. Holmes, "Enhancement of backscattered intensity for a bistatic lidar operating in atmospheric turbulence," *Appl. Opt.* **30**, 2643–2646 (1991).
12. L. C. Andrews and W. B. Miller, "Single-pass and double-pass propagation through complex paraxial optical systems," *J. Opt. Soc. Am. A* **12**, 137–150 (1995); "Single-pass and double-pass propagation through complex paraxial optical systems: Errata," *J. Opt. Soc. Am. A* **12**, 2213 (1995).
13. L. C. Andrews and W. B. Miller, "The mutual coherence function and the backscatter amplification effect for a reflected Gaussian-beam wave in atmospheric turbulence," *Waves Random Media* **5**, 167–182 (1995).
14. L. C. Andrews, C. Y. Young, and W. B. Miller, "Coherence properties of a reflected optical wave in atmospheric turbulence," *J. Opt. Soc. Am. A* **13**, 851–861 (1996).
15. L. C. Andrews, R. L. Phillips, and W. B. Miller, "Mutual coherence function for a double-passage retroreflected optical wave in atmospheric turbulence," *Appl. Opt.* **36**, 698–708 (1997).

16. L. C. Andrews, R. L. Phillips, and A. R. Weeks, "Rytov approximation of the irradiance covariance and variance of a retroreflected optical beam in atmospheric turbulence," *J. Opt. Soc. Am. A* **14**, 1938–1948 (1997).
17. L. C. Andrews and R. L. Phillips, "Monostatic lidar in weak-to-strong turbulence," *Waves in Random Media*, **11**, 233–245 (2001).
18. V. A. Banakh and V. L. Mironov, *LIDAR in a Turbulent Atmosphere* (Artech House, Dedham, Mass., 1987).
19. Yu. A. Kravtsov, "New effects in wave propagation and scattering in random media (a mini review)," *Appl. Opt.* **32**, 2681–2691 (1993).
20. A. V. Jelalian, *Laser Radar Systems* (Artech House, Boston, 1992).
21. C. J. Solomon, "Double passage imaging through turbulence," in *Wave Propagation in Random Media (Scintillation)*, V. I. Tatarskii, A. Ishimaru, and V. U. Zavorotny, eds., SPIE Optical Engineering Press, Bellingham, Wash.; Institute of Physics Pub., Techno House, Bristol, England (1993).
22. M. S. Belen'kii, "Effect of residual turbulent scintillation and a remote-sensing technique for simultaneous determination of turbulence and scattering parameters of the atmosphere," *J. Opt. Soc. Am. A* **11**, 1150–1158 (1994).
23. L. C. Andrews, R. L. Phillips, and C. Y. Hopen, *Laser Beam Scintillation with Applications* (SPIE Press, Bellingham, Wash., 2001).
24. M. Tur, K. C. Chin, and J. W. Goodman, "When is speckle multiplicative?," *Appl. Opt.* **21**, 1157–1159 (1982).
25. J. W. Goodman, "Some effects of target-induced scintillation on optical radar performance," *Proc. IEEE* **53**, 1688–1700 (1965).
26. G. Ya. Patrushev, A. I. Petrov, and V. V. Pokasov, "Intensity fluctuations of mirror-reflected optical beams in a turbulent atmosphere," *Izv. Vyssh. Uchebn. Zaved. Radiofiz.* **26**, 823–830 (1983) (in Russian).
27. V. A. Banakh, "Influence of reflector edge diffraction on the amplification of backscattering in a turbulent atmosphere," *Atmos. Oceanic Opt.* **6**, 229–232 (1993).
28. V. A. Banakh, "Influence of reflector edges diffraction on manifestation of backscatter amplification effect," *Atmospheric Prop. and Remote Sensing II*, in Proc. SPIE **1968**, 312–318 (1993).

For a collection of many classic papers on laser radar, the reader is advised to consult the following reference:

Selected Papers on Laser Radar, G. W. Kamerman, ed., SPIE Milestone Series, Vol. MS 133 (SPIE Optical Engineering Press, Bellingham, Wash., 1997).